Quantum Sensing with NV Centers in Diamond

Dissertation
to acquire the doctoral degree in mathematics and natural science
'Doctor rerum naturalium'
at the Georg-August-Universität Göttingen
in the doctoral degree programme PROPHYS
at the Georg-August University School of Science (GAUSS)

Submitted by
Vinaya Kumar Kavatamane Rathnakara
from Kavatamane, Karnataka, India

Göttingen, 2019

Contents

List of Figures

List of Tables

Glossary

AC *Alternating Current.*

AWG *Arbitrary Wavefrom Generator.*

APD *Avalanche PhotoDiode.*

$|B|$ *External static magnetic field.*

c *Speed of light in vacuum.*

CB *Conduction Band.*

CPMG *Carr-Purcell-Meiboom-Gill sequence.*

CVD *Chemical Vapor Deposition.*

D_{es} *Zero Field Splitting (Excited State).*

D_{gs} *Zero Field Splitting (Ground State).*

DC *Direct Current.*

DD *Dynamical Decoupling.*

δ_m *Skin depth of alternating current.*

DYSCO *Dynamical Sensitivity Control.*

GMI *Giant Magneto-impedance.*

8CB *4-n-octyl-4'-cyanobiphenyl.*

ES *Excited State.*

ESR *Electron Spin Resonance.*

η_{AC} *AC magnetic field sensitivity.*

η_{DC} *DC magnetic field sensitivity.*

f_L *Larmor Frequency in Hz.*

FID *Free Induction Decay.*

FWHM *Full-width at half-maximum.*

Γ_p *Linewidth of proton signal.*

GS *Ground State.*

γ_n *Gyromagnetic ratio of nuclear spin.*

γ_e *Gyromagnetic ratio of electron/NV spin.*

γ_h *Gyromagnetic ratio of proton spin.*

h *Planck constant.*

$\hbar$ *Planck constant/2π.*

HPHT *High Pressure and High Temperature.*

HF *HyperFine.*

I *Nuclear spin quantum number.*

I_1 *Isotropic Phase.*

k_B *Boltzman Constant.*

LAC *Level AntiCrossing.*

λ *Wavelength of light.*

λ_s *Magnetostriction co-efficient.*

LC *Liquid Crystal.*

MRI *Magnetic Resonance Imaging.*

MW *Microwave.*

m_s *Electron spin sublevels.*

μ_B *Bohr magneton.*

μ_r *Relative permeability.*

μ_t *Total permeability.*

μ_0 *Vacuum permeability.*

N_1 *Nematic Phase.*

NV *Nitrogen Vacancy.*

NMR *Nuclear Magnetic Resonance.*

NA *Numerical Aperture.*

Ω_R *Rabi frequency.*

ODMR *Optically Detected Magnetic Resonance.*

PSF *Point Spread Function.*

RF *Radio Frequency.*

S *Electron spin quantum number.*

S_1 *Orientational order parameter.*

S' *Magnetometer signal.*

σ_s *Standard deviation.*

SNR *Signal to Noise Ratio.*

SQUID *Super Conducting Quantum Interference Device.*

T_1 *Spin-lattice relaxation time.*

T_2 *Coherence time.*

T_2^* *Spin dephasing time.*

V_{pp} *Amplitude of RF driving signal.*

VB *Valence Band.*

Z *Impedance.*

ZPL *Zero Phonon Line.*

Abstract

This thesis is concerned with studies involving quantum sensing based on Nitrogen-Vacancy (NV) center in diamond. Essentially, it attempts to address two important problems. First, enhancing the sensitivity of a single NV center to external static magnetic fields, and second, probing the phase transitions in a soft condensed matter system using a near surface NV center. NV center's sensitivity to time-varying or AC external magnetic fields is in the range of a few nT and is limited by coherence time of NV. For various applications, including the bio-magnetic measurements, it is necessary to sense nearly static or DC fields rather than the AC fields. However, in diamond samples with natural abundance ^{13}C concentration (1.1%), the best reported sensitivity to DC fields is in μT range and is limited by short lived spin dephasing time of NV. In the present work, a novel hybrid magnetometer consisting of a ferromagnetic material and a single NV center is utilized to achieve DC field sensitivity down to tens of nT. The ferromagnetic material exhibits a property known Giant magneto-impedance (GMI) and is sensitive to DC fields under certain conditions. The achievable sensitivity of GMI sensors is in the range of pT. By positioning a GMI microwire in close vicinity of a NV center, magnetic interaction between the microwire and NV center can be realized. In the presence of minute changes in the DC fields in the surroundings, the GMI wire responds and encodes information to the NV center. By employing a standard magnetometry sequence on NV this information can be readout. As the sequence relies on long lived NV coherence time, its overall sensitivity could be enhanced by over two orders of magnitude. Second study deals with detecting the temperature driven phase transitions in a soft matter system, namely a liquid crystal (LC) material. The chosen LC material shows distinct ordered phases close to room temperature. By varying the temperature, transitions from solid-like phases to liquid-like phases in a thin layer of LC can be induced. The NV sensors located at a few nm depths detect these transitions in terms of changes in the spin noise signal emanating from nanoscopic volumes containing LC molecules above the diamond surface. Temperature plays a key role in determining the soft matter properties. Since NV centers are also known as nanoscale temperature sensors, it is possible to tune the temperature precisely to the transition points. This way, NV based method is demonstrated as a dual mode sensing for studying soft matter systems at nanoscale, with a control over temperature. The work aims at extending NV centers as novel probes for exploring soft matter systems and address some important questions in that area.

Introduction

The field of quantum science and engineering is increasingly finding applications in several realms of modern research [1]. Particularly, in the area of measuring weak physical quantities from the environment, sensors based on the quantum concepts outperform their classical counterparts mainly due to their precision approaching fundamental limits [2, 3]. The physical quantities under consideration are electric and magnetic fields, temperature, pressure, frequency, and so forth. Several sophisticated sensing methods have been developed over the last decades and they have provided unprecedented levels of sensitivity to these quantities. While the sensitivities are approaching the fundamental limits, there are certain hindrances associated with some of these sensors. These include requirements of extreme operating conditions resulting in lack of universal applicability, bulky length scales of the sensor degrading the spatial resolution, power consumption and costs to name a few.

Proposal of crystal defects in solid state materials [4–6] as potential candidates for sensing a little over a decade ago has caused a lot of excitement because they are free from most of the limitations listed above. For example, negatively charged nitrogen-vacancy (NV) color centers in diamond have been extensively studied over the last decade and constitute a rapidly developing research area [7]. The center is formed out of a nitrogen atom, a most common impurity in the crystal lattice made of carbon atoms, and a vacancy site devoid of a carbon atom [8]. Owing to the remarkable thermal and mechanical properties of the diamond, the center forms a stable point defect in rigid crystal matrix. The decisive advantages offered by NV sensors over other sensors are- operability at ambient conditions, convenient optical readout of measured quantities, atomic size of the sensor resulting in sub-optical spatial resolution, ultralong quantum memory times at room temperatures and versatility to detect multiple physical quantities with high precision. The research interests with NV centers have been mainly focused on their applications as possible candidates for quantum metrology [9] and quantum information processing [10].

NV center is characterized by spin quantum number S=1 and its ground state spin levels form an effective two-level system. As remarkable candidates in quantum metrological applications, NV sensors as individual centers or as an ensemble, have been employed in various platforms. They have been demonstrated as efficient probes for detecting magnetic fields [6, 11], electric fields [12], temperature [13], pressure [14], and as highly photo-stable, non-toxic biomarkers [15]. Among these quantities, sensing applications involving magnetic fields form a core interest because of the high sensitivity of the electron spin associated with the NV center to these fields. Magnetic sensing using NV centers relies on determining the Zeeman shifts of its ground state energy levels to external perturbations [6]. In case of single centers, sensitivities to weak alternating [16] and static fields [17] have

3

been in the range of nT and μT, respectively. On the other hand, in ensemble NV centers, sensitivity scales as $1/\sqrt{N}$, where N is the number of defects used [18]. Accordingly, the sensitivity has been shown to reach pT level [19]. However, due to the requirement of large length scale over which the signal has to be averaged, the spatial resolution reduces by orders of magnitude. As a result, individual NV centers have been the probes of choice for many demonstrations involving the detection of weak magnetic fields, albeit with relatively low sensitivity.

For a NV center two of its triplet ground state spin sublevels form an effective two-level system and constitute a qubit. When placed in a coherent superposition of its two sublevels, the NV spin acquires a phase under the influence of external magnetic field [16]. For slowly varying or static fields the total phase acquired over a measurement run is non-zero and by measuring this phase one gets information about the external field. This method is analogous to traditional Ramsey interferrometric methods for measuring the fields in case of atomic magnetometers [9]. Sensitivity of a NV center to such fields critically depends on the measurement time over which the spin retains its phase. However, in the superposition state the NV spin quickly loses its phase due to its interaction with other noise sources, a process known as inhomogeneous dephasing [20]. This limits the measurement time and as a result, in case of NV centers located in the bulk of diamond their sensitivity to static fields usually lies at about a μT [17].

For sensing applications the NV center has to detect weak signals emanating from target sources outside the diamond. As the magnetic dipolar interaction between a NV center and the target falls off as inverse of distance cubed, it is crucial that NV-target distances are as short as possible. This necessitates fabrication of diamond samples containing NV centers close to the surface, at about a few nm depths, so as to be able to sense the external signals [21]. Due to the presence of additional noise sources at the surface than in the bulk, these near surface centers dephase even quickly than their bulk counterparts. This lowers their sensitivity by about an order of magnitude and the values are in the range of tens of μT [22]. This is a major hindrance in advancing the NV based sensing methods to be on par with the current state of the art magnetometers.

On the other hand, magnetic sensors based on classical concepts with modest sensitivity and operating at ambient conditions have been known for a long time [23]. During the 1990s, a magnetic phenomena known as Giant-magneto impedance (GMI) was discovered in certain ferromagnetic materials [24, 25] and it subsequently paved the way for designing a new class of magnetic field sensors based on classical concepts [26]. The GMI sensors exhibit $\sim 10^{-12}$ T sensitivity to static magnetic fields and this value is better than that of most other classical sensors such as fluxgate and Hall probes. While this range is still lower than the best achievable sensitivities of some of today's advanced sensors (10^{-15} T in case of SQUIDs, for example), relative ease of operation makes GMI sensors attractive candidates. There are also other non-trivial advantages offered by GMI sensors such as low power consumption, relatively small sensor head, response speed and linearity [27]. However, for sensing with high spatial resolution the GMI sensor heads need to be brought down to nanometer-scale. This is apparently a difficult task given the fact that most sensors employ millimeter-scale pick-up coils to readout the GMI response and hence the whole sensor assembly can not be scaled down in size.

The GMI materials can be moulded into various shapes, namely micro-wires, ribbons

and thin films [26]. This freedom allows for possibility of integrating the GMI materials with other sensors which could potentially offer better properties and more flexibility than the standalone sensors. As a comparison with GMI sensors, single NV centers have μT sensitivity at nanoscale spatial resolution. It is thus intriguing to couple them with GMI material and see if the overall GMI-NV sensitivity could approach that of standalone GMI sensors (pT).

In this regard, Chapter Two discusses a novel approach in which a single NV center is integrated with a micro-wire of GMI material. The achieved overall sensitivity to static fields is in the range of tens of nT.

Due to the nature of the Ramsey magnetometry, the method is inherently insensitive to alternating or magnetic fields which are varying on a faster time scale than the measurement time [28]. The overall phase acquired during a measurement gets averaged out due to the alternating sign of the field signal. In order to detect the alternating fields the method has to be modified to what is known as Echo technique, a concept borrowed from conventional magnetic resonance experiments [29]. An Echo based method makes the qubit only sensitive to alternating fields while being insensitive to static fields. Additionally, the interrogation time of the qubit can be extended beyond the inhomogeneous dephasing limit and its value can be at least two orders of magnitude higher than this limit [6, 16]. Thus, echo based methods effectively prolong the measurement times to actual or true coherence time (T_2) of the sensor. The spectral resolution of the detected alternating signal is given by the reciprocal of T_2 and longer the T_2 finer is the resolution [9].

This measurement of alternating signals has important implications for NV sensors. One particular interest is the detection of magnetic signals due to Larmor precession of nuclear spins in the samples outside the diamond crystal. Essentially, due to the nanoscopic sensing volumes associated with individual NV sensors one can perform nuclear magnetic resonance (NMR) experiments of samples at the nanoscale [30, 31]. NMR spectroscopy offers distinct fingerprint of the molecular structure and interactions of its chemical species with one another. However, it has been a long-standing goal to employ NMR for sensing and imaging individual atoms or even single molecules due to its poor sensitivity and bulky sizes of probe [32]. Magnetic resonance force microscopy (MRFM) methods [33] developed in the previous decade could perform nano-NMR but the requirement of extreme operating conditions hinders their widespread use in some important areas. In this context, NV based nano-NMR has turned out to be advantageous. The nano-NMR can be accomplished with individual NV sensors located at shallow depths while the sample of interest is directly placed on the diamond chip. In nanoscopic volumes, the magnetization signal from sample results from an ensemble of statistically polarized nuclear spins and an individual NV center is shown to be able to sense signals from $\sim 10^3$ such spins [31]. As a comparison, in conventional NMR, an ensemble of at least 10^{15} thermally polarized spins are required to produce a measurable signal.

The NV based nano-NMR is being intensively pursued after its first proposals and has been actively utilized to sense spin signatures from detection volumes of several $(\text{nm})^3$ above the diamond surface. NV based nano-NMR has been demonstrated to be sensitive down to single molecule and single spins. For example, signals from individual protein molecules [34, 35] and nuclear (^{29}Si and ^{1}H) spins [36, 37] have been detected. In the recent years, shallow NVs have also been employed as novel probes for investigating

several interesting features in condensed matter, particularly those in two dimensional (2D) systems. NV sensors offer unique non-perturbing probes for studying lower dimensional systems due to convenient optical readout. For instance, characterization of- atomically thin molecular layers [38], spin-spin interaction in a 2D water film [39], electrical properties of graphene layer [40] and metal films [41], and magnetic excitations in 2D ferromagnets [42], are reported. But, to the best of our knowledge NV sensors have not been proposed for exploring soft condensed matter physics.

Soft matter systems are ubiquitous and exist as polymers, liquid crystals, gels, emulsions, colloids, surfactant self-assemblies, granular materials, and many biological materials [43]. Understanding molecular origins of some of the interesting phenomena such as phase transitions is significant because of its relevance, from fundamental research to designing a new class of functional materials. Liquid crystal (LC) materials, owing to their unusually simultaneous occurrence of crystallinity and fluidity [44], have been the model systems for several studies [43, 45]. Knowledge of phase transitions in lower dimensional LC systems offers rich insights to understand more complex phenomena in other systems [44, 46] but, experimental investigations are often limited mainly due to lack of of versatile and non-invasive probes.

NV sensors can potentially address these issues. NMR spectroscopy is widely used in bulk LC systems, mainly for the elemental analysis and it has not been applied for studies at the nanoscale. Particularly, our NMR knowledge about LC systems across transitions of their wide varieties of phases in nanoscale is limited. In this regard, NV based NMR studies of a LC system have been reported in Chapter Three. A standard LC material showing ordered phases close to room temperature has been studied using individual NV centers located at a few nm below the diamond surface. The phase transitions are induced by varying the temperature. A single NV center is simultaneously used as a nanoscale sensor to monitor the temperature and to detect changes in the spin noise signal originating from the LC layer. As the NV center's detection volume extends upto a few molecular layers of thin LC film, the sensor is shown to be capable of performing nano-NMR. Steps to improve the signal to noise ratio and potential problems in soft matter that can be addressed are mentioned.

The outline of the thesis is as follows. Chapter One starts with an introduction to the NV center and reviews basic concepts of NV as a magnetic field sensor. The chapter presents a detailed experimental setup for optically addressing the single NV spin and its manipulation, and discuses the progress of various sensing schemes over the last decade and their applications. Chapter Two is about enhancing the static sensitivity of GMI-NV based hybrid sensor. It starts with an overview of the concepts underlying the GMI, and then moves to implementation of hybrid GMI-NV based magnetometry, demonstration of nT sensitivity and discuses the factors affecting the overall sensitivity and concludes with possible applications. The Chapter Three starts with a general introduction to LC systems and to phase transitions in LCs containing rod-like mesogenic molecules. Details about the materials and experimental methods are given in the following sections. Results and detailed discussion on the observed results is presented at the end of the chapter. The thesis concludes with a brief summary and outlook.

Chapter 1

NV centers in diamond: fundamentals and sensing applications

1.1 Diamond

1.1.1 Material properties

Diamond is an allotrope of carbon in which the carbon atoms are arranged in a certain face centered cubic (FCC) lattice. Diamonds are found in many applications due to their exceptional thermal, mechanical, optical, and electrical properties. Owing to the strong covalent bonding and low phonon scattering the diamond is a very good conductor of heat with a thermal conductivity of natural diamond measured to be 22 W/(cm.K) [47]. The diamond also has a low thermal expansion coefficient (1.0×10^{-6} K^{-1} for synthetic diamond at 300K). Diamond is the hardest known naturally occurring material with a hardness value of 10,000 kg/mm^2. The Young's modulus of the diamond is reported to be 1054 GPa [48].

There exists a wide bandgap of 5.47 eV between the valence and conduction bands in diamond as a result of which a pure diamond is transparent to visible light and hence appears colorless (figure 1.1a). The different colors in diamond arise due to the presence of impurities (figure 1.1b). Diamond also has a high index of refraction (n_D=2.417) which is suitable for applications like high photon confinement etc. As a result of wide bandgap the diamonds are generally electrical insulators except for some natural diamonds which are semiconductors due to the presence of impurities. The electrical resistivity of diamonds is of the order of 10^{11} to $10^{18}\Omega$.m. Besides, the chemical inertness, non-toxic nature, and possibility of surface functionalization makes diamond appear in a wide range of chemical and biological applications [15, 49].

1.1.2 Diamond synthesis

Over the past several decades, synthesis of diamonds in the laboratory has been developed to meet the increasing demands of the diamond based applications. At room temperature and pressure, graphite is the stable allotrope of carbon while diamond is a metastable allotrope. Presently, there are two methods used for the synthesis of diamonds in the

laboratory- one, High Pressure and High Temperature (HPHT) method which mimics the production of natural diamonds under geological conditions, and second, Chemical Vapor Deposition (CVD)method.

The HPHT method involves large anvil presses to generate high pressures in the range of 5-10 GPa and heaters to produce temperatures of about 2000 °C [50, 51]. Subjecting a carbon source (graphite) to such high pressures and temperatures results in the direct conversion to diamond [52]. Also, during the HPHT process an addition of molten metals acts as a catalyst to reduce the large kinetic barrier for the conversion of graphite into carbon.

The CVD method of synthesis of diamond involves chemical reaction of gaseous reactants and their deposition onto a substrate. The advantage of the CVD method is its ability to grow diamond under ambient pressure, and unlike HPHT route the incorporation of unwanted elements into the diamond can be avoided. Essentially, the CVD method contains following mechanisms [53, 54]: First, flow of gaseous reactants into the reactor takes place. The reactants are mainly the H_2 gas and a small amount of hydrocarbon, namely methane as source of carbon. Second, activation of gaseous reactions by supplying the energy. This activation is carried out mainly through either hot filaments or plasma. During the activation process, the molecular hydrogen (H_2) converts into atomic hydrogen (H), and then reacts with the hydrocarbons present in the gaseous mixtures. The resulting complex mixture is then transported to the substrate via diffusion and convection. Third, on the surface of substrate adsorption, reaction and desorption of various species occurs leading to nucleation and growth of the diamond film. The temperature of the substrate maintained around 800°C to avoid the growth of graphite. Also, the presence of H atoms selectively etches the sp^2 graphitic carbon and promotes the growth of sp^3 bonded diamond carbon.

In addition to the production of thin films and bulk crystals of diamond by HPHT and CVD method, there exist a few methods to produce nanocrystals of diamond. In a method called detonation technique [49], nanodiamonds are synthesized from controlled detonation of explosives containing TNT inside a metallic chamber. The nanodiamonds obtained by this method can be as small as several nanometers in diameters, but they suffer from the presence of significant amount of impurities. A much purer variety of nanodiamonds can be obtained by grinding large crystals to nanoscale by methods such as high energy ball milling of diamond microcrystals produced by HPHT [55] and CVD

(a)   (b)
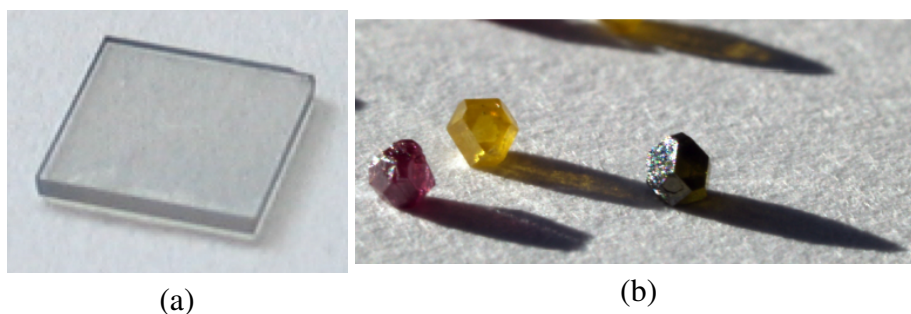
Figure 1.1: Photographs of pure single crystal diamond (a) and the doped diamonds (b). Doping giving rise to different colors in (b) are (from left to right): NV, nitrogen, & Vacancy.

methods [56].

1.1.3 Diamond Classification

The diamond is classified into two categories, Type I and Type II. The basis for the classification of diamond into two different types is the presence or absence of Nitrogen (N), the most common impurity in diamond [57]. The Type I diamonds contain detectable presence of N impurity atoms while the Type II do not.

Further, the Type I is classified into Type Ia and Type Ib. The Type Ia diamonds account for upto 98% of the natural diamonds. They contain substantial N impurities, with N concentration ranging from 500 ppm to 3000 ppm. The Type Ib diamond also contains significant N concentration but less than Type Ia. Here, the N concentration can be upto 300 ppm. Typically the diamonds synthesized by HPHT method fall into the Type Ib category.

In Type II diamonds the N concentration is about 1 ppm or less. The Type II is further divided into Type IIa and Type IIb depending on the absence and presence of boron impurities, respectively. Diamonds synthesized from CVD method fall into the Type IIa category and because of lack of impurities they appear transparent. For the experimental studies reported in this thesis commercially available Type IIa diamonds (with N concentration about 1 ppm) were used. The Type IIb diamonds contain significant presence of boron impurities and as a result they are also p-type semiconductors. Table 1.1 summarizes the classification of diamonds.

1.2 Color centers in Diamond

As a result of wide bandgap (5.5 eV) the diamond is able to host a vast number (more than 500) of optically active defects or color centers [57, 58]. These color centers being present in a rigid crystal structre of diamond, can be easily adressed individually by laser excitation. Moreover, the defects in diamond are often characterised by low electron phonon coupling due to high Debye temperature of diamond 2200 K, resulting in long relaxation times [59]. Some of these color centers are single photon sources, meaning that they emit only one photon per excitation and emission cycle. Such single photon sources are an essential prerequisite for a variety of modern technologies like quantum computation and information processing, metrology, and photonics [60]. Color centers

Type	[N] in ppm	Distinctive feature	Production method
Ia	∼500-3000	Aggregates of N	Natural occurrence
Ib	∼300	Individual N	HPHT
IIa	≤ 1	Very low N and other impurities	CVD, Natural
IIb	≤ 1	Significant boron content	Natural, HPHT

Table 1.1: Classification of diamonds into different categories.
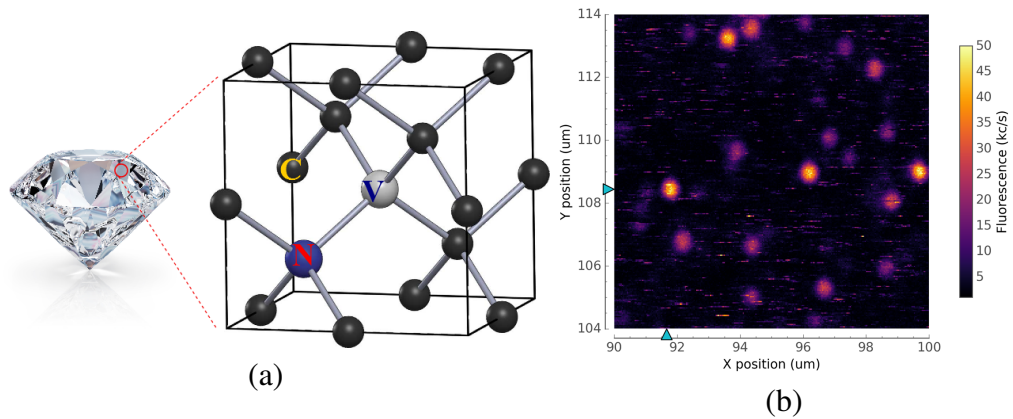
Figure 1.2: (a) NV center in Diamond. Nitrogen (N) is marked in blue, the vacancy (V) in grey, and the individual carbon atoms in black spheres. (b) Identification of individual NV centers (bright spots) in a $10 \times 10 \ \mu m^2$ photo-luminescence confocal scan.

in diamond offer additional advantages like photo stable emission, and room temperature operation compared to their other solid-state counterparts like atoms, trapped-ions and quantum dots.

1.2.1 Nitrogen-Vacancy color centers

The Nitrogen-Vacancy (NV) color center is a most common point defect in diamond. It is a point defect formed by most abundant impurity in diamond, a substitutional nitrogen (N) atom, and a carbon vacancy (V) adjacent to it. The NV center is schematically depicted in the figure 1.2a and a standard confocal image of NV centers is shown in figure 1.2b. The NV centers can be formed either naturally during the growth of diamond or artificially using the techniques like implantation. What makes the NV center an outstanding defect among other color centers in diamond is that it has a non-zero spin S, making the defect magnetic, and its optical properties are spin dependent. This magneto-optical property of the NV centers has been exploited in the recent years for various applications [8, 61, 62].

1.2.1.1 Electronic structure and optical properties

NV centers are created naturally during the CVD growth process, or by irradiation and annealing, or by ion implantation and annealing. Experimentally it is found that the NV center exists in two charge states, namely negatively charged, (NV^-) and neutral (NV^0) states. The distinctive feature of these two charge state is their optical resonance line known as zero phonon line (ZPL) in the emission spectra (figure 1.3).

In the case of NV^- there are totally six electrons involved in the structure [64]. Out of five valence electrons of nitrogen, three make covalent bonding with the neighboring carbon atoms while two electrons remain unbonded. The three carbon atoms surrounding the vacancy provide three electrons through dangling bonds. An additional electron is captured from the lattice, probably through the nitrogen donors. Even number of spins (6) results in integer number for spin. Electron spin resonance (ESR) studies have showed
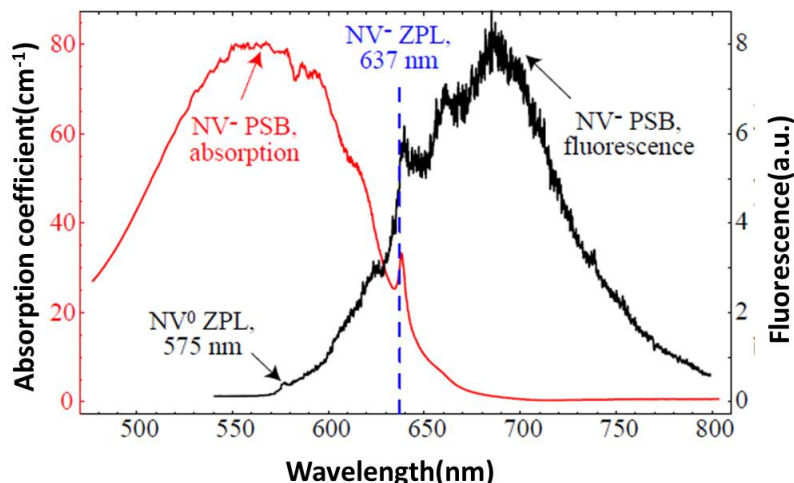
Figure 1.3: Optical absorption and Fluorescence spectra of single NV^- center at room temperature. The fluorescence recorded under 532 nm excitation shows the ZPL=637 nm along with the PSB. The ZPL of NV^0 is also indicated. The picture adapted from [63].

that the NV^- has an electron spin angular momentum S =1 in its ground state (GS) [64]. According to group theoretical calculations the center belongs to C_{3V} symmetry group [65]. The center's electronic GS is identified as a spin-triplet ($^3A_2$) with the degenerate spin sublevels $m_s=\pm 1$ split by D_{gs}=2.87 GHz from the m_s=0 spin sublevels under zero magnetic field [66]. The excited state (ES) identified as ^3E is also a spin triplet with a zero-field splitting D_{es} = 1.42 GHz (roughly half of D_{gs}) between $m_s=\pm 1$ and m_s=0 spin sublevels [67].

The NV^0 has five electrons in its structure. The fluorescence emission at λ= 575 nm corresponds to 2.156 eV optical transition from an excited (A) to ground (E) level [68]. However, due to absence of any magnetic resonance associated with its ground and excited state [69] NV^0 has not attracted much research interest and hence it hasn't been explored extensively. However, it is known that laser illumination-induced ionization can cause interconversion between NV^- and NV^0 states [70, 71]. Both NV^- and NV^0 emit strong fluorescence thereby allowing their identification easier under confocal microscopy (figure 1.2b). Conversion between the two charge states poses a major challenge, particularly in case of the shallow (a few nm below the surface) NVs in diamond. This thesis deals with mainly the NV^- center and thus it will be denoted as NV center for simplicity in the rest of the thesis.

The optical spectra of a single NV center is shown in figure 1.3. It contains a broad absorption band and a broad emission band. To explain the Stokes shifted absorption and anti-Stokes shifted emission spectra, Huang–Rhys model has been invoked [8, 72]. Due to the interactions of the electronic and vibrational degrees of freedom, the GS and ES of the center can be represented by harmonic potential wells with discrete vibrational levels. The minima of these wells do not coincide because of the displacement of the equilibrium positions of the nuclei during the optical transitions between GS and ES. By applying the Frank-Condon principle, the most probable transitions at thermal equilibrium are those from the lowest vibronic levels of the GS to the higher levels of the ES. This results in an

11
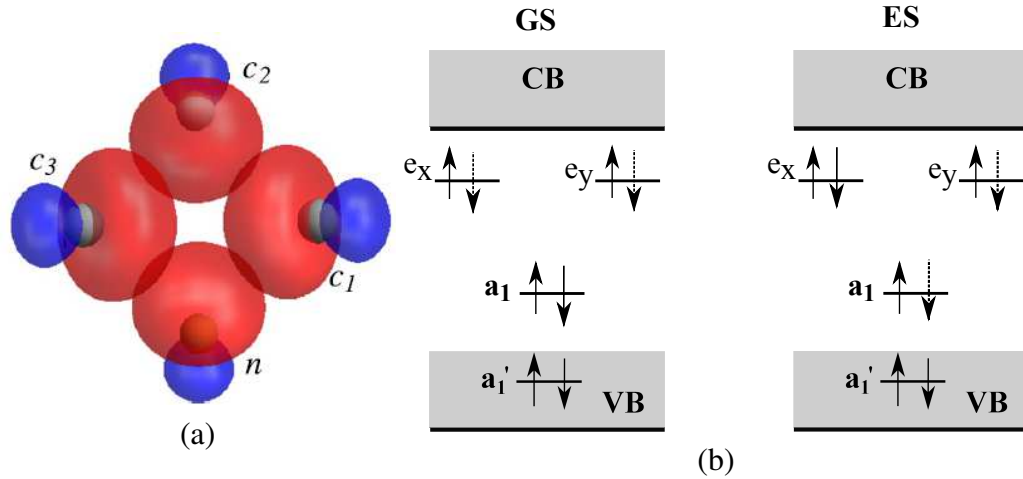
Figure 1.4: (a) Molecular orbital model depiction of the NV$^-$ center's electronic state. Carbon atoms (c_1,c_2,c_3) and nitrogen (n) surrounding the vacancy are shown (figure reused with permission from Elsevier, ref. [8]). (b) Six electrons (with up and down spins) of the center are denoted by arrows. VB and CB stand for valence band and conduction band, respectively. GS and ES are Ground and excited state levels, respectively.

absorption band called as Phonon side band (PSB) with a broad peak around 560nm. In the ES the transition to its lowest level happens non-radiatively. From here the transition back to GS happens for all vibronic levels (in GS) radiatively. Consequently, this gives rise to PSB of the emission and the band extends from 637nm to 750nm. The resonant transition between the two lowest vibronic levels in ES and GS is called as zero phonon line (ZPL) with a wavelength λ_{ZPL} = 637 nm (1.945eV) for the NV$^-$ center. Due to the low transition rates the ZPL accounts for only 4% of the total fluorescence at room temperature.

In the case of NV$^-$ center, the electron density is highly localized at the vacancy and nearest neighbours. This allows for the application of the molecular models to the NV-center and the electronic state can be represented in terms of Molecular Orbitals (MOs). Based on the group theoretical calculations the electron configurations for the ground and excited states has been described [64, 65, 73]. It is explained by six electrons occupying the two lower ($a_1^{'}$, a_1) and energetically degenerate (e_x,e_y) MOs. These orbitals exist between the diamond band gap and can be expressed in terms of the linear combination of the sp^3 orbitals of the nitrogen and three carbon atoms surrounding the vacancy (figure 1.4a). In the $^3A_2$ GS the lower $a_1^{'}$ and a_1 are fully occupied while the e_x and e_y MOs each contain an unpaired electron (figure 1.4b). These two unpaired electrons form S=1 spin triplet. The ES configuration is consisted of one electron from the orbital a_1 being moved to orbital e_x or e_y. The zero field splitting in the GS and ES arises from the spin-spin interactions of the two unpaired electrons. The calculations have showed that the orbitals (a_1, e_x and e_y) are localized near the vacancy and the orbital $a_1^{'}$ lies within the valence band. Note that while the NV$^-$ charge state contains four electrons in excess of filled valence band, the NV^0 state contains three electrons in excess of filled valence band. In both NV$^-$ and NV^0, the $a_1^{'}$ remains filled within the valence band.
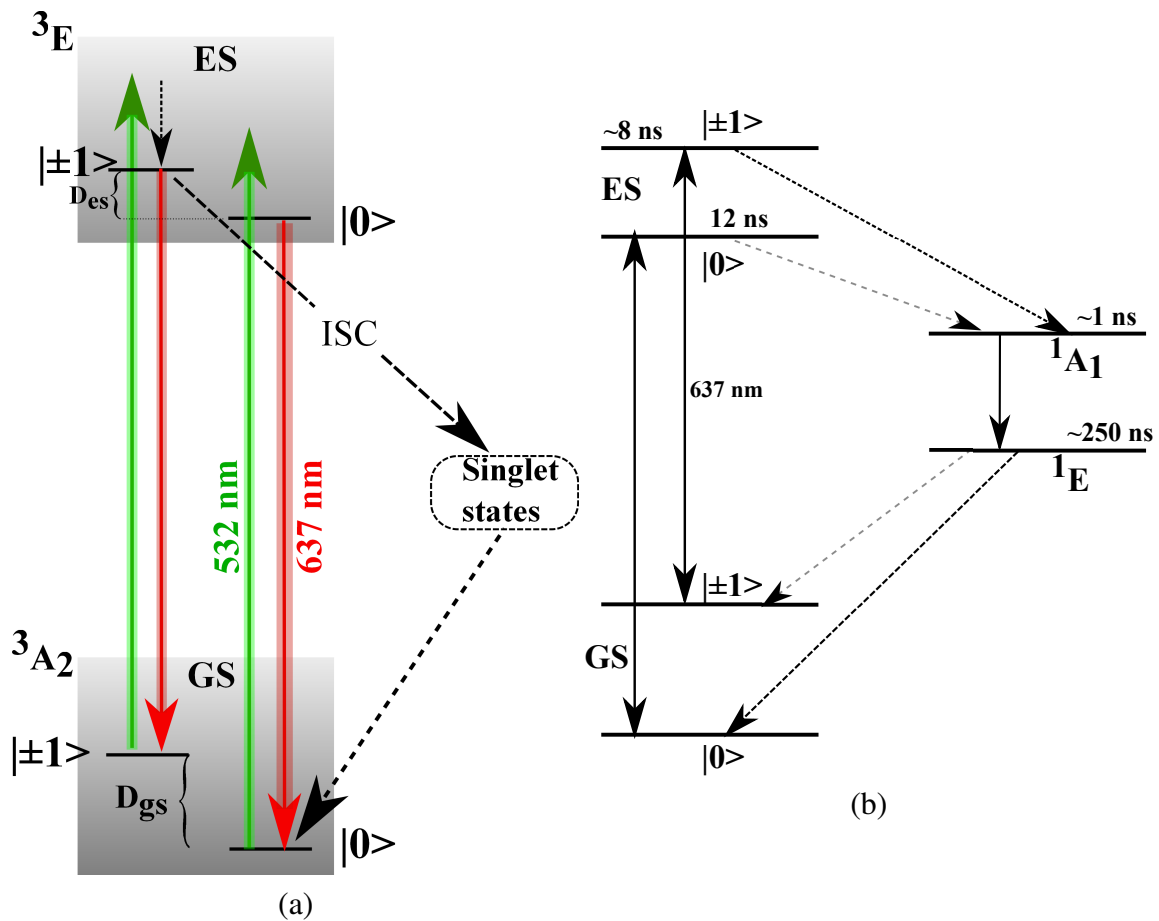
Figure 1.5: (a) Simplified energy level scheme of the NV⁻ center. (b) Mechanism of optical spin polarization. Life times of the excited and intermediate states of the single NV centers in bulk diamond are given in ns. Spin conserving optical transitions are bold lines, non-radiative transitions are black dotted lines, and transitions with low probability (non-radiative) are shown in grey dotted lines. Spin sublevels m_s=0 and ± 1 are denoted by |0> and |± 1> respectively. For simplicity degenerate m_s=± 1 are considered (zero external magnetic field).

1.2.1.2 Optical Spin polarization

Figure 1.5a shows simplified energy level of the NV center. Under an off-resonant green Laser excitation the spin conserving (Δm_s=0) optical transitions from the excited ^{3}E to ground state ^{3}A$_2$ levels produce ZPL emission at 637 nm, besides the emission via the PSB discussed above. There is another pathway through which the NV center decays from ^{3}E to ^{3}A$_2$ state. This is called *inter-system crossing* (ISC) to intermediate singlet states and is a non-radiative decay. This is a very important aspect of the NV center and gives rise to optical spin polarization (discussed below) in the m_s=0 of ^{3}A$_2$ state.

One of the attractive features of the NV center is that it can be optically addressed and thus makes it a very convenient tool for wide range of applications. This feature stems from the fact that the center can be optically polarized to m_s=0 in the GS [74–79]. The NV center's optical polarization mechanism has been schematically illustrated in the figure 1.5b with a six level model. At thermal equilibrium the two GS sublevels (0 and $\pm$1) are almost equally populated. In the presence of green laser (i.e., off-resonant) of sufficient intensity, both m_s=0 and $\pm$1 sublevels undergo spin conserving excitation transition to ES and radiative emission transition to GS. While in the ES the m_s=$\pm$1 state has higher probability (black dotted line in figure 1.5b) of undergoing a non-radiative ISC to one (^{1}A$_1$) of the metastable singlet states than the m_s=0 state (grey dotted line in figure 1.5b). From the ^{1}A$_1$ state the spin undergoes a radiative (1042 nm) decay to a long-lived (lifetime[1] $\sim$250ns) ^{1}E state. But from ^{1}E state the decay happens non-radiatively and preferentially to the m_s=0 level in the GS. Therefore, at the beginning of the laser if the spin was in m_s=$\pm$1 then due to non-radiative decays it ends up emitting less fluorescence and appears 'Dark'. On the other hand if the spin was already in the m_s=0 state at the start of the laser, then it predominantly relaxes back to GS by emitting fluorescence and hence appears 'Bright'. This fluorescence difference amounts to about 30% per cycle and enables one to distinguish the spin sublevels (0 and $\pm$1) in the GS through the optical contrast.

This spin state dependent decay from ES and singlet states to m_s=0 sublevel in the GS produces the optical spin polarization in the GS. The degree of this spin polarization, averaged in time (over a μs) is found to be 50-100% [78, 80–82].

1.2.1.3 NV spin Hamiltonian

The total Hamiltonian ($\hat{H}$) of the ^{3}A$_2$ GS spin triplet is given by the sum of contributions from the zero field splitting (H_{ZFS}), electron Zeeman interactions H_{eZ}, hyperfine interaction (H_{HF}) between electron spin, S and nuclear spin, I, and nulcear spin interactions. But since the nuclear spin interaction part includes quadrupole splitting[2] and nuclear Zeeman interactions[3] which are irrelevant for the studies mentioned in the thesis they will not be considered in the $\hat{H}$. The general form of the $\hat{H}$ is then,

$$\begin{aligned}
\hat{H} &= \hat{H}_{ZFS} + \hat{H}_{eZ} + \hat{H}_{HF} \\
&= h[D_{gs}S_z^2 + E(S_x^2 - S_y^2)] + g_e\mu_B\vec{B}\vec{S} + (S\mathbf{A}I_N)
\end{aligned} \tag{1.1}$$

---

[1] the lifetime is temperature dependent, and 250 ns is the average value between cryogenic and room temperature values

[2] N-15 and C-13 do not have quadrupole moment.

[3] smaller gyromagnetic ratio of nucleus compared to that of electron.

where, S_z, S_x, S_y and I_x, I_y, I_z are the components of the S and I repectively; D_{gs} and E are axial and transverse ZFS factors respectively; g_e- electron g-factor (2.003), μ_B-Bohr magneton, h is the Planck constant, $\vec{B}$ is the magnetic field and $\mathbf{A}$ is hyperfine tensor with nuclear spin (I_N).

ZFS term: As mentioned earlier, the spin-spin interaction of the two unpaired electrons in the e_x and e_y MOs of GS gives rise to a splitting of the NV spin m_s=0 and m_s=±1 sublevels at zero magnetic field by 2.87 GHz (D_{gs}). Hence it is called as zero field splitting (ZFS) [64]. The parameter D_{gs} is sensitive to temperature and it has a linear temperature dependence of $\approx$ -70kHz/K in the range of 280K-330K [83]. This property can be exploited to use NV centers as atom-sized temperature sensors. The NV axis along the [111] direction is taken as the z-axis which also defines the spin quantization axis (figure 1.6a) [84]. Mainly the axial S_z component of the spin interacts with D_{gs}, while the transverse components S_x and S_y interact only with the significant strain or electric fields (E). As the typical range of values (kHz-MHz) for E is small compared to D_{gs} (in GHz scale), the E term in the $\hat{H}$ can be safely ignored.

Zeeman term:

The Zeeman term results from the interaction of the electron spin with the magnetic field. For the case of $\vec{B} \parallel$ NV axis the Zeeman term is written as $\gamma_e|\mathrm{B}|S_z$, where γ_e=($g_e\mu_B\vec{B}\vec{S}$)/h=2.8 MHz/G is the gyromagnetic ratio of the NV electron spin [84] and |B| is the magnitude of $\vec{B}$. When the $\vec{B}$ is aligned along the NV axis, the degeneracy of the m_s=±1 levels in both GS and ES is lifted, and they split linearly as a function of |B| (figure 1.6b). The splitting between m_s=±1 varies as $2\gamma_e$|B|. Here the m_s is a good quantum number. When |B| is close to 500 G, the levels are mixed due to the level anti-crossing (LAC) of the m_s=0 and -1 spin levels in the ES [67, 85]. Since the D in GS is twice as large, the LAC between the m_s=0 and -1 happens at $\approx$1000 G in the GS. The ES-LAC has an important consequence that it results in the polarization of the nitrogen nuclear spins [86]. The variation of m_s levels in the case of an off-axis $\vec{B}$ (i.e., $\vec{B}\perp$NV) is sketched in figure 1.6c where the splitting m_s=±1 levels is not linear. For a very large off-axis field, the quantization axis does not coincide with the NV axis and m_s is no longer a good quantum number [87]. This will lead to reduction of the optically induced spin polarization and hence the inefficient spin dependent photoluminescence of the NV. For all the studies mentioned in the thesis, the $\vec{B}$ is always aligned along the NV axis, and hence the off-axis fields are not relevant here.

Hyperfine(HF) interaction

The last term in the equation 1.1 results from the HF interaction of the NV electron spin with the surrounding nuclear spins. The most prominent HF interaction is due to the host nitrogen nucleus in the NV complex. For ^{14}N which has natural abundance of 99.6%, the spin quantum number I=1. This will give rise to HF splitting of the NV center's m_s levels into total 2I+1 sublevels (m_I=-1,0 and 1) [88, 89]. The $\mathbf{A}$ for ^{14}N is 2.2 MHz, which is the spacing between each m_I levels. The other rare isotope of nitrogen ^{15}N has I=$\frac{1}{2}$ and hence gives rise to doublet (m_I=$-\frac{1}{2}$ and $\frac{1}{2}$). For ^{15}N, the HF factor $\mathbf{A} \sim 3.1$ MHz and therefore, the two m_I are separated by this amount [90]. Other possible HF results from the 1.1% natural abundance ^{13}C spins in an otherwise spin-free ^{12}C diamond lattice. The ^{13}C has I=$\frac{1}{2}$ and gives rise to doublet splitting like in the case of ^{15}N [91]. But the extent of HF spacing depends on the distance and orientation of the ^{13}C spins with respect to the
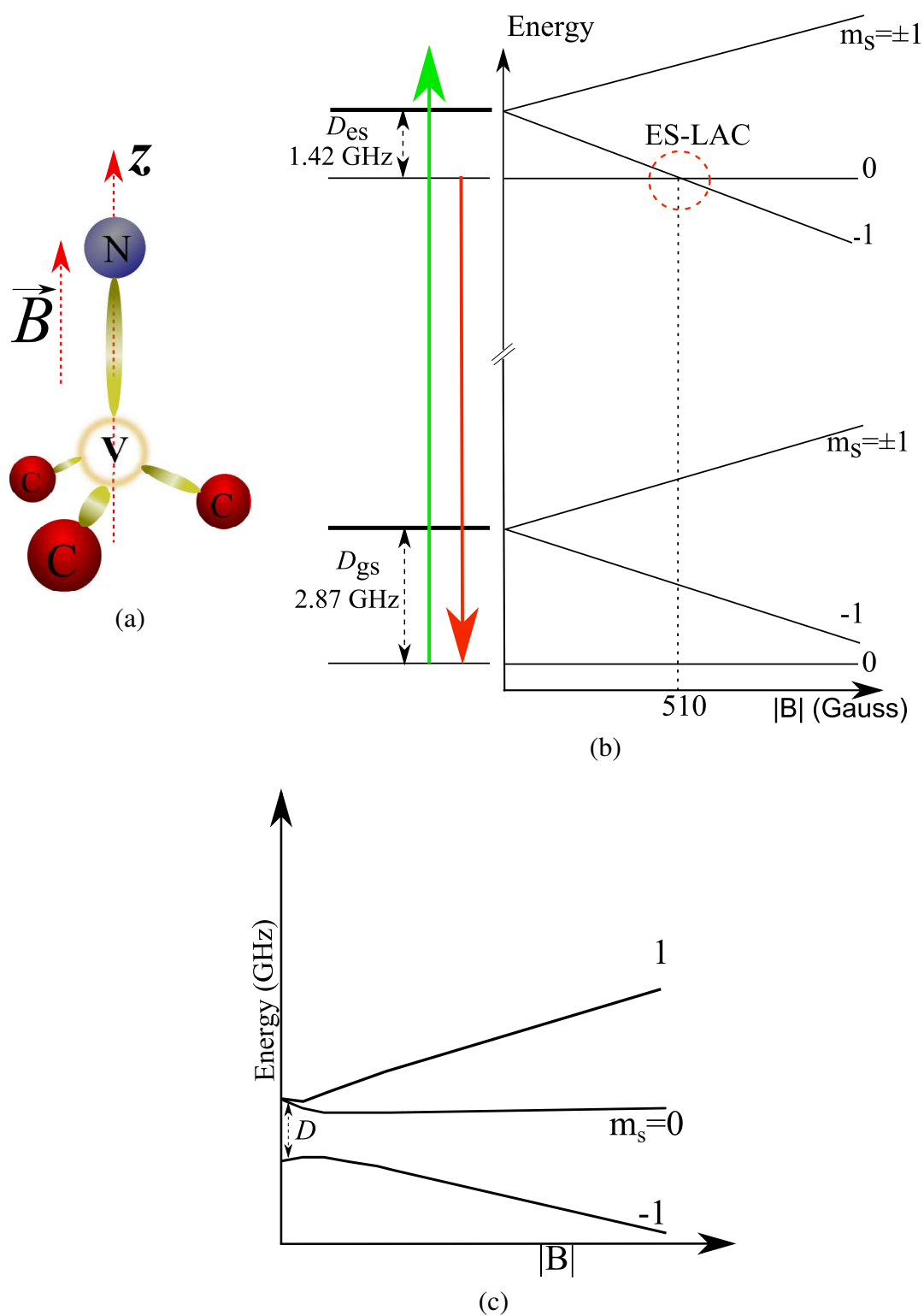
Figure 1.6: (a) Diagram showing NV quantization axis (z) and $\vec{B}$. (b) Energy level diagram showing the splitting of the $m_s=\pm 1$ in GS and ES as a function of |B| for the case, $\vec{B} \parallel NV$. (c) Energy versus |B| for the case of off-axis (NV$\perp \vec{B}$) field. For both cases in (b) and (c) the E of the NV center is assumed to be zero.

NV center [92]. Therefore, the total HF should consists of contributions of nitrogen and all coupled ^{13}C spins [93]. For the case of no strongly coupled ^{13}C, the effective HF term can be restricted to only nitrogen.

Finally, the simplified Hamiltonian in the equation 1.1 can be written as,

$$\hat{H} = D_{\text{gs}}S_z^2 + \gamma_e |\mathbf{B}| S_z + S\mathbf{A}I \tag{1.2}$$

1.3 Experimental setup

For the results presented in this thesis, two almost identical experimental setups capable of manipulating single NV center spins in diamond were built and utilized. Essentially each set up consists of an optical part for the optical identification and preparation of the NV spin, and a microwave (MW) and radio frequency (RF) part for the subsequent manipulation of the chosen NV spin. Figure 1.7 shows a simplified schematic diagram of the experimental setup.

1.3.1 Optical part

Optical identification of single NV center is done using a home-built confocal microscope. Basically, the optical part can be divided into two sections: Laser excitation and NV fluorescence detection. Besides, the optical path is also designed to produce pulsed laser pulses for the pulsed experiments described in the section 1.4.

1.3.1.1 Excitation Path

The laser excitation section consists of a laser source (gem 532, *Laser Quantum*) producing continuous wave (CW) green laser (532 nm) beam at variable power (from 0 to 200mW). First, a polarizing beam splitter cube (PBS25-532, *Thorlabs*) separates the p- and s- components of laser beam by selective reflection and transmission. The transmitted (p-polarized) beam is expanded by a combination of two lenses (L) having an equal focal length (f=100 mm). For producing the pulsed laser light for optical excitation of NV center, an acousto optic modulator (AOM) operating in the double-pass configuration [94] is utilized. By making the beam pass through the AOM twice, a high Laser On/Laser off ratio (also called as suppression ratio) could be obtained, which is crucial for pulsed experiments. The AOM (*AA optoelec.*) was fixed on a five-axis stage (PY005/M, *Thorlabs*) such that its position and orientation angle to the beam can be adjusted to get optimum Bragg diffraction conditions. The AOM is positioned at the midpoint of the two lenses and the beam diameter is adjusted such it matches the active aperture of the AOM crystal. For obtaining the diffraction of light, the AOM is driven with a RF driver board (MODAxx,*AAoptoelec.*). In the first pass, a required diffraction order[4] ($m = +1$) of the beam is selected using an aperture (AP) and made to pass through a quarter-wave ($\lambda/4$) plate. The beam is then retroreflected using a combination of additional lens and a mirror. While traversing the $\lambda/4$ plate twice, the resulting beam has an orthogonal linear polarization with respect to the

---

[4]0th order is a non-diffracted beam and can not be modulated with AOM for switching on/off
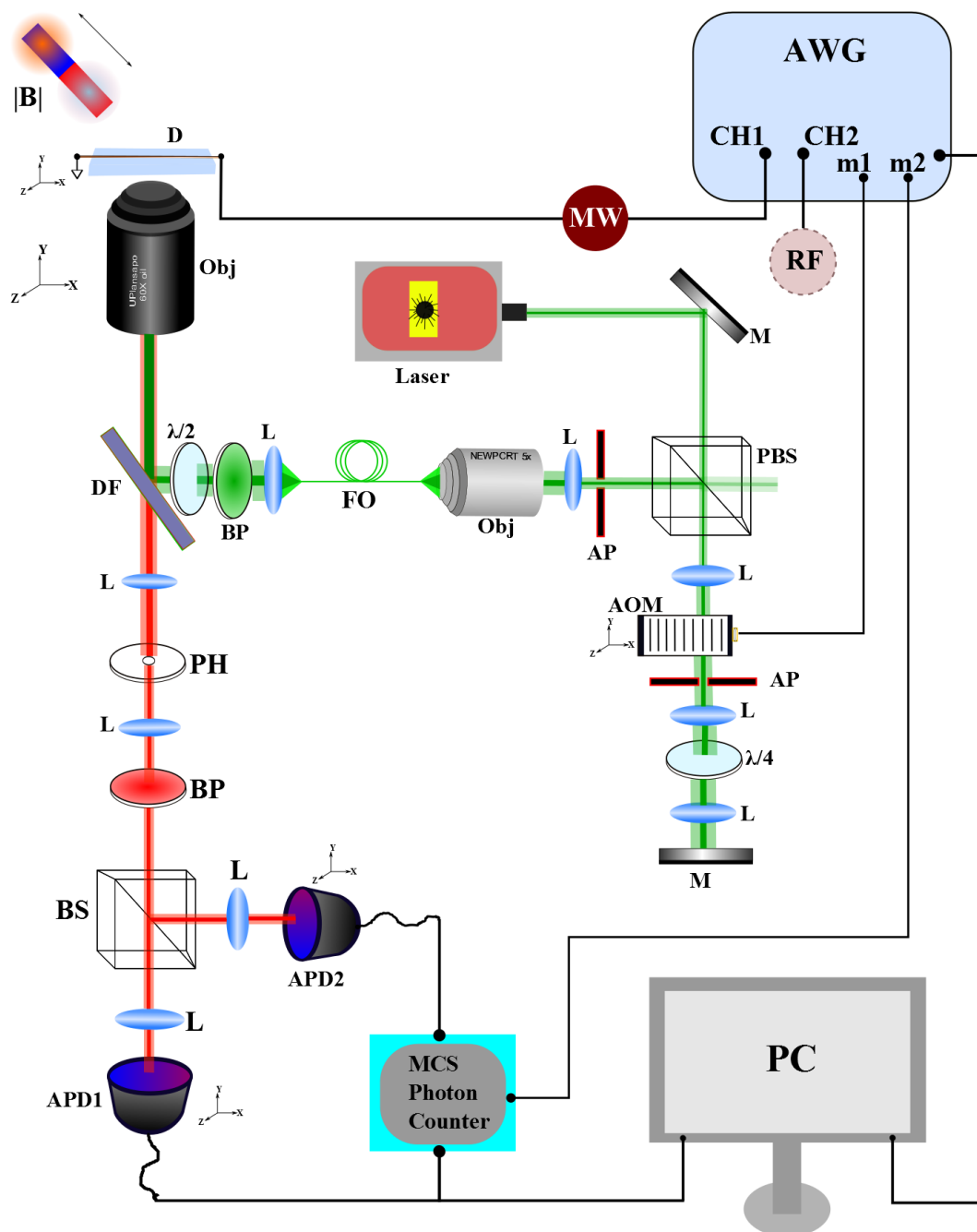
Figure 1.7: Simplified schematic diagram of single NV spin manipulation setup. Abbreviations stand for (clockwise from top): |B|- Permanent magnet; D-diamond sample with MW antenna; obj-oil objective; MW-microwave amplifier; M-mirror; RF-radio frequency signal; PBS-polarizing beam splitter; L-achromatic lens; AOM-Acousto optic modulator; AP-beam aperture; $\lambda/4$-quarter wave plate; PC-computer; APD-avalanche photo diode; BS-non-polarizing (50:50) beam splitter; BP-bandpass filter (red); PH-pin hole; DF- dichroic filter; $\lambda/4$-half wave plate; BP-band pass (green); FO-optic fiber; obj-objective (air).

incident beam and passes through the AOM for the second time. Due to the orthogonality of the polarization, the second passed beam reflects off the PBS and contains the diffraction orders. With an additional AP after the PBS, $m = +1$ order of the second pass can be selected. The resulting laser pulse has a rise time of $\sim$20 ns and the suppression ratios are found to be around 1000:1. The second passed (polarized) beam is then coupled into a single-mode polarization-maintaining optic fiber (NA=0.12; core size 10 μm; LMA-PM-10, *NKT*) using a low magnification (5X) microscope objective (NA=0.1; *Newport*). The objective and coupling end of the fiber are fixed on a fiber coupler. The coupling efficiency of the fiber is about 30-35%. The coupled out beam is then expanded to desired size (with a lens), and filtered using a narrow band (527-537 nm) laser clean-up filter (ZET 532/10, *AHF*) to get rid of unwanted wavelengths resulting from the scattering effects at the fiber core. A dichroic beam-splitter (zt561 RDC, *AHF*) (DF) plate at 45° angle to the incident beam reflects off the beam towards the sample stage. A $\lambda/2$ plate before DF could be used to rotate the angle of linearly polarized light going towards the sample.

The sample stage consisted of an oil immersion microscope objective (60X;working distance: 150 μm; NA=1.35; UPLSAPO, *Olympus*) and the diamond sample. For the imaging of the diamond sample, an objective-scanning and sample-stationary approach is used. Here, the objective was fixed to the three-axis (3D) nano-positioning piezo scanner stage ($200\mu m \times 200\mu m \times 25\mu m$, from *npoint*) which is controlled by a motion controller (C300 DSP controller, *npoint*). The control signals to the controller are provided by an I/O device (USB-6363, *NationalInstruments*) which is interfaced with the computer. The software for confocal microscope is implemented and controlled using a $Qudi - Python$ platform [95]. The diamond samples containing NV centers can be mounted on a sample holder made of PCB microwave stripline circuit (figure 1.8a). The holder is fixed to a sturdy 3D linear positioner (M-562-XYZ, *Newport*) for coarse positioning of the diamond sample to reach NV centers at different lateral locations and depths for optical imaging.

1.3.1.2 Detection path

The objective accomplishes the two tasks-focusing the green light onto the sample and simultaneously collecting the broadband near-infrared fluorescence (figure 1.3) from the NV centers. The fluorescence light spatially overlapping with the back-reflected green light from the sample is separated using the DF plate which transmits the wavelengths longer than 560 nm. Following the standard confocal method, the transmitted light from DF is focused to a 25 μm precision pin hole (PH) using a tube lens (f =75 mm). The PH acts like a spatial filter, and the focal point of the objective coincides with the image plane of the PH.

The confocal point spread function (PSF) of the imaged object is a diffraction limited-ellipsoid with a full-width at half-maximum (FWHM) of lateral extent, $\Delta r \approx \lambda/(2 \text{ NA})$ and that of axial extent, $\Delta z \approx \lambda n/(\text{NA})^2$, where λ is the wavelength, NA-numerical aperture of objective, and n-refractive index of the oil medium [96, 97]. The Δr and Δz are also known as lateral resolution and axial resolution of the confocal microscope, respectively. For our case, λ =532 nm, NA=1.35 and n=1.52 (oil from *SigmaAldrich*) result in $\Delta r \approx$200 nm and $\Delta z \approx$450 nm.

The collected light is filtered to selectively allow the fluorescence from the NV$^-$ while blocking the NV^0 by using a band-pass filter of 660-800 nm (BrightLine731/137, *AHF*).

(a)

(b)

(c)

(d)
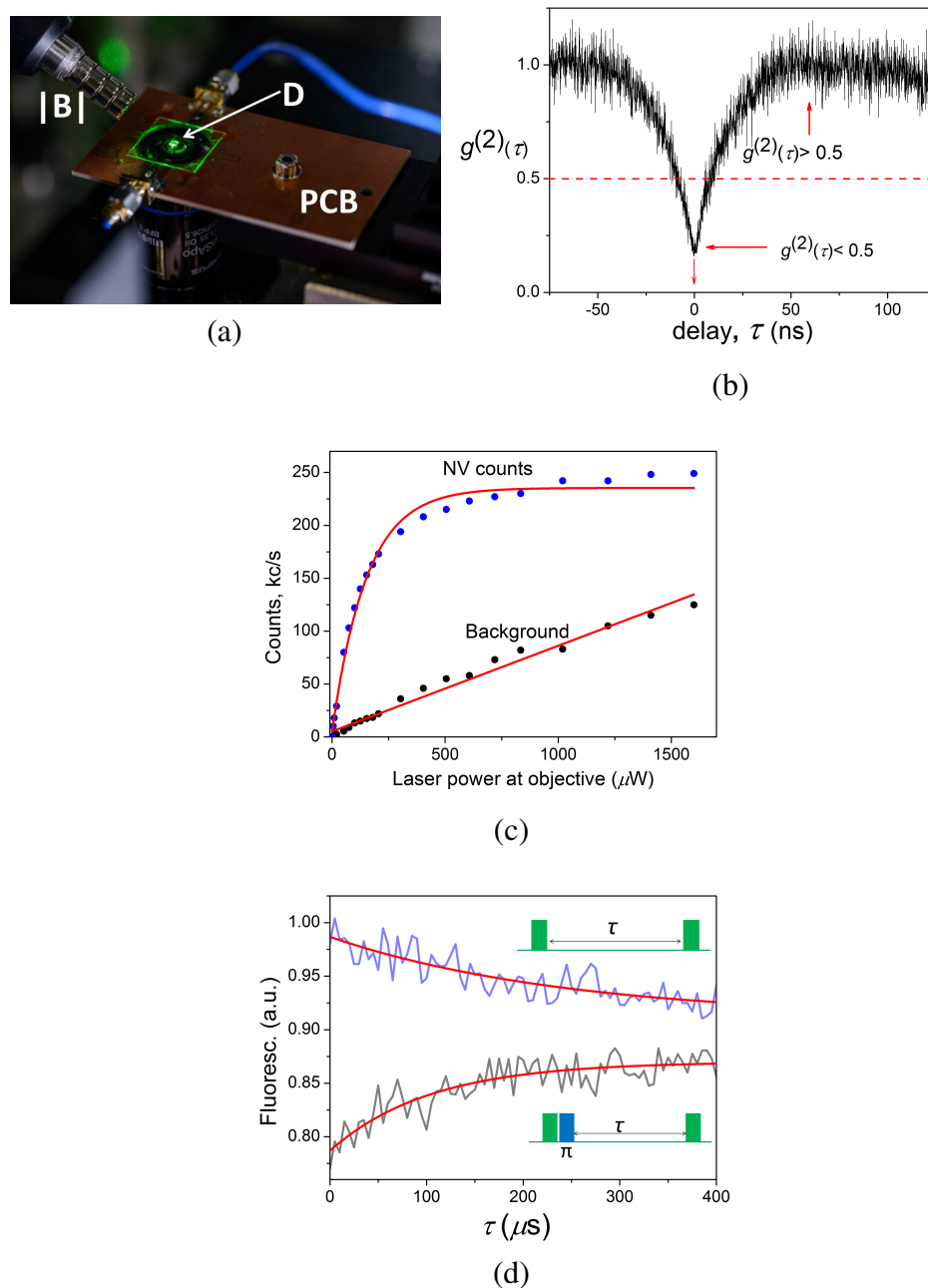
Figure 1.8: Characterization of single shallow NV. (a) A photograph of the horizontal experimental setup showing the diamond sample (D) mounted on a PCB stripline. |B| is provided by the permanent magnet and is aligned along NV axis. (b) Typical antibunching result on a single NV showing the $g^{(2)}(\tau) < 0.5$, characteristic of a single emitter. (c) NV counts (in 1000 counts per s) as a function of green laser power measured at the sample. Plotted alongside is the background counts. (d) Typical T_1 measurement showing a value of $\sim$200 μs. Blue and black lines are data points and red lines are fit to exponential decay. Insets shows the experimental pulse sequence used to acquire the data.

The resulting light enters 50:50 beam-splitter (BS) cube and the halved light intensities are focused onto two separate single photon counting avalanche photodiodes (APD) using lenses. The APDs are mounted on 3D stages to precisely align the optics. The photon signals arriving at the APDs are counted using a fast counting module (MCS6A, MCS) for recording time trace and further analysis of signal on the computer.

The two APDs (SPCM-AQRH, $Excelitas$) operating in Hanbury Brown and Twiss anti-bunching configuration [98] are used to ascertain whether a given emitter is a single NV center or not. The emission of photons by a single NV center can be described by a second order autocorrelation function of the fluorescence intensity,

$$g^{(2)}(\tau) = \frac{\langle I(t)I(t+\tau)\rangle}{\langle I(t)\rangle^2} \qquad (1.3)$$

where, $I(t)$ is the fluorescence intensity at a given time t and τ is the delay time between the two APDs, and $\langle ..\rangle$ denote the time average. For a delay $\tau \to 0$, the value of $g^{(2)}(\tau)$ should be zero, if the emitter is a single NV center since a single emitter can not emit two photons at the same time. It is known as antibunching effect. On the other hand, if we have a pair of emitters contributing to $I(t)$ then there is an equal probability of detecting two photons by the APDs at the same time and the value of $g^{(2)}(0) \to 0.5$. Therefore, normally a $g^{(2)}(0) < 0.5$ is sufficient to establish the presence of a single NV center (figure 1.8b). This point is important for the NV centers close to the surface because they contain more background fluorescence than the bulk NV, which leads to relatively higher $g^{(2)}(0)$ values. Values of $g^{(2)}(0) > 0.5$ correspond to more than one center and it is called bunching effect.

The count rate of detected photons from the single NV center critically depends on the detection optics and it is important to have a good count rate to obtain decent signal-to-noise-ratio (SNR) in the experiments as it determines the spin contrast. With our setups, normally a saturation NV count rates of $\sim$250,000 per second for an excitation laser power of $\sim$1 mW at the sample (figure 1.8c) is obtained. As the counts from the background increases linearly with the laser power, thus contributing to reduced spin contrast, an optimum range of power-count rate must be determined. For the experiments mentioned in the thesis the power was kept around 0.5 mW which would result in 150-200k counts/s. Also, since the count rate from a single NV center is weak compared to ambient light, the whole detection optics is built with suitable shielding arrangements.

The detected photon signal from APDs are sent to I/O device for confocal imaging of the diamond and tracking the NV center over time.

Out of the two experimental setups only one has an antibunching configuration while the other setup has single APD for signal detection. The experiments reported in the Chapter Two were performed in the former while the experiments of Chapter Three were done in the latter. In the setup without antibunching arrangement, the single NV centers were isolated based on the average counts of NV centers and signatures of their ODMR (section 1.4) spectra.

1.3.2 Microwave (MW) part

A two-channel arbitrary waveform generator (AWG70002A, Tektronix) operating at a sampling rate of 20 Gsps is the main control unit of the experimental setup. MW pulses

produced at the channel-1 (CH1 in figure 1.7) of AWG, for example, are amplified using a 16W high power amplifier (ZHL-16W-43+, $Mini-circuits$) and applied to the sample. The channel-2 (CH2) could be used to additionally generate RF signals, if required by the experiment and were mostly used without further amplification. The synchronization of the optical pulses, MW pulses for NV manipulation and associated readout of NV signal in a given experimental pulse sequence is achieved with marker signals (m1& m2) of AWG and a pair of MW switches (ZASWA-2-50DR+, $minicircuits$) to route them sequentially. For generating laser pulses, a known voltage from m1 is applied to the AOM through RF driver for a required duration. Similarly using m2 the MCS counting can be turned On/Off. All the commands to AWG are sent through the programs written in MATLAB.

Figure 1.8a shows the photograph of sample stage. The diamond sample is mounted on a coplanar MW waveguide made of PCB. The sample is first glued onto a 170 μm microscope cover glass and the glass-diamond assembly is then fixed on the PCB which has a wide hole of 25 mm diameter to allow for the objective move freely. The PCB is fixed to 3D stage and keeps the sample stationary while the objective scans and repositions itself for tracking the NV centers. Depending on the experiments at hand the mounting methods varied (as explained in the respective chapters). But, essentially the MW excitation is achieved using thin microwires (Cu or Au) soldered across the sample. In some cases, if the fast driving of the NV spin was necessary, lithographically patterned micro structured antennas on cover glass were used in place of microwires. The amplified MWs are applied through the co-axial cable at one end of the PCB and at the other end, the MW power could be measured after attenuation (with a 20W attenuator).

The static magnetic field (|B|) required to split the degeneracy of the NV center's spin levels is provided by a permanent (Neodymium) magnet. The magnet is fixed to a 3-axis kinematic mount to adjust the angle of field and the whole mount is fixed on a one-axis linear stage (PT1/M, $Thorlabs$). The position of the magnet is adjusted manually (to increase or decrease the |B|) using this linear stage which has a resolution of 10 μm. The angle of |B| is set to 54.7° with respect to normal to the (100) surface of the diamond. This angle coincides with one of the four [111] axes of the NV. The alignment of the field along the NV axis is carried out by reaching the ES-LAC ($\sim$500 G) and maximizing the fluorescence.

1.3.3 About diamond samples

1.3.3.1 Fabrication of shallow NV centers

For all the experiments mentioned in the thesis, NV centers located close to the surface of the diamond were utilized, unless otherwise mentioned. For applications involving NV based sensing of external weak signals, it is a prerequisite to have the probe NV centers close to the target as the NV-target coupling scales with the inverse of their distance cubed (see section 1.5.4). For sensing applications, it is also important to have NV center's surrounding free from excessive noise sources such as those from the intrinsic nitrogen content[N]. Hence, ultrapure CVD synthesized diamonds (type IIa) with low ($\leq$ 1ppm) [N] is preferred. The NV centers formed during the CVD growth will be present at random locations in the bulk of the diamond and there will be very few NV centers close to the surface. This results in very low concentration of NV centers available for sensing

(a)

(b)
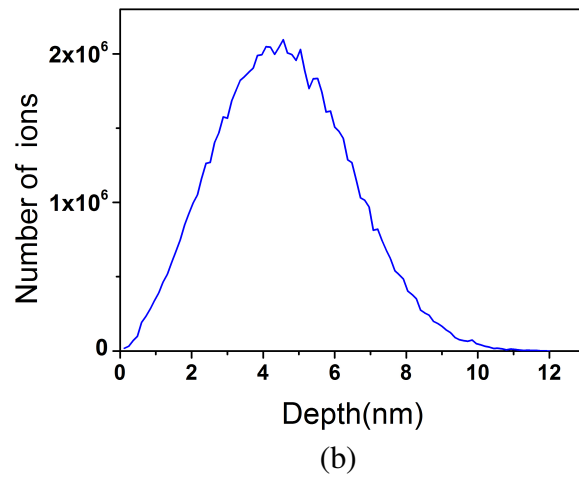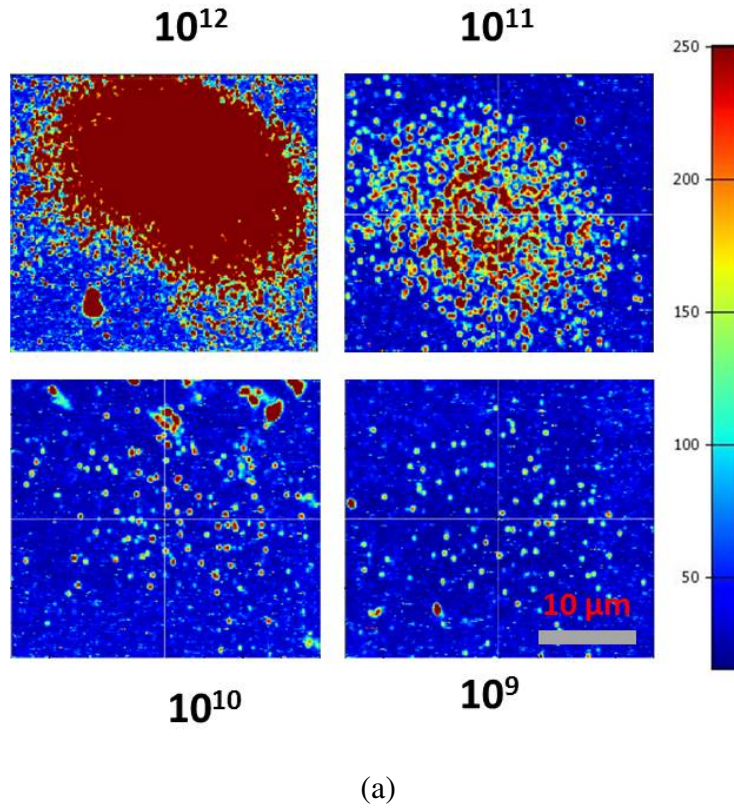
Figure 1.9: (a) A confocal map shallow NV centers produced by different implantation dosages (in units of ions/cm^2) of ^{15}N ions. Single NVs could be isolated more easily only in 10^9 dosage spots. (b) SRIM simulation results of 10^9 spot indicating average depth of the ions of $\sim$5 nm.

applications and lack of freedom in readily switching from one NV to another. To overcome this problem one can artificially engineer the NV centers in ultrapure (or isotopically pure) diamonds by two methods: nitrogen delta doping [99, 100] and nitrogen ion implantation [101, 102].

For the present work, NV centers were produced by low energy implantation of ^{15}N ions and subsequent high temperature annealing under vacuum. The rare isotope ^{15}N was chosen instead of naturally abundant ^{14}N in order to distinguish the implanted NV centers from native ones.

The diamond samples used for implantation were commercially obtained from $element6$ and had dimensions of $3mm \times 3mm \times 0.3mm$. The samples belonged to type-IIa category and had a 1.1% of ^{13}C concentration. Prior to implantation, the samples were thinned down to about 100 μm by polishing. This thinning provides several advantages: namely, it helps in imaging the implanted side by looking through the diamond from its other side as the total thickness is now within the working distance of the objective used. As the diamond is looked through from non-implanted side, various samples (containing target spins) that need to be studied could be brought in direct contact with the surface without being contaminated with the immersion oil, which is only present at the other side. Further, bringing immersion oil in contact with the shallow NV centers results in unstable behaviours of NV centers, possibly due to continuous exchange of free charges present in the oil and thus leading to charge state switching between NV$^-$ and NV^0.

The focused ion implantation of ^{15}N was performed using a nano-implanter device (SPECS IQ 12/38, $Surface Nano Analysis GmbH$). By adjusting the kinetic energy (from keV to MeV) of the implantation ions the depths of the NV centers could be tuned. For producing NV centers at shallow depths the required energy is in few keV. For the present case, an energy of 2.5 keV was used, which would result in mean ion depths of about 5 nm below the surface with an uncertainty known as ion-straggling of about 2nm. The implantation was done on several samples with a fixed energy (2.5 keV) but with varying number of ^{15}N ions and sizes of implantation spots. The number of ions, also known as dosage is calculated by the product of nitrogen flux and implantation time. The dosages were varied from 10^{12} to 10^9 ions/cm^2 and diameters of approximately circular spots varied from $\sim$30 μm upto 1 mm in some samples.

It is known that as the ion penetrates through the diamond, it knocks out native carbon atoms and produces interstitials and vacancies along its path before being finally stopped. Ion implantation also induces significant crystal damage and strain in the lattice which leads to deterioration of NV spin properties [103, 104]. High temperature annealing of the implanted diamond is carried out to combine the nitrogens and vacancies to form a stable N-V pair and to mitigate the crystal damages. Since even at high temperatures the nitrogen atoms do not move, for the formation of N-V defect centers the vacancies have to move and combine with the nitrogen. As the vacancies become mobile only at temperatures >600° C, a high temperatures annealing is necessary [105]. At high temperatures the vacancies can also diffuse and repair the crystal damages.

The annealing was carried out using a vacuum system (minicoater, $tectra$) equipped with heater and a thermocouple. The samples were subjected to temperatures upto 800° C while maintaining a high vacuum of $\approx 10^{-7}$ mbar. High vacuum is necessary in order to avoid the etching and graphitization of diamond in the presence residual gases at high
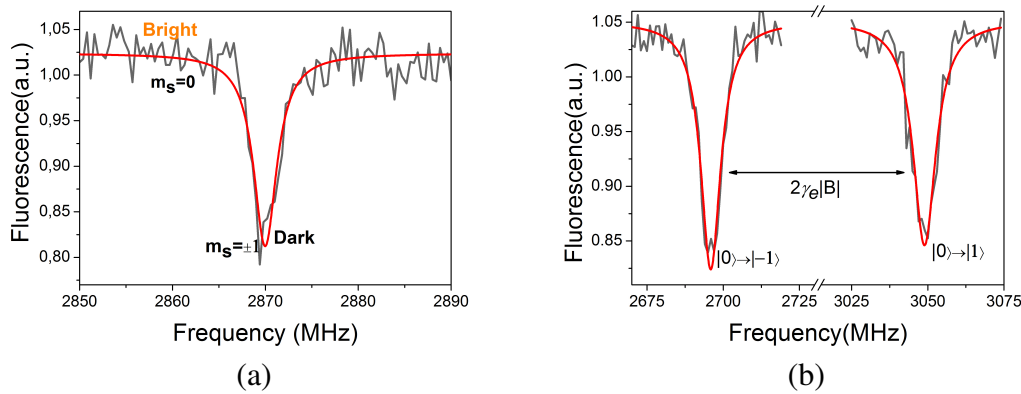
Figure 1.10: (a) ODMR at zero external magnetic field (|B|=0). (b) ODMR at a non-zero field (|B|≈ 65 G). The data (black lines) are fit to Lorentzian function.

temperatures. The annealing was done by slowly ramping from room temperature to $800°$ C in steps of $100°$ C and each step had a duration of 60 minutes. From $800°$ C the temperatures ramped down to room temperature in coarse steps. The samples were then boiled in a strong tri-acid mixture to remove the graphitic and other impurities adsorbed to the surface.

The quality of implantation is determined by measuring the ratio between number of NV centers produced and number of ions implanted, also known as implantation yield. Due to the low energy (keV) of implanted ions, the number of vacancies produced is less and hence the eventual formation of NV centers is also minimum. We estimated that our samples produced an yield of $<0.1\%$, which is typical for the energy used. Figure 1.9a shows confocal images of one sample with varying dosages of implantation. The single NV centers appear as diffraction-limited spots and could be more easily isolated near the periphery of dense spots or from the low dosage spots. An average depth of the produced NV centers can be estimated by calculating the 'Stopping and range of ions in matter' (SRIM) [106]. In our case (2.5 keV) the average depth[5] was found to be about 5nm (figure 1.9b). These NV centers exhibit decent spin properties and often show spin relaxation (T_1) times of 100 μs to 1 ms (an example is shown in figure 1.8d and T_1-concept is described in section 1.4.1).

1.4   Electron Spin Resonance on NV center

The fact that the electron spin associated with the NV center exhibits Zeeman interaction with the $\vec{B}$ resulting in a energy splitting of its spin sublevels proportional to |B| allows us to perform traditional electron spin resonance (ESR) experiments. Besides, the spin state-dependent fluorescence of NV enables us to detect the ESR transitions by optical means. The first experiments on the optically detected magnetic resonance (ODMR) on single NV spin was demonstrated by Gruber et all [107]. The basic measurement scheme is shown in the figure 1.10. Under zero applied field (|B| = 0), the GS is split by D_{gs} and

---
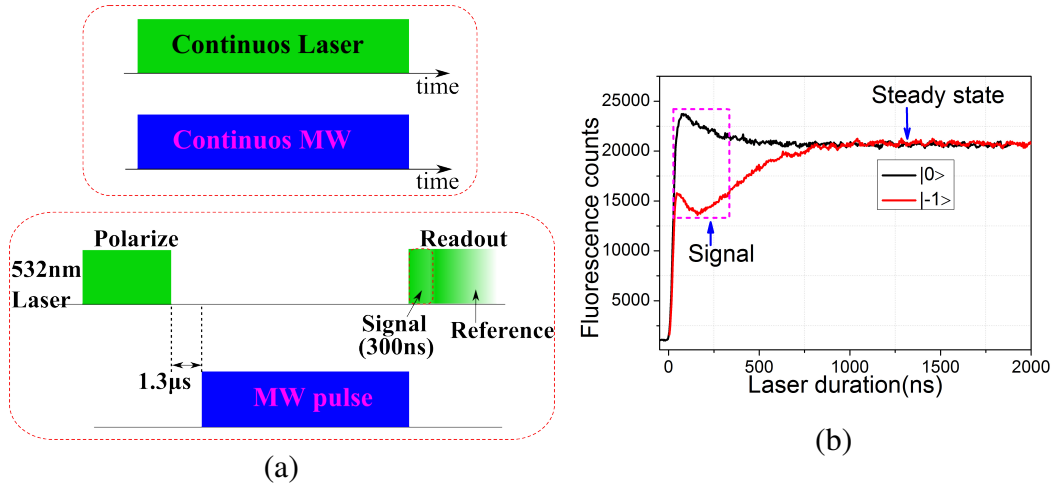
Figure 1.11: (a) Schematic of the CW-ODMR (top) and the pulsed ODMR (bottom) measurements. (b) Time-resolved PL of NV center. The measured 'Signal' corresponds to fluorescence counts-difference in the first ∼300ns time-window normalized with the steady state value.

optical excitation produces a spin polarization in the $m_s = 0$ of the GS. The NV shows maximum fluorescence and hence it is in 'Bright' state. A resonant MW radiation equal to D_{gs} will transfer some of the population from $m_s = 0$ to degenerate $m_s=\pm 1$ level. The subsequent optical excitation causes these population to undergo shelving into long-lived metastable states and eventual drop in fluorescence as explained in the section 1.2.1.2. The spin is now said to be in the 'Dark' state. So, when the spin is initially polarized into $m_s = 0$ level, if the MW is swept across the D_{gs} we get 'Dark' state for resonant frequency and 'Bright' state for all other non-resonant MW frequencies (figure 1.10a).

When a magnetic field $\vec{B}$ is applied along the NV-axis, the $m_s=\pm 1$ couple to $\vec{B}$ and split into two levels separated by a Zeeman energy of $\Delta E \sim 2\gamma_e|B|$. Now, if the MW frequency is swept, instead of a single resonance dip we will observe two dips in the fluorescence according to $|0\rangle \rightarrow |-1\rangle$ and $|0\rangle \rightarrow |+1\rangle$ resonant transitions (figure 1.10b). The corresponding transition frequencies are given by $\nu_- = D_{gs} - \gamma_e|B|$ and $\nu_+ = D_{gs} + \gamma_e|B|$, respectively. Therefore, by measuring the ν_- and ν_+ from an ODMR experiment we can estimate the external DC field along the NV-axis. Since an NV-axis points along one of the four crystallographic [111]-directions in diamond, ODMR on one NV center can give information about $\vec{B}$ along one of these axes. If we use an ensemble of NV centers then we can have NV centers pointing their axes in all four directions. Therefore, by measuring the ODMR on all four directions one could measure the magnitude and direction of $\vec{B}$. Thus, NV centers can be utilized as vector magnetometers for the reconstruction of the external $\vec{B}$ profile [108, 109].

There are two modalities of ODMR measurements, namely the continuos wave (CW) ODMR and pulsed ODMR (figure 1.11a). In the CW-ODMR, the NV center is continuously excited with the green laser and the MW is applied simultaneously. The ODMR spectrum is recorded by sweeping the frequency of the MW around the resonance and measuring the corresponding fluorescence. This method is the most straight forward way to measure the DC field but it lacks the sensitivity (discussed in later section).

In the pulsed ODMR method, the NV center is polarised into $m_s=0$ state with an initial

laser pulse of known duration $\sim$3 μs. Then, a MW pulse of fixed duration is applied in the absence of any laser excitation, and finally the NV spin state is readout with a second laser pulse (figure 1.11a). The sequence is repeated by sweeping the frequency of the MW pulse and the ODMR spectrum is recorded. The readout laser pulse in each sequence also serves the initialization pulse for the subsequent sequence. Crucially here, the fluorescence signal photons are collected only during the first 300 ns of the readout laser. The reason for this can be explained by analyzing the time-resolved photoluminescence (PL) of the NV center shown in the figure 1.11b. At the end of the MW pulse if the NV spin state is in m$_s$=0 ('Bright') state then initially high PL counts are observed. But due to the finite (though small) probability of m$_s$=0 state in the ES to undergo ISC to long-lived singlet states the PL intensity decays and reaches a steady state value. In case at the end of the MW pulse the spin state was in m$_s$=$\pm$1 ('Dark') state then a relatively lower PL counts is observed due to spin-state dependent optical contrast. Due to the fast ISC rates of m$_s$=$\pm$1 state into singlets, the PL decreases sharply in the beginning and then decays towards steady state value as the system preferentially relaxes to m$_s$=0 state. This decay happens within the lifetime of the metastable singlet state ($\sim$250 ns). Therefore the actual signal corresponds only to be the difference in PL values of m$_s$=0 and $\pm$1 in this time-window of $\sim$300 ns. The NV spin state can thus be measured by normalizing PL value in this window with the steady state PL value. Note that for each pulse sequence normally a waiting time of 1.3 μs between the initialization laser pulse and the MW pulse is used in order to allow the steady state population trapped in the metastable singlets to relax to the m$_s$=0 state.

The pulsed ODMR sequence just explained forms a most basic and general scheme of various ESR measurements that can be performed on the NV centers. It can be extended to realize other ESR experiments on the NV centers by having a block of MW pulse sequence for the manipulation of the NV spins instead of a single MW pulse between the two laser pulses.

Due to the low collection efficiency of the photon detection optics, the 300 ns measurement window results in very small number of photons that is available for the spin state read-out per pulse sequence. Thus, it is necessary to repeat the sequence $\sim$10^6 times to achieve a good SNR.

1.4.1 NV spin relaxation times

For describing the spin relaxation of NV centers some essential ideas from the traditional Nuclear Magnetic Resonance (NMR) have been employed. In NMR, the net magnetization $\vec{M}$ precesses about an external static field $\vec{B}$ with a Larmor frequency ω_L=γ_n|B|, where $\omega_L = 2\pi f_L$ with f_L being the Larmor frequency (in Hz) and γ_n is the gyromagnetic ratio of the precessing nuclei [29, 110]. The vector M can be resolved into its time-dependent components along three orthogonal directions, $M_x(t)$, $M_y(t)$ and $M_z(t)$. $M_x(t)$ and $M_y(t)$ are transverse components, and $M_z(t)$ is a longitudinal component. By assuming M precesses along a cone around $\vec{B}$ with time t, the components $M_x(t)$ and $M_y(t)$ rotate sinusoidally around $\vec{B}$ while $M_z(t)$ stays constant. Bloch equations describe the interaction of these components with $\vec{B}$. The solutions to Bloch equations lead to following simplified

expressions for the longitudinal and transverse components,

$$M_x(t) = M_0 e^{-\frac{t}{T_2}} \sin(\omega_L t),$$
$$M_y(t) = M_0 e^{-\frac{t}{T_2}} \cos(\omega_L t), \tag{1.4}$$
$$M_z(t) = M_0(1 - e^{-\frac{t}{T_1}})$$

Where, M_0 is the equilibrium magnetization. The two decay/time constants, T_1 and T_2 are called longitudinal and transverse relaxation time, respectively. The T_1 relaxation (also known as *Spin-lattice relaxation* in case of solid samples or simply T_1 relaxation in case of liquids under study) is the time required for M to return to its thermal equilibrium value (M_0). The T_1 decays on a relatively longer time-scale of seconds in most samples. T_1 relaxation originates from the exchange of energy between the precessing spins and their surroundings. In case of solids this can happen through the dissipation of energy of the system into the excitation of lattice vibrations or phonons.

The T_2 or transverse relaxation is the process by which the transverse components decay exponentially from their initial maximum value (M_0) in the transverse plane. T_2 relaxation can also be visualized as a gradual loss of phase coherence between precessing M_x and M_y components due to the fluctuating field (ΔB) caused by the spin-spin interactions. Hence the T_2 time is also called as *Coherence time*. Unlike the T_1 relaxation the T_2 relaxation does not involve the exchange of energy with the environment but rather increase of entropy of the system. Generally, the T_2 decays on a faster time scale than the T_1 and any processes which cause T_1 relaxation also destroy the coherence in the transverse plane. Therefore, the upper limit for T_2 is set by the T_1.

Extending these concepts to NV centers, the T_1 relaxation is the time-scale in which the optically polarized NV spin population[6] returns to its equilibrium value from m_s=0 level. Also, it is equivalent to time scale in which the population from m_s=±1 level decays to equilibrium after being transferred from m_s=0 to m_s=±1 level. Since the $\vec{B}$ is applied along the z-axis it is taken as the longitudinal direction while the x and y as transverse directions. Once the spin is polarized along the z-direction it can be brought to xy-plane with a resonant MW pulse where it precesses about the $\vec{B}$ with Larmor frequency ($\omega_{NV} = \gamma_e |B|$). The T_2 relaxation refers to the exponential decay of spin coherence in the transverse (xy) plane. Therefore, while T_1 is the time scale in which the spin flips happen between m_s=0 and m_s=1 Zeeman levels, the T_2 is the loss of phase information in the transverse plane.

Owing to the high Debye temperature, the diamond lattice has very low phonon density of states even at room temperature. This implies that the coupling of the NV spin to lattice vibrations is highly minimized which results in the long T_1 times (ms time scale) of the NV center. Albeit small, the non-zero interaction of the NV electron's orbital states with the lattice vibrations leads to spin-lattice relaxation of the NV center. The T_1 relaxation of NV shows strong temperature dependence- from $\sim 10^2$ s at low temperatures (<100 K) to a few milliseconds at room temperatures [111, 112]. It is identified that at high temperatures two-phonon Raman and Orbach-type processes, and at low temperatures

---

[6]The term 'population' in case of single NV center refers to the repetitive measurement on the single spin, whereas in NMR it applies to ensemble of nuclear spins.

the cross relaxation due to Nitrogen nulcear spins are the main sources of T_1 relaxation [111–113].

The transverse relaxation of NV centers originates from the interaction of the NV spin with randomly fluctuating ΔB created by a bath of ^{13}C nuclear spins and paramagnetic impurities (known as P1 centers) such as electron spins associated with Nitrogen (N) atoms in bulk diamond. This is characterized by a *spin dephasing time* (T_2^*) time. In CVD diamonds with natural abundance ^{13}C (1.1%) and N concentration $\simeq 1$ ppb, the T_2^* values are nearly a few μs. By synthesizing the isotopically pure diamonds (ultra low concentration of ^{13}C) and depleting the crystal of paramagnetic impurities the T_2^* can be extended upto hundreds of μs [16, 20, 114]. The decay of the actual transverse relaxation happens on a much longer (T_2) time-scale than T_2^*. Using the spin manipulation experiments known as dynamical decoupling methods T_2 times can be further extended to ms time-scale, almost on par with the T_1 over a wide range of temperatures [92, 115–119]. Nevertheless, T_1 sets the ultimate limit of the spin relaxation time such that $T_2^* < T_2 < T_1$.

1.4.2 Coherent manipulation of NV spin

1.4.2.1 Rabi oscillations

One of the advantages of the pulsed ODMR scheme is that it enables us to perform the spin manipulation coherently. As the MW is applied in the absence of laser, the spin phase memory is retained during its manipulation unlike in CW-ODMR where the spin is continuously excited and thus would have led to loss of coherence.

The NV spin has triplet GS, i.e., in the presence of a $\vec{B}$ along z, we get m$_s$= 0, -1 and 1 states. We use m$_s$= 0 and one of m$_s = \pm 1$ levels, for its manipulation. Thus we have an effective two level system forming a spin 'qubit'. Its spin dynamics can then be represented by a vector on a unit sphere known as Bloch sphere whose north and south poles coincide with $|0\rangle$ and $|-1\rangle$ eigenstates, respectively. In the pulsed ODMR experiment discussed above the population was transferred from north to south pole when a resonant MW oscillating in the equatorial plane was applied. Therefore, if we perform ODMR experiment by sweeping the duration (τ) of the MW pulse while keeping its resonant frequency (ν_1) constant, the spin continuously moves over the Bloch sphere (figure 1.12a). This results in the periodic oscillations of the fluorescence signal between 'Bright' and 'Dark' states (figure 1.12b). These oscillations are known as Rabi oscillations and the corresponding frequency, Rabi frequency (Ω_R). Ω_R depends on the applied MW power (P_{MW}) as $\Omega_R \propto \sqrt{P_{MW}}$ .The Rabi contrast ($\sim$30%, the spin-state contrast) is the peak-to-peak amplitude in the fluorescence oscillation. In the Bloch sphere picture a resonant MW pulse whose τ brings the spin vector from its initial z-axis to xy plane is called as a $\pi/2$-pulse (figure 1.12a) and the spin is now said to be in an equal coherent superposition of $|0\rangle$ and $|-1\rangle$ states. If the τ of the MW is such that it transfers the spin between $|0\rangle$ and $|-1\rangle$ then the pulse is called as a π-pulse and is responsible for the complete state transfer between the two levels. Hence, a Rabi experiment serves as a calibration of the system to apply MW pulses for further ESR experiments.

In the superposition state, the spin state can be expressed as,

$$\Psi = \frac{1}{\sqrt{2}}(|0\rangle + e^{i\phi}|-1\rangle) \tag{1.5}$$

29

(a)

(b)
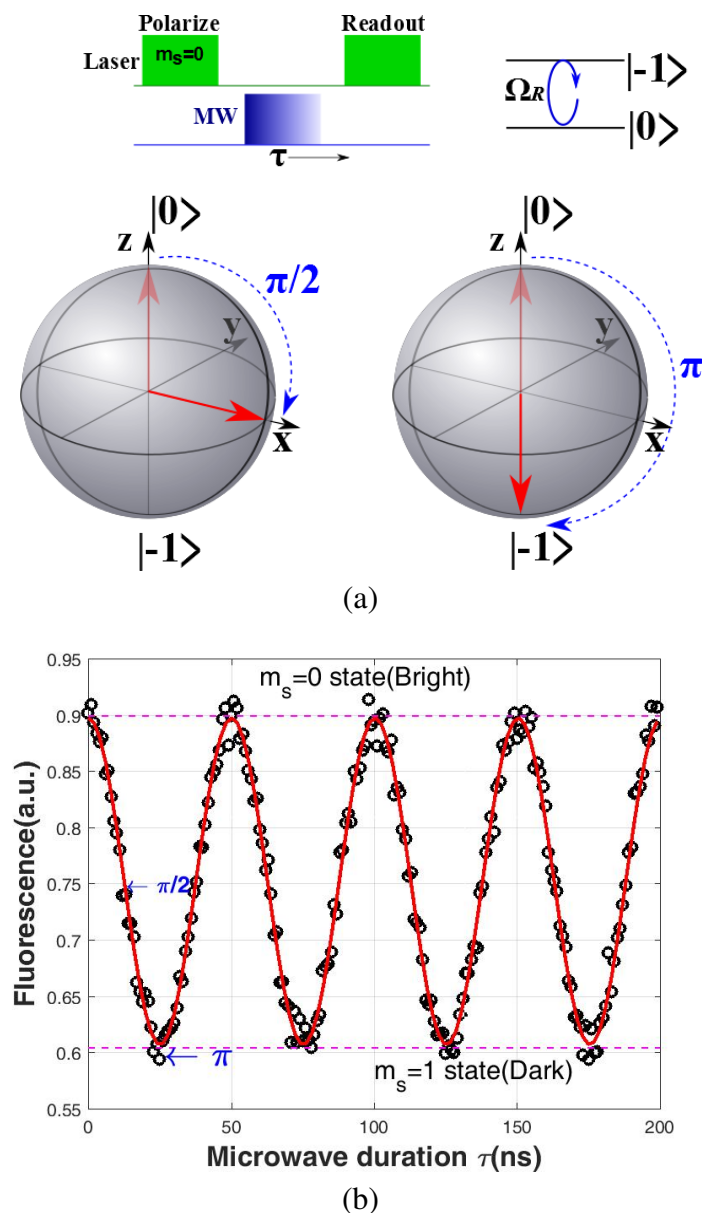
Figure 1.12: Measurement of coherent Rabi oscillations of NV center. (a) Experimental pulse sequence (top) and Bloch sphere illustration of the NV-spin dynamics during Rabi driving (bottom). The MW is applied along the $+y$-direction and the blue dotted arrow indicates the path of the spin vector during the Rabi driving. (b) Experimentally measured Rabi oscillations of a single NV center. The $\pi/2$ and π pulse duration are indicated. The Rabi contrast is the difference between signal's minimum and maximum (dotted lines) value. Black circles are data and the red line is fit to a cosine model yielding $\Omega_R \approx 20$ MHz.

where the phase $\phi = 0$ corresponds to x-axis and $\phi = \pi/2$ to y-axis. The coherent evolution of the spin in its superposition state is sensitive to the presence of additional static and oscillating magnetic fields. As a consequence the NV spin can be used as a quantum sensor for detecting small fields as explained in the following section.

1.4.2.2 Ramsey experiment

The Rabi oscillations described in the previous section are due to driven spin dynamics. By transforming the spin to equal superposition of $|0\rangle$ and $|-1\rangle$ states and letting it evolve freely (i.e., MW is switched off) for a period τ, we can observe the undriven or free spin dynamics. This can be accomplished by applying another $\pi/2$-pulse which puts the spin back into its $|0\rangle$ state and readout with a second laser. This is represented by a simple pulse sequence, $\pi/2 - \tau - \pi/2$ known as Ramsey sequence (figure 1.13a). The sequence is repeated many number of times in order to collect sufficient SNR.

If a small additional static field is present, it shifts the Zeeman sublevels of the NV spin. Hence, the NV's transition frequency given by $\nu_- = D_{\text{gs}} - \gamma_e|\text{B}|$ is slightly detuned by $\delta\nu = \gamma_e \Delta\text{B}$. In the superposition state, if the spin is allowed to freely precess under the influence of this detuning field ΔB for a duration τ, we observe oscillations in the resulting fluorescence signal with 2π periodicity. The oscillation frequency corresponds to $\delta\nu$. These oscillations are called as Ramsey fringes. The Ramsey signal decays on a time scale of T_2^* or spin dephasing time (mentioned in section 1.4.1) [16, 91, 120]. This is also called as *free induction decay* (FID) signal in analogy with traditional NMR. Figure 1.13b shows an example of Ramsey signal decay for a shallow implanted NV center at a low |B| and its Fourier transform is presented in the figure 1.13c. The measurement was carried out with a MW detuning ($\delta\nu$) of 10 MHz from the resonance frequency.

Experimentally, due to the HF interaction of the NV spin with the nitrogen atom of the vacancy, typically a beating of the Ramsey signal is observed at low applied static field. The Fourier transform of the signal shows three lines ($\delta\nu$+2.2 MHz, $\delta\nu$ and $\delta\nu$-2.2 MHz) in case of ^{14}N, and two lines, $\delta\nu$-3.05 MHz or $\delta\nu$+3.05 MHz in case ^{15}N (figure 1.13c). This is because, due to HF coupling, NV now forms three (two) independent two level systems with the host ^{14}N (^{15}N). The data can thus be modeled by a summation over all the observable frequencies with a Gaussian-decay envelope [121],

$$I(\tau) = e^{(-\frac{\tau}{T_{2*}})^2} \sum_i \cos 2\pi f_i \tau \qquad (1.6)$$

where, $I(\tau)$, is the fluorescence signal as a function of τ and f_i is the ith frequency component.

As mentioned in the section 1.4.1, the decay of the Ramsey signal over T_2^* time scale originates from the dipolar interaction of the NV spin with the fluctuating magnetic field (ΔB_{bath}) created by a bath of nuclear spins surrounding the NV center. In diamonds with natural abundance (1.1%) of ^{13}C, the main source of nuclear spins is randomly placed ^{13}C spins in the crystal lattice. As the Ramsey sequence is repeated many times, each measurement run gives a slightly different signal due to sporadic nature of interaction of NV with the ΔB_{bath}. The resulting averaged signal decays on a time scale of a few μs, which is much shorter than the actual coherence time (T_2). Therefore, the Fourier transform

of the FID shows a broadening of width or FWHM (Γ_2^*) of measured $\delta\nu$ by $\sim \frac{1}{T_2^*}$ (ref. [17]). This is known as the *inhomogeneous broadening*[7]. Note that this inhomegeneous broadening of a few hundred kHz (corresponding to T_2^* of a few μs) is faster than the dipolar interactions between the ^{13}C spins (0-10 kHz) [120].

1.5   Magnetic sensing with NV center

NV centers, due to their quantum nature such as the spin coherence properties mentioned in the previous section, can be called as *Quantum Sensors* [9]. NV based quantum sensing for detection of weak magnetic fields (known as magnetometry) can be broadly classified into two categories- DC sensing and AC sensing. DC sensing refers to detection of magnetic fields which are static or slowly varying, while AC sensing corresponds to detection of alternating fields or time-varying signals of frequencies usually upto 10 MHz [18]. The DC magnetometry employs ODMR (CW and pulsed) and Ramsey methods, and is essentially limited by the T_2^*. The AC magnetometry is performed by Spin-Echo based techniques which extend the T_2^* by 1 to 2 orders of magnitude to reach the T_2-limit.

1.5.1   DC Magnetometry

1.5.1.1   CW and pulsed ODMR methods

The most straight forward way to detect the external field is by ODMR experiment. As explained in section 1.4, the ODMR measures the |B| along the NV-axis according to Zeeman relation $\nu_\mp = D_{\text{gs}} \mp \gamma_e |B|$, where $\nu_\mp$ are the two resonance transitions.

In the case of CW-ODMR, the NV center is continuously excited with a green laser, and the MW is simultaneously applied and its frequency is continuously swept. Any change in the magnetic field ΔB from original will change the resonance frequency. The photon shot noise limited sensitivity, η_{DC} (in units of $T/\sqrt{Hz}$) of the method, is related to minimum detectable magnetic field B_{min} in a measurement time Δt as [17],

$$\eta_{\text{DC}} = B_{min}\sqrt{\Delta t}$$
$$\approx P_\alpha \frac{h}{g\mu_B} \frac{\Delta\nu}{C\sqrt{R}} \tag{1.7}$$

where, P_α is the numeric factor related to line shape of the ODMR transitions (0.77 for Lorentzian and 0.7 for Gaussian shape); $\Delta\nu$- FWHM of the ODMR line, known as the linewidth; C-contrast of the ODMR signal; and R- detected count rate of fluorescence photons from the NV.

As can be seen from the equation 1.7, η_{DC} in CW-ODMR is essentially limited by the linewidth $\Delta\nu$, which is given by the inhomogeneous broadening Γ_2^* of the dephasing rate $\sim 1/T_2^*$ of the NV. In addition, $\Delta\nu$ also suffers from the power broadening due to continuous optical and MW excitation used in CW method. One way to minimize the

---

[7]in analogy with terminology used in regular NMR where the broadening happens due to spatial variation of the signal in ensemble averaging.

(a)

(b)

(c)
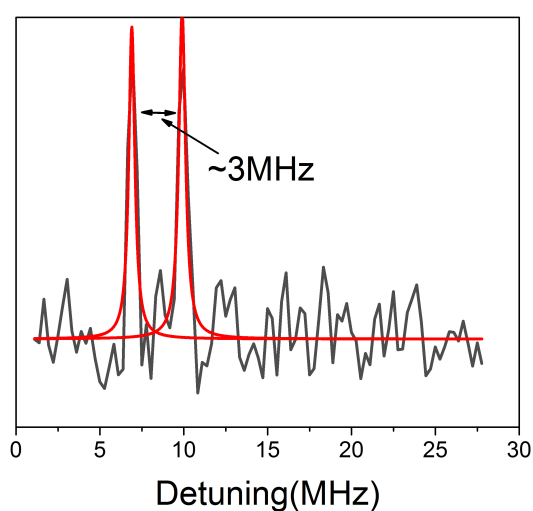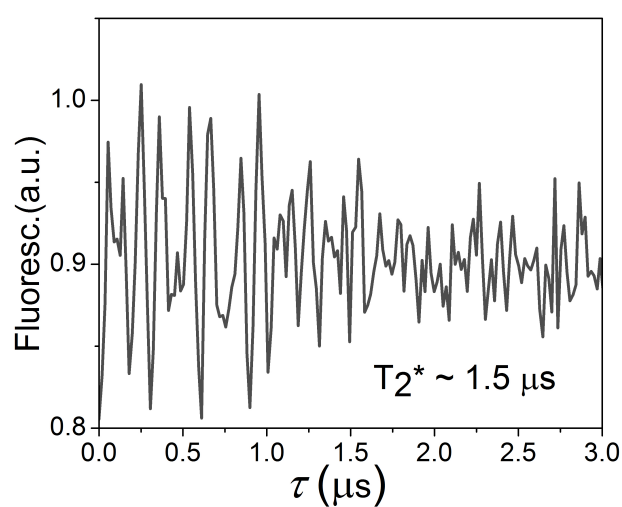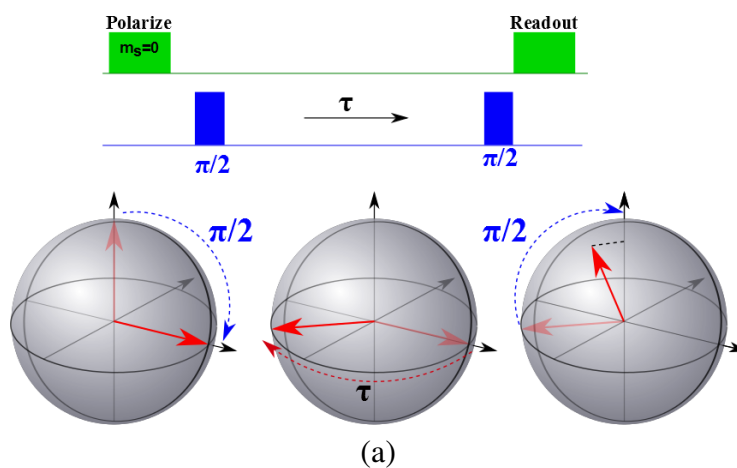
Figure 1.13: Ramsey or FID experiment. (a) Ramsey pulse sequence (top) and corresponding spin dynamics on the Bloch sphere (bottom). (b) A typical FID signal from a shallow implanted NV center. (c) In the frequency domain, the Fourier transform of the signal yielding two HF lines separated by $\sim$3 MHz corresponding to host ^{15}N spin.

33

power broadening (and hence to enhance the η_{DC}) is to use low powers for laser excitation as well as MW manipulation. But this will significantly reduce the contrast C and count rate R, and hence deteriorates the η_{DC}. The best achievable η_{DC} in CW-ODMR is therefore about 2 μT/$\sqrt{\text{Hz}}$.

In pulsed ODMR the issues of laser and MW induced power broadening can be eliminated while achieving an optimum contrast, C [17]. The laser induced power broadening is avoided in two ways: First, as the MW spin manipulation happens under dark conditions the laser induced fast dephasing of NV spin is avoided. Second, the photon measurement times are shortened to only 300 ns, equal to NV metastable state lifetime (figure 1.11b). As a result the photon counting can extract only the actual contrast of the spin state (figure 1.11b). Sufficient R can also be obtained as the laser power can now be set to NV-saturation value.

The power broadening due to MW is canceled by appropriately choosing the MW duration τ_{mw}. By setting $\tau_{mw} \approx T_2^*$, one can achieve ODMR line with an optimum contrast C_{pulse} and the linewidth limited only by the Γ_2^*. This duration of the MW corresponding to T_2^* is known as the π-pulse as it brings the complete population transfer (as in case of Rabi).

As a result, with pulsed OMDR the η_{DC} can be improved by atleast an order of magnitude compared to CW-ODMR. An expression for η_{DC} in pulsed ODMR is given by,

$$\eta_{DC} \approx \sqrt{2e} \left(\frac{\hbar}{g\mu_B} \right) \frac{1}{C_{pulse}\sqrt{R't'}} \frac{1}{\sqrt{T_2^*}} \tag{1.8}$$

where, $\hbar$-reduced Planck constant; R' and t' are rate of detected photons in CW excitation and photon collection window (300 ns) in pulsed ODMR, respectively. Though the ODMR provides a simple way of measuring DC fields, the η_{DC} are degraded due to several factors. The best achievable η_{DC} (in case of single NV) in pulsed ODMR is reported to be $\approx$300 nT/$\sqrt{\text{Hz}}$. The optimum value of η_{DC} can be obtained with a Ramsey based method discussed in the next section.

1.5.1.2 Ramsey method

The Ramsey magnetometry is based on the coherent spin manipulation method discussed in section 1.4.2.2. Here. the magnetic field is determined by measuring the relative Zeeman energy shifts of the two spin sublevels induced by static or slowly varying ΔB (detuning field). Initially the NV spin is transformed into a equal superposition of $|0\rangle$ and $|-1\rangle$ states using a $\pi/2$ pulse and allowed to precess freely (figure 1.13a).The states acquire a ΔB-dependent phase Φ during the evolution τ,

$$\Phi = \gamma_e \int_0^\tau \Delta\text{B}(t)dt \tag{1.9}$$

This relative phase Φ is then converted into population difference between the spin levels using a second $\pi/2$ pulse. The population difference is then measured via fluorescence difference and from which the Zeeman shift is estimated. For small Φ, the population difference or the magnetometer signal (S') is linearly proportional to the field, $S' \approx \gamma_e\Delta\text{B}\tau$.
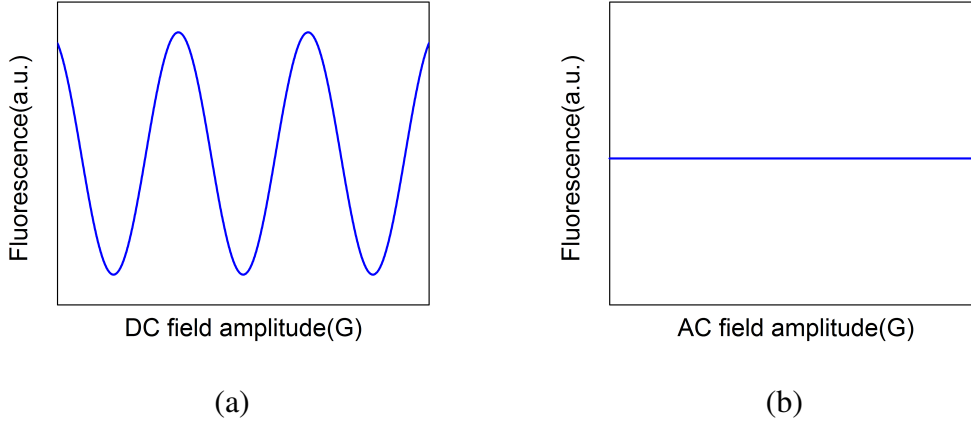
Figure 1.14: Ramsey magnetometer response for a DC field (a) and an AC field (b).

At $\tau \sim T_2^*$, an expression for optimum η_{DC} in case of Ramsey method closely resembles that of pulsed-ODMR except for a numerical factor [6],

$$\eta_{\mathrm{DC}} \approx \left(\frac{1}{\gamma_e}\right) \frac{1}{C'\sqrt{T_2^*}} \tag{1.10}$$

where $C'(\leq 1)$ is a parameter taking into account the R and contrast of the Ramsey fringes. The estimated photon-shot-noise limited η_{DC} is about 120 nT/$\sqrt{\mathrm{Hz}}$ [6]

Essentially, the Ramsey magnetometry can be accomplished by two methods. In the first method, as explained in the section 1.4.2.2 Ramsey fringes are obtained by sweeping the τ. The Fourier transform of the fringes gives the value of the detuning $\delta\nu$ and if an additional static field (unknown) is present it can be calculated by measuring the shift of this value, $\Delta B = \delta\nu'/\gamma_e$, where $\delta\nu'$ is the change in detuning from the original value. Therefore, the linewidth (FWHM) of the signal gives the resolution with which we can estimate ΔB and is limited by $1/T_2^*$.

In the second method, the τ $(< T_2^*)$ is kept constant. The amplitude of the additional field is slowly increased and the S' is recorded simultaneously. As the Φ acquired during a time τ is proportional to ΔB, the fluorescence signal oscillates sinusoidally with 2π periodicity (figure 1.14a). The minimum detectable field (B_{min}) is then obtained by the ratio of *standard deviation* over maximum of *slope* of the sinusoidally varying magnetometer signal.

While the Ramsey method is sensitive to the static or DC fields, it is inherently insensitive to the alternating or AC magnetic fields. Because, the phase Φ_+ acquired by the NV during the positive half of the signal gets exactly cancelled by the Φ_- acquired during the negative half. As a result the magnetometer response shows a flat line (figure 1.14b).

1.5.2 AC Magnetometry

For measuring alternating or AC fields, a variant of Ramsey sequence, known as Hahn-Echo or Spin-Echo (SE) sequence can be employed [9, 11, 16]. The SE sequence is formed by inserting an additional π-pulse in the middle of the Ramsey sequence. It achieves mainly
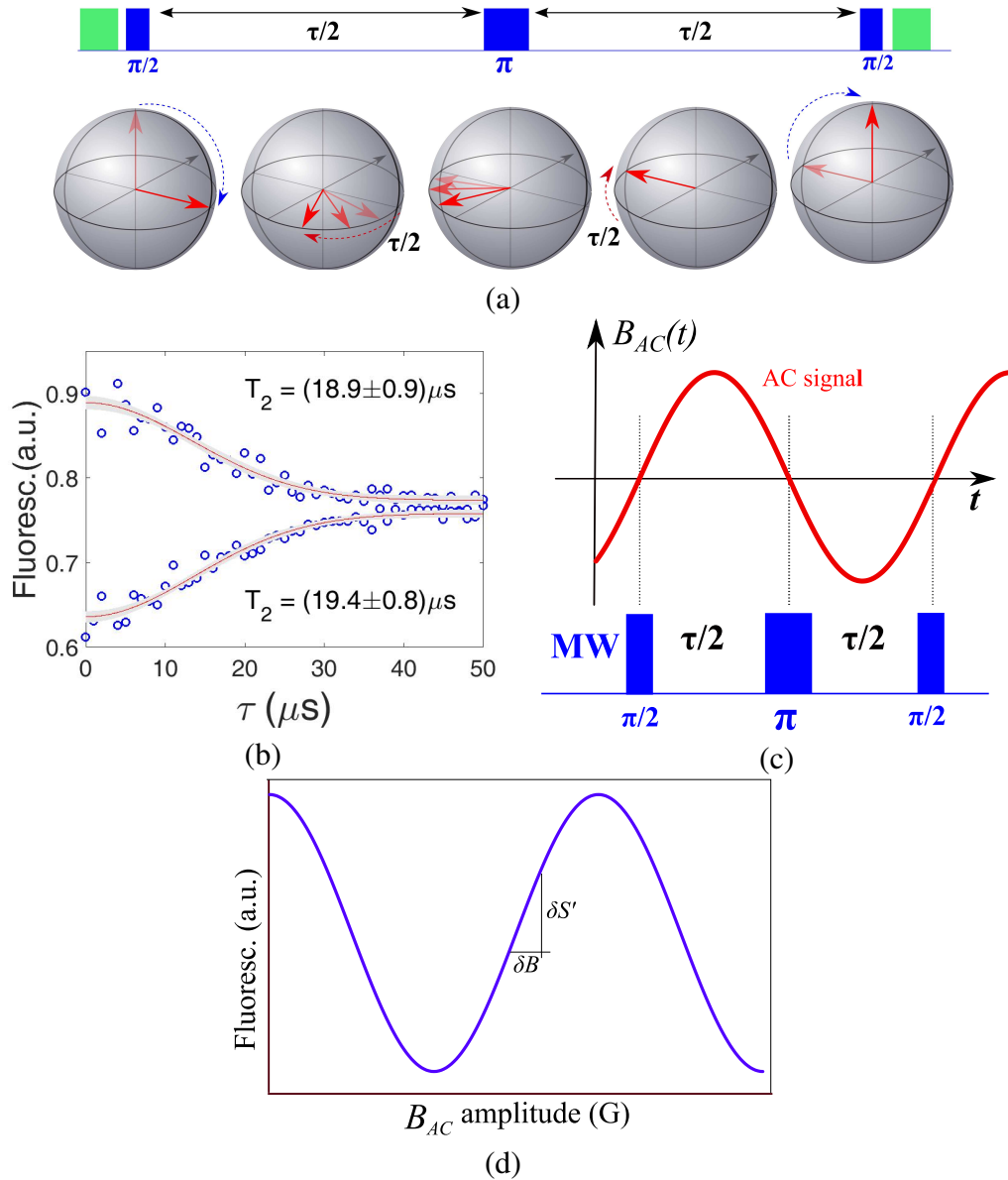
Figure 1.15: Spin Echo (SE) measurement on the NV center. (a) Spin dynamics of the NV center in Bloch sphere under an echo sequence. The MW $\pi/2$ and π pulses are applied along a same axis. (b) Typical SE measurement on a shallow implanted NV center by sweeping τ yields $T_2 \approx 20 \, \mu$s. The static field $|B| \approx 420$ G. The two curves correspond to measurements with the phases of first $\pi/2$ pulses altered by 180°. Blue circles are data points, red line is fit to the stretched exponential function and gray shaded area is the error in fit. (c) Spin Echo based magnetometry for detection of external AC signal, $B_{AC}(t)$. (d) Magnetometer signal (S') as a function of amplitude of external field B_{AC} for a fixed frequency. The magnetometer is most sensitive to B_{AC} at the maximum slope $(\frac{\delta S'}{\delta B})_{max}$ of oscillation.

two goals: One, it extends the coherence time beyond the inhomogeneous broadening value T_2^* to a substantially longer T_2. Second, one can probe the environmental noise in the range of kHz to MHz unlike Ramsey method which is sensitive to only static fields.

The pulse sequence and corresponding NV spin dynamics on the Bloch sphere are shown in the figure 1.15a. The first $\pi/2$ pulse transforms the NV center into an equal superposition of its spin sublevels. Just like Ramsey sequence, during the first free precession (MW-free) time $\tau/2$ the NV spin dephases due to inhomogeneous broadening caused by the static or slowly varying fields. The middle $\pi/2$ pulse flips the NV spin by 180º and the spin is allowed to freely evolve over second free precession (MW-free) time, $\tau/2$. Therefore, at the end of the total τ the spin is refocused back to its equal superposition state. The phase Φ acquired during first interval $\tau/2$ is cancelled by -Φ acquired in the second interval $\tau/2$. In other words the inhomogeneous broadening has been effectively cancelled by setting the two intervals equal, thus forming an echo signal [121]. A final $\pi/2$ pulse converts the coherence back to the population difference, which gives a spin state dependent fluorescence. The total Φ accumulated over one complete pulse sequence can be written as,

$$\Phi = \gamma_e \left(\int_0^{\tau/2} \Delta\mathrm{B}(t)dt - \int_{\tau/2}^{\tau} \Delta\mathrm{B}(t)dt \right) \tag{1.11}$$

As can be seen from the equation 1.11, fields which produce equal phase during the two intervals result in null net phase. Hence, SE sequence is insensitive to static (DC) fields and fluctuations which vary on time scales longer than the measurement time τ. This coherent control of the spin using the simple Hahn sequence effectively prolongs the observation time from T_2^* to T_2 by at least an order of magnitude [6, 16]. It varies from a few μs for the case of nano diamonds [117] to a few ms in isotopically engineered bulk diamonds [16]. For the case of shallow NV centers at a depth of a few nm below the surface of bulk diamond (with $1.1\%^{13}$C), the T_2 (Hahn) values are typically around 10 to 30 μs [122, 123]. Figure 1.15b shows such a measurement giving a value close to 20 μs. The data is fitted to a stretched exponential function $e^{-\left(\frac{\tau}{T_2}\right)^p}$, where the parameter p=2. This value of T_2 obtained is 10 times higher than $T_2^* \approx 2$ μs (figure 1.13b).

The SE sequence is sensitive to AC fields whose frequency f is matched to the Echo duration, f=1/τ. This allows us to probe the external fluctuating fields with sensitivity η_{AC} which depends on T_2 [6, 11, 16].

Consider a time varying magnetic signal applied along the NV axis, $B(t) = B_{AC}\cos(2\pi ft + \phi_0)$ with an amplitude B_{AC}, frequency f, and phase ϕ_0 (figure 1.15c). The π pulse is applied exactly when the signal changes its sign so that the time evolution of the NV spin happens in a reverse direction during second half of the sequence. As a result, the net acquired by the NV spin at the end of the sequence is non-zero and is given by [9],

$$\Phi = \frac{2}{\pi}\gamma_e B_{\mathrm{AC}}\tau \cos(\phi_0) \tag{1.12}$$

This Φ is converted to population difference and read out optically.

As in the case of Ramsey magnetometry, the AC magnetometry can be performed by locking the f of the AC signal to the Echo sequence and slowly ramping the amplitude of the signal. Owing to the increase in Φ, the fluorescence shows periodic modulation
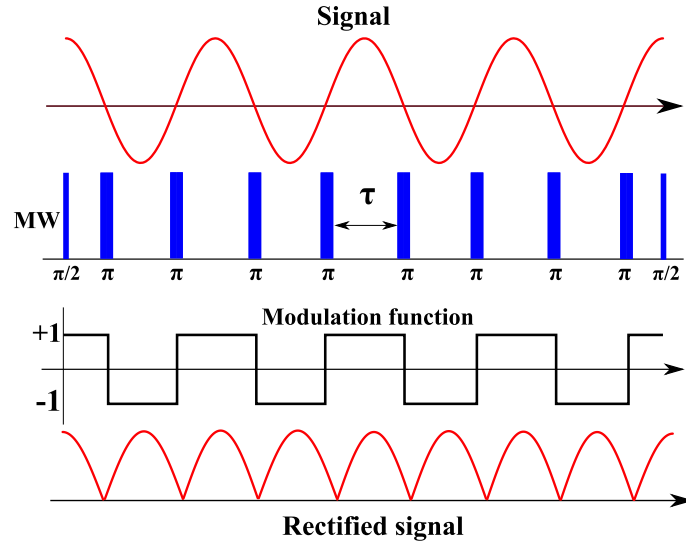
Figure 1.16: Schematic of the AC signal sensing using multipulse sequence. Locations of π pulses are made to coincide with the nodes of the signal so that maximum Φ is accumulated. Modulating function of the sequence periodically inverts the NV spin resulting in a rectified DC signal.

(figure 1.15d). The minimum detectable field B_{min} is estimated from $\sigma_s/\left(\frac{\delta S'}{\delta B}\right)_{max}$, where σ_s-standard deviation of the magnetometer signal (S') and $\left(\frac{\delta S'}{\delta B}\right)_{max}$ is the maximum slope of its response. The photon shot noise limited sensitivity η_{AC} for a measurement time τ is then given by [6],

$$\eta_{\text{AC}} = B_{min}\sqrt{\tau} \approx \frac{\pi}{2}\frac{1}{\gamma_e C\sqrt{T_2}} \tag{1.13}$$

Comparing this with the equation 1.10, since $T_2 \gg T_2^*$, the sensitivity is improved by a factor of $\approx \sqrt{\frac{T_2^*}{T_2}}$. Currently the best achieved η_{AC} values are in the range of a few nT/$\sqrt{\text{Hz}}$ for single NV centers.

Note that for the case of ensemble NV centers, the expressions for both η_{DC} and η_{AC} contain an additional factor $\sqrt{N}$ in the denominator, where N is the number of NV centers [18].

The T_2 values obtained from the simple Hahn or SE sequence discussed above can be further enhanced to reach actual T_2 by making use of multipulse sequences known as dynamical decoupling (DD) protocols [116, 117, 119, 124]. These pulse sequences are unique to AC sensing as they are intrinsically insensitive to DC fields. Basically they are an extension of the SE sequence with more than one π pulse added so that the T_2 time and accordingly the η_{AC} could be improved. This is discussed in the following section 1.5.3.

1.5.3 Dynamical decoupling

Multipulse sequences were initially developed for studies in NMR for refocussing the ensemble of spins [125]. Recently they have been extensively utilized for dynamicaly decoupling the various solid state systems including the NV sensors from the environment [9, 28, 126]. Basically they contain a series of n number of π pulses equally separated by

τ. Most commonly used DD sequences are based on family of Carr-Purcell-Meiboom-Gill (CPMG) pulse sequences [127, 128]. As mentioned earlier, NV center's coherence is strongly reduced due to its interaction with the surrounding bath of nuclear spins. In a typical CPMG-n sequence, the NV spin is periodically flipped so as to cancel the effect of its environment, which increases the T_2 [119]. The sequence can be regarded as a high pass filter because it cancels out all the noise frequencies which are smaller than the frequency of the pulse spacing [118].

If the interpulse delay τ is swept, the sequence decouples the NV spin from every other frequency except for a set of frequencies given by $f_L = \frac{k}{2\tau}$, where k=1,3,5,...is the resonance order [92]. For this specific set of frequencies the decoupling fails resulting in recoupling. The NV spin then acts as a narrow band filter with a bandwidth (full width at half maximum) $\Delta f = \frac{1}{n\tau}$ [9]. Therefore by increasing n, the filter can be made narrower to increase the frequency resolution. The resulting spectrum shows the presence of NV coherence (or 'Bright' state) for all the frequencies where the decoupling happened and a decoherence (or 'Dark' state) where the recoupling took place. Any k can be chosen to observe the peak, but k=1 gives the strong signal and accordingly most experiments are done with that value. The maximum and minimum f_L that can be sensed depends on the Rabi frequency (which determines the width of the π pulses) and T_2 time, respectively.

Generally, the phase Φ acquired during a pulse sequence containing n number of π pulses with a spacing τ is written as [9],

$$\Phi = \int_0^T \gamma_e B(t) g(t) dt \tag{1.14}$$

where, $T = n\tau$ is the total sequence time, $B(t)$ is the oscillating signal and $g(t)$ is the modulating function that changes sign whenever a π pulse is applied and takes values -1 and +1 (figure 1.16). The Φ acquired during a sequence depends on the relative phase difference between the $B(t)$ and modulation function $g(t)$. For a signal that is in phase with the $g(t)$ (or when the nodes of the signal coincide with the π pulse timing), maximum Φ occurs and for out of phase $B(t)$, minimum Φ occurs. Further, as the train of π pulses periodically invert the sign of the $B(t)$, we obtain a 'rectified' DC signal with fluctuating amplitude (figure 1.16). Since a DD sequence is nothing but a set of π pulses embedded inside a standard Ramsey sequence this rectified DC signal can now be measured [117].

The equation 1.14 in the frequency domain can be written as,

$$\Phi = \gamma_e T B_{AC} W(f_L, \phi_0) \tag{1.15}$$

where $W(f_L, \phi_0)$ is the filter function of the sequence. The form of $W(f_L, \phi_0)$ depends on the sequence. For CPMG sequence it is a sinc function [118],

$$W(f_L, \phi_0) = 8 \sin^2\left(\frac{\omega T}{2}\right) \frac{\sin^4\left(\frac{\omega T}{4n}\right)}{\cos^2\left(\frac{\omega T}{2n}\right)} \tag{1.16}$$

(where $\omega = 2\pi f_L$). The filter function allows only those frequencies which are centered around $f_L = f_k = \frac{k}{2\tau}$ (with k=1,3,5,...) with a filter bandwidth given by $\frac{1}{n\tau} = \frac{2f_L}{n}$, as mentioned above.

Spectral decomposition

The phase Φ given in equation 1.15 is converted into a measurable fluorescence signal. This coherence signal ($C(t)$) is convolved with a filter function, $W(\omega)$ of the DD sequence used. In order to reconstruct the spectrum of the spin noise (known as power spectral density, $S(\omega)$), the measured signal $C(t)$ needs to be deconvolved with the corresponding $W(\omega)$. Generally the $C(t)$ decays exponentially, $C(t) = e^{-\chi(t)}$, where the decoherence functional $\chi(t)$ is defined as [118, 124],

$$\chi(t) = \frac{1}{\pi} \int_0^\infty S(\omega) \frac{W(\omega)}{\omega^2} d\omega \tag{1.17}$$

by considering the filter function to be a Dirac δ-function localized at the given frequency (ω_0), the equation 1.17 is solved to $\chi(t) = tS(\omega_0)/\pi$. Hence, we can express the $S(\omega_0)$ in terms of $C(t)$ as,

$$S(\omega_0) = -\pi \ln(C(t))/t \tag{1.18}$$

This way, by measuring the $S(\omega)$ for various values of ω_0 the spectrum of spin noise of the NV's environment can be decomposed.

XY pulse sequence

In CPMG sequences the π pulses are applied along a single axis in the transverse plane (i.e., along X or Y axis). For higher order (large n) sequences, CPMG protocols are prone to pulse errors such as those caused due to imperfect MW duration, frequency and phases of the π pulses [116]. Since the π pulses are applied along only one axis (say X), errors in orthogonal axis (Y) are not compensated, and these errors accumulate over the sequence duration and lead to eventual deterioration of spin manipulation. To avoid this, a slightly modified set of pulse sequences have been employed and are robust against such pulse errors. These are known as XY sequences [116, 129, 130]. Here, instead of a single axis, the sequence is comprised of alternate π pulses which differ in phase by $\pi/2$, meaning that they are applied along X and Y axes alternatively. Except for this alternating phase factor, the XY sequence is identical to CPMG and has a similar filter function as the latter.

In a XY sequence, the phases of the π pulses are alternated judiciously so that the errors in both axis are self compensated. A typical XY sequence with a block of 8π pulses each separated by a pulse delay τ is drawn in figure 1.17a. The first four π pulses have alternate X and Y phases, and the next four have their phases swapped. This block of 8π pulses is repeated N times to get a total number of $8\times$N pulses and the whole set is embedded within a Ramsey sequence. As the XY sequence are known to be robust against pulse errors, they are most commonly used in the NV based magnetometry [31, 36, 131–133].

Figure 1.17b shows the results of XY based sensing of AC magnetic signals due to the bath of ^{13}C nuclear spins surrounding the NV center at a magnetic field of |B| $\sim$411 G. A XY8-4 (total 32 π pulses) sequence was applied to a NV in the bulk of the diamond. The τ was varied upto 5 μs and the corresponding fluorescence signal shows broad collapses and sharp dips. The ^{13}C bath produces an oscillating signal (Larmor precession) with a period $\tau_L = 1/f_L$ at the given |B| and this is sensed by the NV center [92]. The broad collapses correspond to the resonance order of this spin bath at specific k which appear at 1,3,5
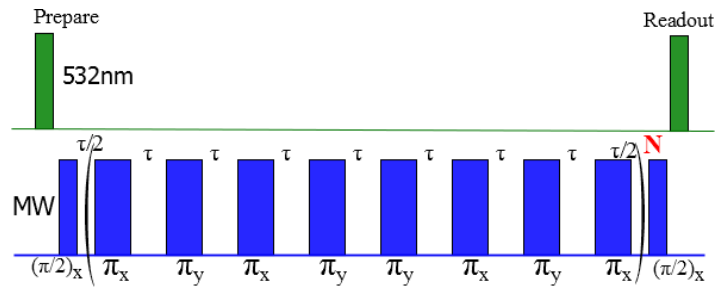
(a)
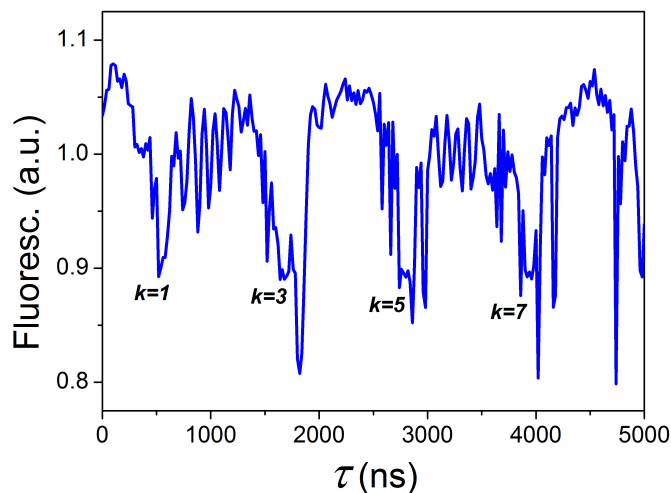
(b)

Figure 1.17: (a) Schematic of the XY8-N pulse sequence for detecting AC magnetic signals. (b) Typical XY8 results showing the signatures of carbons spin bath surrounding the NV center. Here, XY8-4 sequence was used and the |B| was 411 G.

and 7th positions of the fundamental (figure 1.17b) as described above. The sharp dips at higher τ are due to coherently coupled individual ^{13}C spins.

One disadvantage with the multipulse XY sequences is that they allow harmonics of the signal frequency to pass through the filter function [134]. For example, a fundamental frequency (f_L) can produce harmonics at $2f_L$, $4f_L$ and $8f_L$. This leads to ambiguities in the actual signal measurement. For the calculation of the filter function (e.g., equation 1.16) ideal π pulses with infinitely short duration are considered. But in real scenario the π pulses contain finite duration and causes the spin to acquire additional phase Φ. The harmonics are caused due to this extra spin evolution during the finite time of the real π pulses.

1.5.4   Probing nanoscopic volumes via statistical polarization

In conventional NMR experiments, the magnetic signal originates from a small number of thermally polarized nuclear spins. For a spin-1/2 system at thermal equilibrium, ratio of number of spins ($N_\uparrow$) aligned along the field to those ($N_\downarrow$) aligned anti-parallel to it follows the Boltzmann distribution [29],

$$\frac{N_\uparrow}{N_\downarrow} = e^{-\frac{\Delta E}{k_B T}} \approx 1 - \frac{\Delta E}{k_B T} \tag{1.19}$$

where, ΔE-is the magnetic energy separation between the two levels, k_B-Boltzmann constant and T-is the temperature. For small |B| and room temperature (which is relatively large), $\Delta E \ll k_B T$. An approximation of $e^{-x} \approx 1$-x for $x \ll 1$ is used in the above equation. Due to the small ΔE the two levels are equally populated, implying that $N_\uparrow = N/2$, where N is the total number of spins. The above equation then simplifies to,

$$N_\downarrow - N_\uparrow = \Delta N_T \approx \frac{N}{2}\frac{\Delta E}{k_B T} = \frac{N}{2}\frac{h\gamma_n|\text{B}|}{k_B T} \tag{1.20}$$

where, ΔN_T is the thermal polarization, h-Planck constant and γ_n is the nuclear gyromagnetic ratio. The fractional spin polarization $\Delta N_T/N$ is generally quite small and is of the order of 10^{-5}. As a result only a large ensemble of spins ($N > 10^{15}$) produce a detectable magnetic signal and in this regime only thermal or Boltzmann polarization is the dominant mechanism.

However, if we move towards smaller detection volumes containing sufficiently small number of spins another type of nuclear spin polarization mechanism known as the 'statistical polarization' becomes dominant [135, 136]. For a given number of N spins, the instantaneous polarization (ΔN_T) of the spins fluctuates over their characteristic time scale (T_1 time). In the limit of measurements times smaller than this time scale and small ΔN_T the ΔN_T appears static but its statistical variance σ_N is non-zero and equal to $\sqrt{N}$. This gives rise to statistical polarization $\Delta N_S = \sqrt{N}$ due to incomplete cancellation of the randomly oriented spins. The resulting signal is called spin noise signal. In case of conventional NMR experiments, due to large N involved the ΔN_S is negligible compared to ΔN_T. But, for ensembles containing small N (for N close to unity), the ΔN_S becomes a dominant mechanism and overtakes ΔN_T. For example, in a detection volume containing 10^4 spins $\sqrt{N}$ is $\sim 10^2$, which means the fractional polarization $\Delta N_S/N$ is $\sim 10^{-2}$, which is orders of magnitude larger than the $\Delta N_T/N$ ($\sim 10^{-5}$) in the same volume.

The size of the critical volume V at which the ΔN_S starts to dominate the ΔN_T (i.e., $\sqrt{N} > \Delta N_T$) depends on the sample number density ($\rho_N = N/V$) and the |B| used. Explicitly, ΔN_T occurs for volumes,

$$V < \frac{1}{\rho_N}\left(\frac{2k_B T}{h\gamma_n|\text{B}|}\right)^2 \tag{1.21}$$

For water samples ($\rho_N \approx 7 \times 10^{28}\text{m}^{-3}$) at room temperature (300 K) and at fields, |B| = 400 G, the resulting critical volume turns out to be $V = 769$ $(\mu\text{m})^3$.

In the presence of an external field with magnitude |B|, the statistically polarized spins precess with a Larmor frequency given by $f_L = \gamma_n|\text{B}|$. The amplitude and phase of the magnetic field produced by this precession varies in time because the statistical polarization shows fluctuations. However, its frequency remains centered around the f_L described by a Lorentzian and allows for measurements via suitable experimental techniques [28].

The detection of statistical polarization has been realized by many experimental approaches including the magnetic resonance microscopy (MRFM) for the detection of small number of electron and nuclear spins [136, 137].

Nanoscale NMR with NV centers

Even though MRFM has sensitivity down to single spin level, the requirements of low temperature and high vacuum in this method may not be feasible for samples which require ambient conditions, for example biological systems. NV centers, due to their atomic size and relatively long T_2-time even at room temperatures enable both AC and DC with nanoscale spatial resolution. Indeed, over the last decade intense work has been directed towards realizing NV centers as alternative probes for MRFM [4, 138].

In order to achieve both maximum sensitivity and spatial resolution, it is necessary to have the NV centers in close proximity with the target spins. This is because of two reasons: One, magnetic dipolar coupling of NV spin with the nearby target spins scales as $1/r^3$, where r is the separation distance. Consequently, only r in the nanometer range can provide sufficient coupling strengths. Second, for imaging applications the spatial resolution is determined by the precise and minimum r, thus necessitating a close proximity of the sensor-target spins. Although earlier demonstrations with NV centers showed the detection of individual electron and nuclear spins within the diamond, for nano-NMR applications it is necessary to sense spins outside the diamond surface. Clearly, NV centers at μm depths or below the diamond surface are not viable for such applications.

NV centers in nanodiamond (ND) offer the required proximity with the target spins but the progress in ND is hampered by relatively low T_2 times, often insufficient for high sensitivity applications. Therefore, one is left with the option of positioning NV centers close to the surface in bulk diamond. This can be currently achieved via well established NV fabrication methods such as ion implantation and nitrogen delta doping. With these methods it is now possible to position single NV centers at depths as small as a few nm below the surface [21, 122] and with sub nanometer accuracy. Currently, NV centers implanted at a few nm depth below the surface are probes of choice for several applications of external spin sensing. Besides the close proximity, the T_2 time is a crucial figure of merit for sensing applications as it determines the achievable spectral resolution and sensitivity. In bulk NV centers T_2 depends on the concentration of nuclear spins and paramagnetic centers within the crystal. The upper limit is set by spin-lattice relaxation time as $T_2 \leq 0.5 T_1$. For the case of shallow NVs however, additional sources of noise from the surface contribute to degrading the T_2 times. The surface induced noise originates from several mechanisms specific to surface [100, 124, 139]. Major factors are due to both electric and magnetic field noises, with the former dominating the latter at low frequency regimes [140]. While the electric field noise are due to surface charges such as unpaired electron spins [140, 141], the magnetic field noise possibly comes from the fluctuating magnetic fields created by the surface states in the top most carbon layers [123]. Consequently the coherence time decays on a faster time scale ($T_2 \leq 0.1 T_1$) than in case of bulk NV.

Further, well behaved and stable NV centers are essential for magnetometry applications. An important issue with the shallow NVs is the stochastic charge state switching (between negative and neutral states) due to strong interaction with the surface charges. As the switching from NV^- to NV^0 results in the drop in fluorescence (due to the different emission band, see figure 1.3), the optical properties are degraded and results in the poor signal contrast, which is undesired. It is shown that oxygen terminated diamond surface stabilizes the charge state (i.e., NV^-) as a result of negligible free surface charges. On the

(a)

(b)

(c)
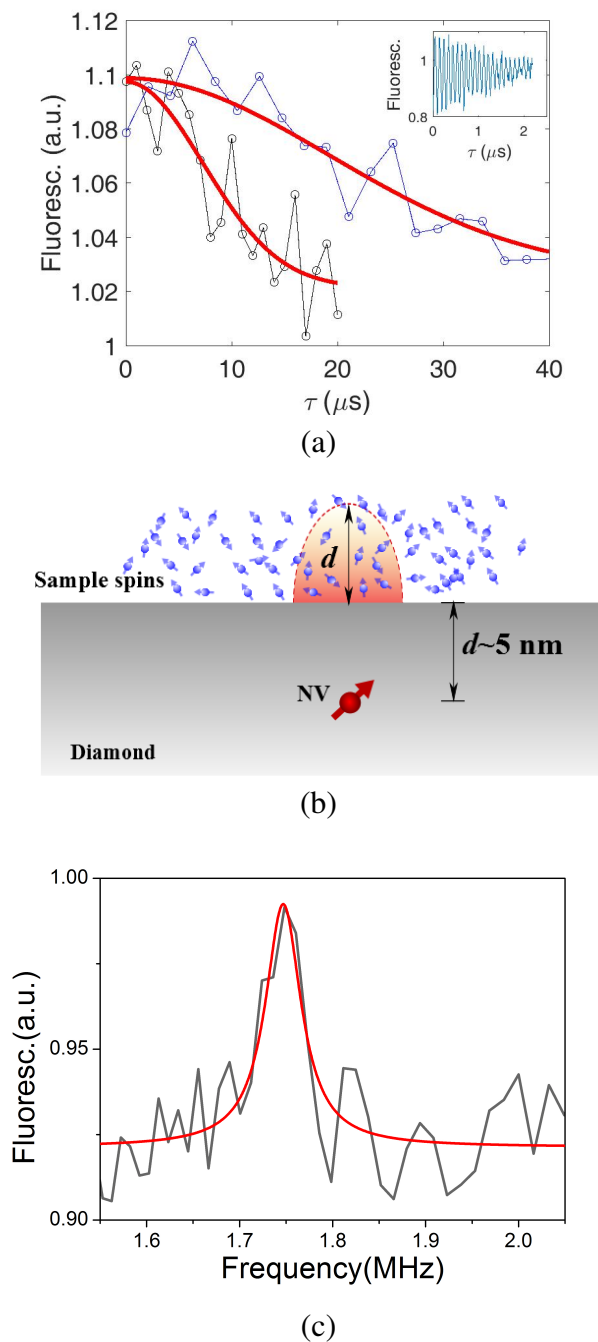
Figure 1.18: (a) T_2 measurements on a shallow NV center using simple Hahn sequence (black line with circles) giving 10.3 ± 2 μs and XY8 sequence (blue line with circles) giving 27 ± 5 μs. Red curves are results from fit to stretched exponential fuction $e^{-\left(\frac{\tau}{T_2}\right)^2}$. Inset shows the $T_2^* \approx 1$ μs measured from Ramsey sequence on the same NV. (b) Schematic of external spin sensing with shallow NV center. NV sensing volume extends upto a half sphere (orange shaded region) of diameter d equal to its depth inside diamond. (c) Typical XY spectrum obtained from shallow NV showing the protons peak at the Larmor frequency (f_L). The proton signal originates from the thin layer of H_2O adsorbed on the diamond surface. Here, |B| =412 G is used; values of f_L= 1.75 MHz and a FWHM = 47 ± 10 kHz are obtained from fitting to a Lorentzian function.

other hand, hydrogen termination leads to accumulation of charges and consequently turns the charge state to be neutral (NV^0) [139].

Figure 1.18a shows the typical coherence measurements from a shallow NV located at a few nm below the surface. Results from simple Hahn sequence gives T_2=10 μs, which is about an order of magnitude enhancement compared to $T_2^* \sim 1$ μs from the same NV. But the actual T_2 of ~ 30 μs was obtained when a multipulse XY8 sequence was used. As it is evident from the measurement, ultimate T_2 values in shallow NV centers are about two orders of magnitude lower than the T_2 values of bulk NV centers (in diamond with $1.1\%^{13}C$) which are in the range of several hundred μs.

These T_2 values (of tens of μs) of shallow NV are still sufficient to observe the signatures from sample spins outside the diamond surface [30, 31]. As the detection length scale of NV is in the nanometer range, we can readily observe statistically polarized spins in nanoscopic volumes, just similar to MRFM. This offers following advantages compared to MRFM and conventional NMR: first, this enables performing nano-NMR spectroscopic studies on samples at ambient conditions; second, it eliminates the need for having high magnetic fields to create thermal polarization and requires no sample spins driving. Also the sample volumes reduce from about 10^{-9} liter in bulk NMR to about 10^{-22} liter in nano-NMR [39, 142]. It is estimated that about a few hundred statistically polarized spins could be detected with this method [30, 31].

Figure 1.18b is an example of such a measurement scheme involving a shallow NV center at a depth (d) for sensing sample spins. The sample can be directly placed on the diamond surface. It is known from the previous studies [31] that a NV center at a depth of d could sense spins within a sensing volume of a half sphere of diameter d above the diamond. A nano-NMR spectrum of proton spins in the water layer on top of the diamond surface at a magnetic field of ~ 410 G is shown in the figure 1.18c). The experiment employed a XY8-N dynamical decoupling pulse sequence for detecting the magnetic field from the protons spins within a volume of about $(5 \text{ nm})^3$ corresponding to the half sphere. As mentioned in the section 1.5.3, the DD sequence accomplishes two tasks: first, it extends the coherence time to a true T_2-limit; second, by tuning the filter function to a desired frequency, the NV spin can be made insensitive to every other fluctuating (noise) sources except for desired Larmor frequency (here, f_L of protons).

However, the typical spectral resolution (FWHM or Γ_p) of several tens of kHz (e.g., ~ 50 kHz in figure 1.18c) offered by standard DD protocols is at least three orders of magnitude small compared to Γ_p achievable with the conventional NMR spectroscopy.

Initial demonstration of nano-NMR (by ref. [30, 31]) of external spins using NVs has inspired several groups to employ shallow NVs for various interesting studies in condensed matter physics. For example, they have been used for studying spins in two dimensional thin films of hexagonal boron nitride [38] and water [39], for studies of graphene [40], ferromagnetic materials [42], thin metal films [41], and meteorite chondrules [143]. Simultaneously, the detection sensitivity close to the level of single molecule and even single spin exterior to the diamond surface has been demonstrated. For example, detection and spectroscopy of individual protein molecules [34, 35], multiple nuclear species [133], and individual nuclear and electron spins [36, 37] have been reported.

Apart from NMR spectroscopy, achieving a magnetic resonance imaging (MRI) at the level of single molecule is also a long standing goal. Towards obtaining a three dimensional

(3D) nano-MRI of nuclear spins, shallow NV centers have been utilized in some of the recent works [131, 132]. In the early demonstrations, NV center (either in the ND [4] or grafted to a diamond nanopilllar [144] was used to scan across a sample. But in the recent studies the sample containing target spins is attached to a scanning probe and scanned across the shallow NV center in a bulk diamond. While the sensitivity is improved due to increased T_2 compared to that of ND or nanopillar, the spatial resolution is only limited by the NV-target spin separation and the limitations of the scanning hardware. At the moment a spatial resolution of ~ 10 nm with chemical specificity (i.e., ^{1}H and ^{19}F nuclei) of the sample has been achieved [131, 132]. Possibly, the 3D imaging of nuclear spins from individual molecules is within reach, with application of large magnetic gradients [145].

Correlation spectroscopy

While the sensitivity is approaching the level of single spins, clearly Γ_p obtained from T_2 based DD protocols are insufficient to extract information about interactions at the molecular levels due to poor Γ_p. Several strategies to mitigate the intrinsic T_2 based methods have been explored over the years. Of these, utilizing the long lived T_1-time for sensing is one such attempt. As the T_1 is about an order of magnitude higher than T_2, performing measurements at the T_1 limit could correspondingly improve the Γ_p. This can be accomplished by performing correlation spectroscopy [39, 146]. Principle of correlation spectroscopy is depicted in the figure 1.19a. It consists of two blocks of XY8-N sequences with constant N and inter pulse delay τ. As in a standard DD method, the τ is matched to the resonance condition for Larmor frequency (f_L) of the nuclear species to be detected, $1/\tau = 2f_L$. The delay time known as the correlation interval (τ^*) between the two blocks is varied. Essentially, the NV spin gathers a phase (Φ_1) in the first XY8-N block and is converted to population difference using a final $\pi/2$ pulse, but is not readout optically. As a result, the NV spin retains information about the Φ_1 as long as T_1 (of NV) persists. The nuclear spins are allowed to evolve during the τ^* time. In the second block another phase Φ_2 is picked up and converted to population difference. If the nuclear evolution during the τ^* was slow enough then the two phases Φ_1 and Φ_2 are said to be correlated and readout using the last laser pulse. The resulting correlation signal,

$$S_c(\tau, \tau^*) \sim \langle \sin \Phi_1 \sin \Phi_2 \rangle$$

(where $\langle \rangle$ denotes time average) decays on a time scale of T_1 of NV center and allows for relatively longer interrogation times than T_2 of NV. Correspondingly, the Γ_p improves as $\sim 1/T_1$ (instead of $1/(n\tau) \approx 1/T_2$ in a simple DD protocol) and the dynamics of the nuclear spins over longer times could be observed. As the T_1 in shallow NV centers decay on $\sim$ms time scale, Γ_p of few kHz, about an order of improvement could be achieved.

Figure 1.19b shows the results from a correlation experiment to sense the external proton spins using shallow NV centers. The amplitude of S_c as a function of τ^* due to proton spins on the surface of diamond is plotted. The τ^* was varied upto 100 μs and the corresponding S_c did not show considerable decay. Fourier transform of S_c gives a peak at the proton Larmor (f_L) and its FWHM gives the corresponding linewidth, Γ_p. A value of $\Gamma_p = 10$ kHz ($\sim 1/\tau^*$) was obtained (figure 1.19c). On the other hand a usual T_2 based XY8-25 measurement with $n\tau \sim 50$ μs yielded a proton signal of $\Gamma_p = 24$

46

(a)

(b)

(c)
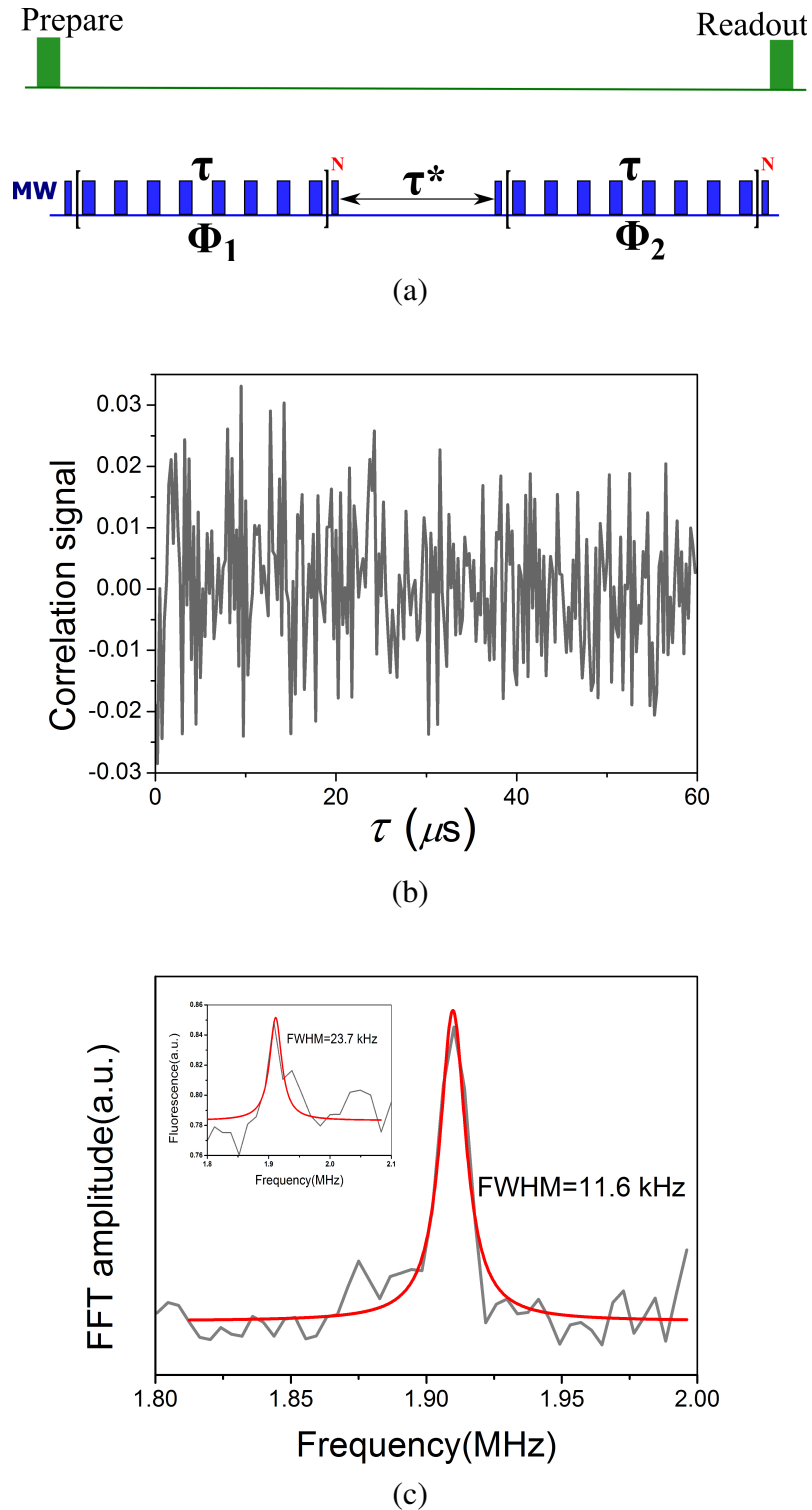
Figure 1.19: (a) Schematic of the XY based correlation sequence for sensing the external spins. τ and N were fixed while τ^* was varied. (b) Amplitude of the correlation signal due to proton spins on the diamond surface. N = 25 (or total of 200 π pulses) in each block was used. Here the signal upto 60 μs out of total measurement time (100μs) is shown. (c) Corresponding Fourier transform of the signal showing a peak at the Larmor frequency (f_L) = 1.91 MHz with a FWHM of 11.6±1 kHz. As a comparison, the inset shows results from XY8-25 experiment on the same NV yielding FWHM~24 kHz. The data were fit to Lorentzian functions.

47
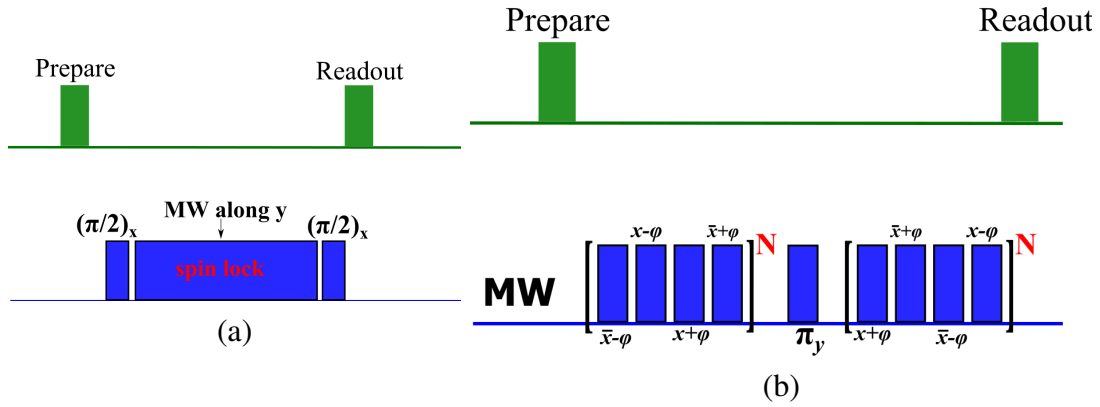
Figure 1.20: Continuous decoupling sequences. (a) Spin locking sequence. (b) DYSCO pulse sequence. π pulses with corresponding phase angles are indicated. There exists no delay time between any π pulses.

kHz (figure 1.19c inset) for the same NV. Evidently, the correlation method significantly improves the spectral resolution but it is still not sufficient to match the resolution obtained from conventional NMR methods, which are in the range of Hz.

1.5.5 Continuous dynamical decoupling

Spin locking

The free precession based or phase detection methods discussed so far provide a sensitive way to detect AC signals whose frequencies are upto MHz. For detection of signals with even higher frequencies (hundreds of MHz), which are relevant for detecting nuclear spins at higher magnetic fields, the NV center's bandwidth has to be extended beyond MHz. Further, as mentioned in the section 1.5.3 phase detection based methods are prone to spurious harmonic artefacts which complicate the measured signal interpretation. Continuous driving of the NV spin can address these problems. It offers the advantages of- fast driving of the NV spin enables sensing broadband noise signals extending to high frequency range ($\gg$1 MHz), avoiding the harmonics as it does not rely on phase detection, and prolonged interrogation time approaching the T_1 time allows for better frequency resolution. An example of a continuous driving for detection of signals is known as spin locking (SL) method [147, 148]. In a basic SL method (the pulse protocol is sketched in the figure 1.20a), a laser pulse first prepares the NV spin. Then a resonant MW $(\pi/2)_x$ pulse rotates the spin into its coherent superposition state. The spin is maintained there (i.e., τ=0) with a continuous resonant MW driving field applied along y direction (90° phase shift). When the NV Rabi frequency $\Omega_R = \gamma_e B_1$ (where, B_1 is the MW amplitude) matches with the weak RF magnetic field (Ω_{RF}) from a nuclear spin then NV spin undergoes coherent evolution between its parallel and anti-parallel states. The rate of this transition depends on the amplitude of the RF field. With a second $\pi/2$ pulse and a following laser pulse, this spin evolution can be observed as modulations in NV fluorescence. Thus, by adjusting the MW power the NV Rabi frequency can be precisely tuned to detect the external high frequency fields.

The total measurement time of SL decays on a time scale known as spin relaxation in rotating frame or $T_{1\rho}$ time. The value of $T_{1\rho}$ is such that, $T_2 < T_{1\rho} < T_1$.

Dynamical sensitivity control (DYSCO) method

Another example of CDD is Dynamical sensitivity control (DYSCO) method [149]. DYSCO is based on polarimetric methods and is used to perform NV sensing in the frequency domain (in contrast to DD baseds method which are interferrometric methods and sense in time domain). Here, the NV spin is continuously driven between its spin states (m_s=0 and m_s=-1) and the external oscillating fields are sensed by measuring the changes in spin state population. The DYSCO sequence (figure 1.20b) is composed of two $4 \cdot \pi$ pulse units with a π pulse in the middle such that:

$$\left(\pi_{\bar{x}-\phi}, \pi_{x-\phi}, \pi_{x+\phi}, \pi_{\bar{x}+\phi}\right)^{\mathrm{N}} - \pi_y - \left(\pi_{x+\phi}, \pi_{\bar{x}+\phi}, \pi_{\bar{x}-\phi}, \pi_{x-\phi}\right)^{\mathrm{N}} \qquad (1.22)$$

where the coherent MW π pulses with phase angle ϕ, drive the NV spin between its spin states m_s=0 and m_s=-1, and N is the number of $4.\pi$ pulse units. In the first $4.\pi$ unit, the first and last pair of π pulses have parallel and anti-parallel driving axes within them. In the second $4.\pi$ unit, just the pairs of π pulses of first unit are swapped. A π_y pulse between these two symmetrized $4.\pi$ units is used to compensate for pulse imperfections. The population, P_0 of the NV spin state at the end of the DYSCO sequence depends on the magnitude B_{RF} of the external radio frequency magnetic field, if any and the control phase ϕ of the pulse sequence.

As the population P_0 oscillates sinusoidally as a function of B_{RF} and ϕ, the Fourier transform (FT) of $P_0(\phi, B_{RF})$ is denoted as the dynamical sensitivity,

$$\beta(\phi) = FT[P_0(\phi, B_{RF})].$$

The term 'dynamical sensitivity' signifies that the quantity β can be varied from 0 (minimum sensitivity) to 1(maximum sensitivity) dynamically just by changing the phase angle ϕ between $-\pi$ and π.

For sensing the presence of spin noise signals in the NV surrounding, the β of NV is modulated to match the frequency f_L of the signal in a smooth and piece-wise manner. The dynamical sensitivity of a Nth $4.\pi$-pulse unit, is written as

$$\beta(f_L, t_N) = \beta_1 \cdot \sin(2\pi f_L t_N), \qquad (1.23)$$

where $t_N = (4N + \frac{1}{2}) \cdot \frac{2\pi}{\Omega_R}$ with Ω_R being the NV Rabi frequency and the amplitude factor β_1 can be increased in any arbitrary steps from 0 to 1. For a given N, the $\beta(\phi)$ of the NV sensor is modulated continuously over a range of frequencies (f_L) to be sensed and at each f_L the maximum of the sensitivity β_1 is varied from 0 to 1. Only when the modulating frequency of the dynamic sensitivity $\beta(\phi)$ matches the frequency f_L of the external signal (B_{RF}) to be probed, the NV spin response is observed in terms of change in its population (P_0). Thus, the information about the external B_{RF} is directly encoded in the population change in the NV spin levels. The frequency resolution of DYSCO is determined by the inverse of t_N. And, its detection bandwidth spans frequency range from minimum $\frac{1}{T_{DYSCO}}$ to a maximum of $\frac{\Omega_R}{9\pi}$. T_{DYSCO} is the NV relaxation in the DYSCO sequence, almost equivalent to spin relaxation in the rotating frame ($T_{1\rho}$). Therefore, the DYSCO bandwidth is bound by T_{DYSCO} and NV rabi frequency.

Figure 1.21 shows some results from DYSCO method. In figure 1.21a, a comparision of relaxation measurements for a shallow NV is given. The usual coherence time measured
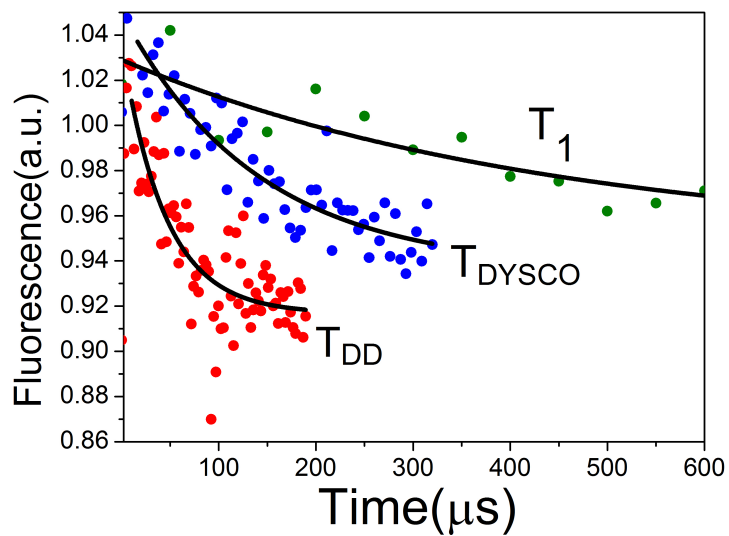
(a)
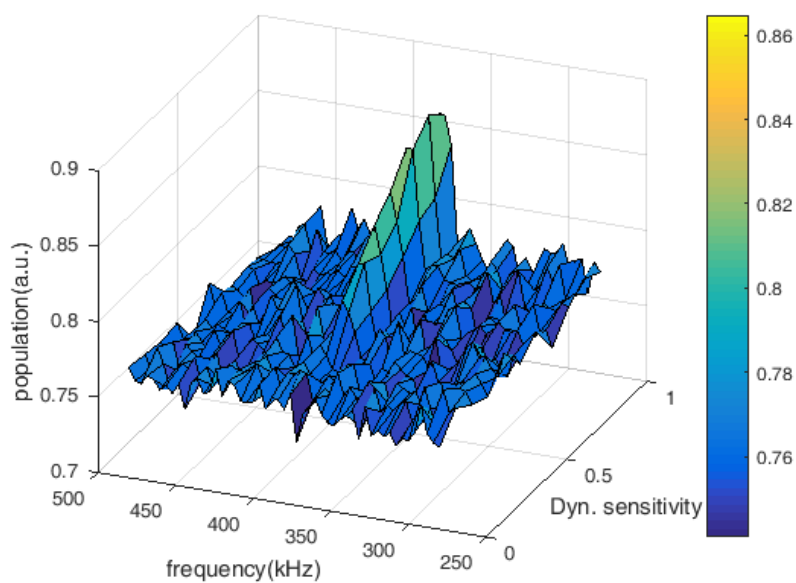
(b)

Figure 1.21: (a) Comparison of relaxation time measurements ($T_{DD} \approx 45\ \mu$s, $T_{DYSCO} \approx 140\ \mu$s and $T_1 \approx 444\ \mu$s) on shallow NV center. Longer T_{DYSCO} compared to T_{DD} allows for better spectral resolution in DYSCO. Dots are data points and black curves are exponential fits of measured data. (b) Sensing carbon spin bath using a bulk NV center. At a field |B| of 356.4 G, Carbon signal appears at its Larmor (382 kHz). Colorbar indicates the NV spin population.

from a dynamical decoupling method (XY) gives a limit of $T_2 \approx 45\mu$s. On the other hand, the relaxation time measured from DYSCO gives a substantially longer $T_{DYSCO} \approx 140\ \mu$s. The T_{DYSCO} was determined by setting the β=0 and recording the NV fluorescence while the total interrogation time t_N was varied by changing the N of DYSCO units. The upper limit is set by NV center's T_1 relaxation time (here, $T_1 \approx 444\ \mu$s).

Figure 1.21b shows the result of DYSCO method for sensing AC magnetic signals from ^{13}C spin bath using a bulk NV center. The DYSCO frequency (in kHz) modulation was performed around the Carbon Larmor and each frequency the dynamical sensitivity was ramped from 0 to 1. Here, the total time t_N was set to 100 μs and hence a frequency resolution of 10 kHz could be obtained.

This way, the DYSCO method achieves the sensing in frequency domain and since it does not involve free precession intervals the method is free from harmonic artefacts. Further, unlike in DD protocols the DYSCO method does not require the external AC signals to be phase matched or synchronous with its pulse sequence. As a result, it does not require prior knowledge of the signals to be sensed and works for all arbitrary signals within its detection bandwidth. Although DYSCO method is demonstrated on NV centers, in principle it can be applied to a wide range of other quantum sensors for precision metrology purposes.

A comparision of field sensitivity of DYSCO method (η_{DYSCO}) with that (η_{DD}) of typical DD sequence turns out to be, $\frac{\eta_{DYSCO}}{\eta_{DD}} = \frac{2}{\pi} \approx 0.64$.

Current state-of-the-art NV sensing protocols

Recently there have been reports of mitigating the limitation in Γ_p by employing entirely different strategies. Unlike the above mentioned protocols which rely on either NV's phase coherence (DD) or T_1 time (correlation, Spin-lock, and DYSCO), here the Γ_p is limited by long quantum memory time of nuclear spin [142] and the stability of the external reference clock [150, 151]. The achieved Γ_p is on par with the resolution in conventional NMR methods. These experiments have paved the way for advancing the NV based nano-NMR and metrology to a new level.

In the first strategy [142], the NV center is used as a sensor while it's intrinsic ^{15}N nuclear spin is used as quantum memory. Specifically, by entangling NV spin with the ^{15}N spin, a much longer spin relaxation time ($T_1 \approx 260$ s at =3T) of the ^{15}N spin could be utilized to carry out the standard NMR protocols on the sample independent of the short T_1 of the NV sensor. This method provides an achievable Γ_p of $\sim$mHz, which is on par with that of today's high resolution bulk NMR, while still being able to sense nanoscopic volumes. However, it should be noted that in nanoscopic volumes other non-trivial effects such as fast diffusion of sample spins in and out of NV sensing area contribute to broadening of spectral lines by orders of magnitude. Another issue with this strategy is the worsening of sensitivity with the Γ_p due to longer measurement time during which the NV center remains idle.

The second strategy is known as the quantum heterodyne (Qdyne) detection in which an arbitrary Γ_p along with highest sensitivity has been demonstrated [150, 151]. The method involves a continuous sampling of the external oscillating signal by repeatedly measuring the spin state of the NV center with reference to an external synchronization clock. The Γ_p is independent of T_1 of NV, and solely depends on the stability of the clock

and the total time (T) of the measurement. For a T of about one hour, Γ_p below 1 mHz for a shallow NV center, which is around 6 orders of magnitude improvement compared to $1/T_1$ limit (kHz) of the NV, is achieved [150].

By implementing the second strategy but with an ensemble of NV spins instead of single NV, it is proposed that Qdyne method could be readily used for nano-NMR for observing subtle molecular signatures (e.g.,chemical shifts and J-coupling) in small molecules [152]. The advantages of using ensemble are essentially two-fold: One, as the magnetic field sensitivity (η) scales as $1/\sqrt{N}$, where N is the number of NV spins used for measurement, a value of $\eta \sim$30 pT/$\sqrt{\text{Hz}}$ can be achieved. Hence the method puts in place the best experimentally achievable η of NV for sensing the external spins. Secondly, since the ensemble sensors sense much larger volumes (10^{-12} liter compared to 10^{-22} liter with single NV), thermal polarization dominates the statistical polarization and provides much stronger signals. Consequently, effects of spectral broadening resulting from diffusion in nanoscopic sensing volumes are mitigated due to increased size of volumes. Although the spatial resolution is limited to μm scale in NV ensemble system, the achieved spectral resolution of the order of Hz promises a bright prospect of NV based molecular NMR spectroscopy, potentially at the single cell level.

1.6   Chapter conclusion

NV centers in NV diamond have witnessed a rapid progress in research over the past one decade due to convenient room temperature operation, optical read out, atomic size and superior spin properties. For utilizing their full potential as nanoscale sensors for static magnetic fields, a major roadblock has been the intrinsically low spin dephasing time. Towards achieving static field sensitivity levels that are comparable or even better than the sensitivities for alternating fields, new methodologies have been constantly explored. In the next chapter (Chapter Two) a novel approach has been explored and demonstrated to enhance the static field sensitivity of individual NV centers beyond that achievable with usual Ramsey based methods.

As the NV centers continue to emerge as promising new candidates for studying various phenomena in condensed matter physics and beyond, it is intuitive to take up some grand challenges and study unexplored systems. Soft condensed matter offers a plethora of such challenges and there is always a constant need for highly sensitive and non-invasive experimental techniques to address some fundamental problems in that area. In this regard, Chapter Three attempts to extend the capability of individual NV centers to probe a well known soft matter system around the ambient temperature.

Chapter 2

A NV spin based hybrid magnetometer for static fields

2.1 Introduction

Magnetic sensors have played a key role in the advancement of modern science and technology over the past decades. They are vital for applications ranging from various engineering branches to fundamental scientific research [23, 153–156]. Ever increasing need for highly sensitive, robust and easy to use magnetic sensors has resulted in the development of various magnetometers based on both classical and quantum physics concepts. The magnetic sensors can be broadly classified into three categories based on their sensitivities [23, 157]: Magnetometers with high sensitivity, medium sensitivity and low sensitivity. Table 2.1 mentions this classification with the examples of the magnetometers with their typical sensitivities.

Even though superconducting quantum interference devices (SQUIDs) possess superior field sensitivity (sub fT), they require low temperature operation, thus limiting their use in a wide range of applications. Currently among the various magnetic sensors, there exists a trade-off between the sensitivity and other non-trivial factors such as operation at ambient conditions, frequency response, probe dimension, and power consumption [158]. In addition, whether the magnetometers are vector type (providing magnitude of the field with its vector components) or scalar type (only total magnitude of the field) is also important. For certain applications in the nanoscale, it is also important to have a sensor which can be miniaturized down to that scale as the probe-to-target distances often determine the strength of their interactions, thus allowing us to extract maximum information from such systems.

Sensitivity	typical field sensitivity	examples	probe dimension
High	$\sim 10^{-15}$ to 10^{-12} T	SQUID, atom vapor	10-20 mm
Medium	10^{-9} to 10^{-6} T	Induction, fluxgate	10-20 mm
	10^{-12} to 10^{-2} T	**GMI**	1-2 mm
Low	10^{-4}T and above	GMR and Hall-effect based	10-100 μm

Table 2.1: Different magnetometers and their sensitivities

Along these lines, electronic spins in solid state systems, particularly the Nitrogen-Vacancy (NV) centers in diamond have emerged as interesting systems with field sensitivity of a few nanotesla (nT) and nanoscale spatial resolution under ambient conditions. The NV centers are highly stable atomic scale defects in the diamond, and have shown to exhibit longest spin coherence times, T_2 among solid state systems at room temperature. This key advantage of the long coherence times is utilized in achieving nT-field sensitivities for the detection of oscillating AC magnetic fields. However, in several areas such as condensed matter physics or biomagnetism, it is of primary interest to sense the static (DC) or low frequency fields than AC or high frequency fields. In the standard method for measuring the DC fields by well known Ramsey method, the NV center's DC field sensitivity, $\eta_{\mathrm{DC}} \propto \frac{1}{\sqrt{T_2^*}}$ is limited by the spin dephasing time (T_2^*). In natural abundance ^{13}C diamond samples the T_2^* values are in range of 2 to 5 μs offering DC field sensitivities $\sim 18\ \mu$T to $\sim 7\ \mu$T when single NV centers are used as the measuring probe. This value of T_2^* is far shorter than the actual spin coherence time, T_2 by about three orders of magnitude. Clearly, by performing the DC field sensing at the limit of intrinsic coherence time (T_2) one could enhance η_{DC} by $\sqrt{\frac{T_2^*}{T_2}}$. In the literature, the magnetometry experiments at the T_2-limit performed by Echo based quantum lock-in protocols have enabled sensitive detection of AC fields down to nT/$\sqrt{\mathrm{Hz}}$. But such protocols are inherently insensitive to the slow varying or DC fields. Another possibility to enhance the sensitivity is to use the ensemble NV centers. But this fundamentally forces one to compromise one of the fundamental advantages of the single NV center-i.e., their nanoscale spatial resolution. Thus, realizing a high resolution (with single NV centers) with high sensitivity still remains as an open question.

In this Chapter, a novel approach which utilizes the advantages of the NV center's substantially longer T_2 time to achieve η_{DC} below 100 nT is presented. In this context, a micro-magnetic wire to enhance the sensitivity of near surface NV sensor to detect the weak external DC magnetic fields has been utilized. The wire exhibits a property known as the Giant magneto-impedance, which is exploited to enhance the η_{DC}. The magnetic wire, when positioned close to a single NV centre, acts both as a microwave antenna and a medium for near-field magnetic interactions with the NV center. The η_{DC} value obtained by this method is atleast two orders of magnitude better than that (~ 10 μT) obtained by conventional Ramsey magnetometry method. This hybrid magnetometer, which brings together the advantages of sensitive magnetic microwire and atomic scale defects in diamond matrix could potentially be employed in nanoscale field measurements with enhanced sensitivity.

2.2   Giant Magneto-Impedance

Recently, discovery of a certain magnetic phenomenon known as Giant Magneto-Impedance (GMI) has drawn the attention of researchers working in the development of magnetic field sensors [26]. The concept of magnetoimpedance (MI) where a change in the static magnetic field causes change in total electrical impedance (Z) of the ferromagnetic alloys was known since 1930s [159]. But due to the relatively weak change in Z associated with the MI effect, there was not much research interest in this area. But only after the
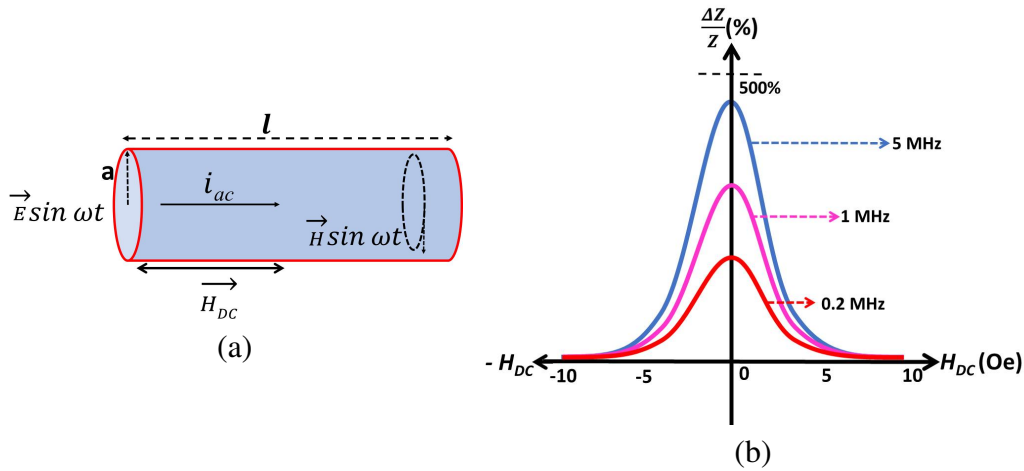
Figure 2.1: (a) A schematic illustration of the GMI wire carrying the alternating current i_{ac} and subjected to static field, H_{DC}. (b) Frequency-magnetic field response of the GMI ratio $\Delta Z/Z$. Large change in the $\Delta Z/Z$ for small changes in the H_{DC} of a few Oe and its dependence on frequency of i_{ac} can be seen.

discovery of unusual Giant magneto-impedance [24, 25, 160] in the 1990s, it has triggered intense investigations in that area. GMI is a high frequency analogue of well known giant magnetoresistance (GMR), which is the large change in the electrical resistance (R) of a material upon change in the external magnetic field. In both cases (GMI and GMR) one observes a large change in the voltage across the material when the magnetic field is applied. However, GMI and GMR are entirely different concepts in that GMI is purely a classical phenomenon [161–163] whereas the GMR effect has quantum mechanical origins. The interest in GMI is spurred by several advantages over the conventional magnetic sensors, namely the high sensitivity (<nT) and room temperature operation. Also in case of GMI sensors the maximum change in Z can be as high as 500%/Oe whereas in GMR sensors the change in R is usually ~1-2%/Oe. The η_{DC} comparison of GMR and GMI sensors can be seen from the table 2.1.

Definition

Giant magnetoimpedance is defined as a phenomenon in which under the application of a small alternating current (i_{ac}), the AC complex impedance (Z) of a soft ferromagnetic conductor suffers large change when a tiny static external magnetic field (H_{DC}) is applied. In figure 2.1a, a cylindrical GMI wire under the application of i_{ac} and H_{DC} is schematically shown. In terms of the relative change $\frac{\Delta Z}{Z}$ of the impedance the GMI ratio is defined as,

$$\frac{\Delta Z}{Z}(\%) = \frac{Z(H) - Z(H_{ref})}{Z(H_{ref})} \times 100, \tag{2.1}$$

where, $Z(H)$ is the impedance of the material at a given value of applied static magnetic field H and $Z(H_{ref})$ is the saturation (reference) value of the impedance at which the external magnetic field no longer changes the impedance. For conventional amorphous magnetic microwires (discussed below), $Z(H_{ref})$ is on the order of 100 Oe. Figure 2.1b illustrates the relative change $\frac{\Delta Z}{Z}$, known as the GMI response which has a
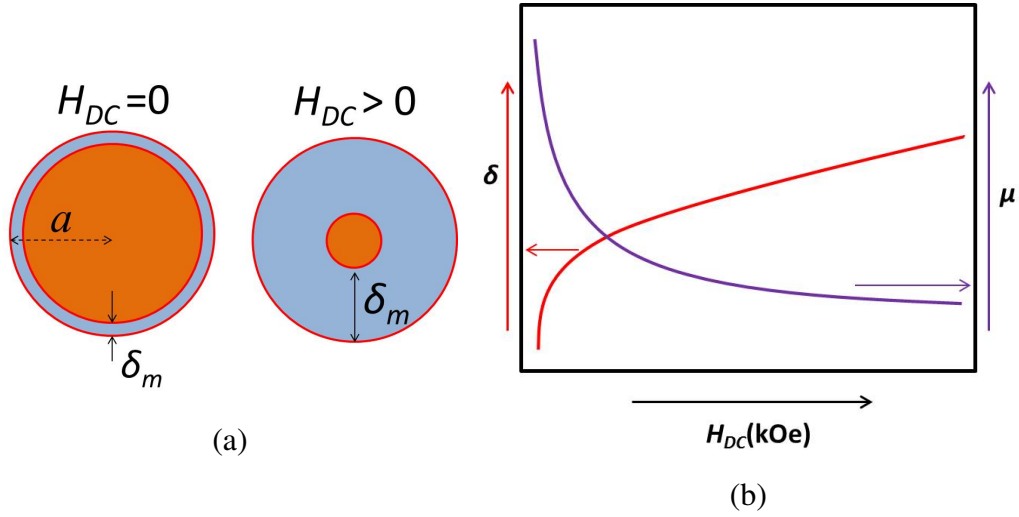
Figure 2.2: (a) A schematic of variation of skin depth (δ_m) with magnitude (H_{DC}) of external field, as seen from the cross section of a cylindrical magnetic wire of radius, a. (b) Variation of δ and total permeability as a function of H_{DC}.

strong dependence on the frequency of i_{ac} and H_{DC}. This is explained in detail in the sections 2.2.1 and 2.2.2.

Since in general $Z = R + jX$ is a complex quantity with R and X are respectively the AC resistance and reactance, it is important to note that R and X also undergo corresponding changes and contribute to overall change in Z,

$$\frac{\Delta R}{R}(\%) = \frac{R(H) - R(H_{ref})}{R(H_{ref})} \times 100,$$

and

$$\frac{\Delta X}{X}(\%) = \frac{X(H) - X(H_{ref})}{X(H_{ref})} \times 100$$

The GMI effect was first observed in amorphous ferromagnetic FeCoSiB cylindrical wires with small magnetic fields and at relatively low frequency [25, 164]. Later on, albeit smaller effect, this phenomenon was also observed in amorphous soft ferromagnetic thin films [165] and ribbons [166].

2.2.1 Origin and basic theoretical concepts

The concept of magneto-impedance (MI) has its origin in the well known *Skin effect* in electromagnetism [167]. The alternating radio frequency (RF) current $i_{ac} = i_0 e^{j\omega t}$ in a conductive element such as a metal wire, tends to be distributed near the surface (skin) of the conductor (figure 2.2a). This means the current density is not homogeneous over the cross section of the conductor but largest near the surface and decreases exponentially away from the surface (figure 2.2b). The *skin depth* (δ_m), the region below the outer surface of the conductor where the effective current flows is given by,

$$\delta_m = \sqrt{\frac{2\rho}{\omega\mu}} \qquad (2.2)$$

56

where, ρ is resistivity of the material, ω, the angular frequency of the alternating current, and $\mu_t = \mu_r \mu_o$ (where, μ_r and μ_0 being the relative permeability and permeability of free space, respectively) is the total permeability. From the above equation we can expect that as the ω increases, δ decreases which means that the i_{ac} tends to be concentrated near the surface of the conductor. For ordinary nonferromagnetic conductors such as copper μ_t is independent of the ω and the external magnetic field. But for ferromagnetic materials, μ_t strongly depends on ω, amplitude (I_0) of the AC driving current as well as the direction and magnitude of the external applied magnetic field (figure 2.2b). In soft ferromagnetic materials (materials which can be easily magnetized or demagnetized), the permeability μ_t changes by orders of magnitude even for the application of small external magnetic fields. The permeability μ_t is also sensitive to temperature, mechanical strain, and magnetic anisotropies in the material [168, 169].

2.2.2 GMI frequency dependence

Depending on the range of frequency ω of the driving current i_{ac}, the magnetoimpedance in general can be broadly classified into three categories [170]:
(i) Low frequency regime (DC to a few kHz),
(ii) Intermediate frequency also called as GMI regime (from ~ 100 kHz to a few MHz), and
(iii) High frequency or ferromagnetic resonance (FMR) regime (from ~ 10 MHz to GHz). In the literature theoretical treatment of the MI effect involves both the uniform cylindrical magnetic conductors (wires) as well as the planar magnetic films (ribbons), as these are the most commonly used material shapes. But as this work only deals with the magnetic wires we will consider the details regarding the wires alone.

2.2.2.1 Low frequency regime

Consider a cylindrical homogeneous ferromagnetic wire of radius a and length l. As one experimentally measures the voltage drop between the ends of the wire, the value of Z can be indirectly obtained by knowing the total voltage drop (V_T). In the low frequency range, when a time varying current i_{ac} flows through the wire, it produces a circular AC magnetic field around the wire. The total voltage drop $V_T = V_R + V_L$ produced is the sum of resistive voltage (V_R) and inductive voltage (V_L). The inductive voltage can be written as [161, 171]

$$V_L = E_z(a).l = -\left(\frac{j\omega}{c^2}\right) L_i.i_{ac}$$

where $E_z(a)$ is the longitudinal electric field generated due to circular time varying magnetic field, $L_i = \mu_\phi l/2$ is the internal inductance and μ_ϕ is the circular permeability of the wire, c is the speed of light in vacuum, and $j = \sqrt{-1}$ is imaginary number. The expression for the total V_T now becomes,

$$V_T = RI - \left(\frac{j\omega}{c^2}\right) L_i.i_{ac}$$

where R is the resistance of the wire. If we define the impedance (Z) as $Z = V_T/i_{ac}$ then the expression follows as,

$$Z = R - \left(\frac{j\omega}{c^2}\right) L_i$$

$$Z = R - \left(\frac{j\omega}{c^2}\right) \frac{\mu_\phi l}{2} \tag{2.3}$$

when a small external DC magnetic field is applied, it modifies the circular permeability μ_ϕ of the wire. Since the inductance L_i is proportional to the μ_ϕ, the main contribution to the change in the voltage drop across the sample is thus due to the inductive term. So, at relatively low frequencies, the impedance (Z) depends on the inductive term (equation 2.3) and hence it is also called as a magneto-inductive effect. In this regime the *skin effect* is very weak.

2.2.2.2 Intermediate frequency regime

This is also known as the GMI regime where the *skin effect* plays a major role in causing the changes in impedance of the material in response to an external magnetic field.

Consider a uniform magnetic conducting wire with radius a, length l, and cross sectional area A. Under the linear approximation the impedance of the wire is a complex number $Z = Z_1 + jZ_2 = \frac{V_0}{i_0}$, where i_0 and V_0 are the amplitudes of the alternating current through the wire and total voltage drop between the ends of the wire, respectively. The Z can also be written in terms of the current density as [162],

$$Z = \frac{V_0}{i_0} = \frac{lE_z(a)}{A\langle j_z\rangle_A}$$

or

$$Z = R\frac{j_z(a)}{\langle j_z\rangle_A} \tag{2.4}$$

where, R is the DC resistance, E_z and j_z are the longitudinal (z) components of the electric field and current density respectively, and $\langle\cdot\rangle_A$ is the average over the cross sectional area A. As can be seen from equation 2.4, Z/R is the ratio of current density at the surface to its average value.

The current density $j_z(a)$ can be obtained by solving the Maxwell equations [167]. The original Maxwell equations are:

$$\nabla.\mathbf{B} = 0$$

$$\nabla \times \mathbf{E} = -\frac{\partial \mathbf{B}}{\partial t}$$

and

$$\nabla \times \mathbf{H} = \mathbf{J} + \frac{\partial D'}{\partial t}.$$

(the notations have their usual meaning)

By using the material relations $\mathbf{J} = \mathbf{E}/\rho$ and $\mathbf{B} = \mu_0(\mathbf{H} + \mathbf{M})$ (where ρ is the resistivity and $\mathbf{M}$, the magnetization), and neglecting the displacement current term (i.e., $\frac{\partial D'}{\partial t} = 0$) for the ferromagnetic conductor the simplified Maxwell equations can then be written as [172],

$$\nabla.(\mathbf{H+M}) = 0 \tag{2.5}$$

$$\nabla \times \mathbf{J} = -\frac{\mu_0}{\rho}\frac{\partial(\mathbf{H+M})}{\partial t} \tag{2.6}$$

$$\nabla \times \mathbf{H} = \mathbf{J} \tag{2.7}$$

Now, by applying curl on both sides of equation 2.7, substituting it for $\nabla \times \mathbf{J}$ in equation 2.6, and finally by noting $\nabla.\mathbf{H}$ from equation 2.5 and rearranging the terms, one arrives at,

$$\nabla^2\mathbf{H} - \frac{\mu_0\dot{\mathbf{H}}}{\rho} = \frac{\mu_0\dot{\mathbf{M}}}{\rho} - \nabla(\nabla.\mathbf{M}) \tag{2.8}$$

By knowing $\mathbf{M}(a,t)$ and solving for $\mathbf{H}(a,t)$ in equation 2.8 with the approximation that relation between B and H is linear ($B = \mu H$), the equation 2.7 can be used to calculate the current density, j_z. Using the equation 2.4 the final expression for the impedance Z then becomes [25, 167],

$$\frac{Z}{R} = ka\frac{J_0(ka)}{2J_1(ka)} \tag{2.9}$$

where J_0 and J_1 are the Bessel functions of the first kind, a is the radius of the wire, and

$$k = \frac{(1+j)}{\delta_m}$$

with j being the imaginary number. δ_m is the classical skin depth or penetration depth of alternating current [25],

$$\delta_m = \frac{c}{\sqrt{4\pi^2 f_{ac}\sigma\mu_\phi}} \tag{2.10}$$

where c is the speed of light in vacuum, $f_{ac}(=\omega/2\pi)$ is frequency of current, σ and μ_ϕ are electrical conductivity and circular permeability of the material, respectively.

The equations 2.9 and 2.10 can be used to qualitatively explain the GMI effects in the ferromagnetic wire. Under an applied external magnetic field the circumferential permeability μ_ϕ reduces, which then increases the skin depth, δ_m and hence modifies the Z. To obtain large GMI effects it is essential to have magnetic materials with large μ_ϕ.

It is important to note that since $Z = Z_1 + jZ_2$ is a complex quantity, both the real (resistive, R) and imaginary (inductive, L) terms contribute to the total impedance Z and hence to GMI [164, 169]. Also, one must note that in ferromagnetic conductors, the $\mathbf{B}$ and $\mathbf{H}$ are not generally linear. So the equation 2.4 (and hence equation 2.9) is valid only for the small amplitudes of the AC driving current [168].

As a comparison, in ordinary metals like copper the *skin depth* does not depend on the permeability but on the frequency (f_{ac}) of the AC driving current. In case of soft

ferromagnetic materials the permeability (μ_t) is orders of magnitude higher than that of metals. Hence for such materials with similar conductivity as metals, the *skin effect* (see equation 2.2) appears at frequencies orders of magnitude smaller than those expected for metals.

To explain the GMI behaviour in magnetic materials in the intermediate frequency range (i.e.,below 100 MHz) several theoretical models have been proposed. Of these, eddy current and domain model satisfactorily explain the observed GMI effect in such materials [161, 173]. In case of cylindrical magnetic wires, periodic magnetic domains form a bamboo-like structure with domain walls between adjacent domains. The effective behaviour of the μ_ϕ with respect to the frequency of the AC current and external magnetic field depends on the contributions from the domain wall movement and the magnetization rotation from its equilibrium values in each domain. At relatively low frequencies like $<$ 500kHz, both domain wall movement and magnetization rotations contribute to the μ_ϕ. For higher frequencies, the domain wall movements are damped by the eddy currents in the material and the main contribution to μ_ϕ comes from the magnetization rotations. The *skin effect* becomes stronger in this range and at high frequencies the equation 2.9 becomes $Z \propto \sqrt{\omega.\mu_\phi}$.

The GMI response curve (such as the one schematically shown in the figure 2.1b) shows strong dependence on the magnetic anisotropy of the domains so that the shape of the curves show single or double peaks close to external field, $H_{DC} \approx 0$. The interpretation of the single peak or double peak behavior in the $\frac{\Delta Z}{Z}$ response has been explained in terms of the transversal anisotropic field H_k in the material [174]. For wires with sufficiently large perpendicular magnetic anisotropy (circular magnetic domains), when H_{DC} is increased along the longitudinal axis of the wire, the equilibrium magnetization in each domain rotates towards the axis. This increases the μ_ϕ and hence the Z. The impedance increases until it reaches a point where $H_{DC} \approx H_k$ [175, 176]. By further increasing the H_{DC}, μ_ϕ decreases, which in turn decreases the Z. Therefore, if the H_{DC} is varied from negative to positive value around 0, then $\frac{\Delta Z}{Z}$ response shows a double peak behaviour. On the other hand if the material has small H_k, the magnetization rotation dominates H_k at H_{DC} close to 0 itself and hence the Z displays a monotonous decrease from $H_{DC} = 0$. This results in the single peak behavior of $\frac{\Delta Z}{Z}$ (figure 2.1b)[177]

2.2.2.3 High frequency regime

At higher frequencies ($>$100 MHz), the magnetization rotations alone completely dominate the magnetization process and contributions of domain wall motion to the μ_ϕ can be neglected. It has been demonstrated that at such high frequencies, the GMI response of ferromagnetic materials is remarkably equivalent to ferromagnetic resonance (FMR) in metals [178, 179]. Thus all the solutions of the FMR in metals can be used to describe the GMI. The frquency response of the ferromagnetic metalic cylinders shows that the resistive (real) part, R of the impedance $Z = R + jX$ shows maximum and the inductive (inductive) part, X vanishes at the FMR frequency (f_r) [179, 180]:

$$f_r^2 = \left(\frac{\gamma_e \mu_0}{2\pi}\right)^2 H_{eff}(H_{eff} + M_s) \tag{2.11}$$

here, γ_e is electron gyromagnetic ratio, M_s is saturation magnetization and H_{eff}

is effective magnetic field (sum of H_{DC}, H_k and demagnetizing fields). At FMR, the theoretical skin depth reaches its minimum value ($\sim 0.1 \mu$m),

$$\delta_m = \sqrt{\frac{\alpha \rho}{\gamma_e \mu_0 M_s}}$$

and the GMI ratio ($\frac{\Delta Z}{Z}$), its maximum value. Here α is a damping constant. Note that this δ_m is frequency independent, and the corresponding theoretical $\frac{\Delta Z}{Z}$ is of the order of $\sim 10^3$ which is far greater than experimentally observed GMI. This is because the GMI is observed in intermediate frequency ($<$ 100 MHz) where the FMR conditions not are satisfied. Whereas in the high frequency range and at high currents the theoretical and experimental values match [181].

2.2.3 Fabrication techniques

The amorphous magnetic wires for the GMI applications can be fabricated by a number of rapid quenching or solidification techniques. Melt spinning, in-water quenching, glass coating processes, electrodeposition, and melt extraction technology are important methods to be named. Among these, the melt extraction technology is a preferred choice for fabrication of amorphous metal alloys [182–184]. In this method, a metal alloy with a required metal composition is first molten and made to come in contact with a high-speed rotating wheel which has a sharp edge. The thin molten layers off the edges of the wheel are quickly extracted and the microwires with diameters ranging from 20-50 μm are produced by rapidly quenching these layers. This method is known to offer following advantages over other production techniques: it has higher solidification rate ($10^5 - 10^6$ K/s). This helps to form amorphous phase, in addition to imparting better soft ferromagnetic and mechanical properties to the wires.

2.2.4 Material properties

2.2.4.1 Domain structures of wires

Formation of particular domain structure in each amorphous material results from the complex interplay [185, 186] of internal stresses generated during the rapid quenching process and what is known as *magnetostriction effect*, a property of magnetic materials to change their dimension when subjected to magnetic field. A material constant λ_s with its sign and magnitude defines the type of magnetostriction that exists in a material. For GMI applications, materials with small λ_s are required as the mechanical effects caused by magnetic field is low in this case. Due to the different quenching rates between inner and outer regions of the wire during the rapid quenching, domain structures with longitudinal, radial or circular magnetization directions are formed in the wire.

For amorphous magnetic wires with positive magnetostriction ($\lambda_s > 0$), the internal stresses during the rapid quenching induce a longitudinal magnetization in the core and a radial magnetization in the outer shell of the wire. Examples of this type include Fe-based wires [187]. On the other hand, for wires with negative magnetostriction ($\lambda_s < 0$), internal stresses during the quenching still yield a longitudinal magnetization in inner core but
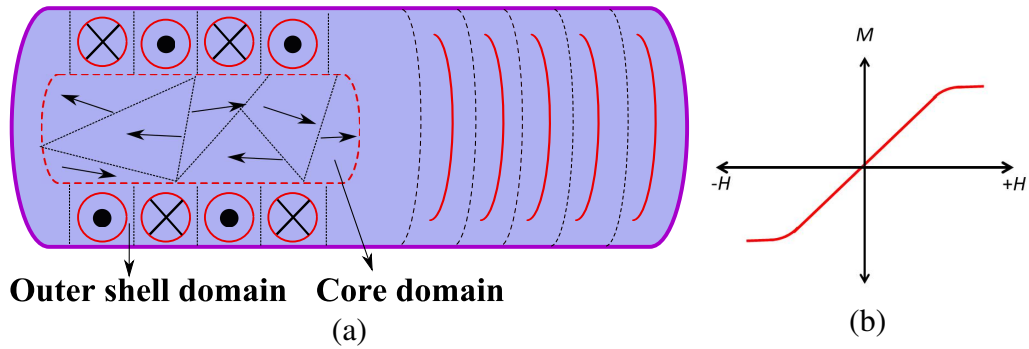
Figure 2.3: (a) Domain structure of negative magnetostriction amorphous wire. (b) Its typical hysteresis curve (schematic) showing linear magnetization (M) as a function of external field (H). A narrow hysteresis loop indicates negligible energy loss per cycle.

circular magnetization profiles in the outer shell (figure 2.3a). These are also known as 'bamboo' domain structures. Typically Co-based wires come under this category [186].

The positive magnetostrictive amorphous wires are not favourable for the GMI applications because of their radial magnetization in the outer shell domains. The radial domain structure does not result in the reorientation of the domains when an external field H_{DC} is applied, which will result in the low GMI effect. In contrast, in amorphous wires with negative and nearly vanishing λ_s, the magnetization and the anisotropy field H_k exist in circular direction in a plane perpendicular to the wire's longitudinal axis[1]. The H_{DC} acts to orient this transverse magnetization along its direction, thus decreasing the circular permeability, μ_ϕ. This results in the large GMI effect [188]. In general, materials with very small or zero λ_s are preferred because there is no energy loss involved due to magnetoelastic response (unlike materials with large $\pm\lambda_s$) when the H_{DC} is applied. This aspect boosts the magnetic softness of the material as the material can be easily magnetized or demagnetized. Another decisive advantage of having materials with vanishing λ_s is that they are robust against certain drawback known as 'magneto-impedance aftereffect'. Materials with 'magneto-impedance aftereffect' tend to show degraded GMI properties over time and hence are not desirable for the applications which require reproducible results [177].

2.2.4.2 Hysteresis behavior

One of the main criteria for a material to show GMI effect is its magnetic softness. Compared to hard magnetic materials, soft ferromagnetic materials, as a result of small coercive field (H_c), exhibit narrower hysteresis loop and the area enclosed within the loop is small. Hence the energy loss per magnetization cycle will be less. In addition, it is also necessary for the material to have a large saturation magnetization (M_s) as it enhances the interaction with the external magnetic field.

In materials with positive λ_s, due to the above mentioned magnetic structure of the domains, the hysteresis loop is relatively large in area and has rectangular shape. In the

---

[1]Typically, the H_k values are nearly four orders of magnitude smaller than the saturation magnetization in Co-rich amorphous wires.

materials with negative λ_s, as a result of easier re-orientation of the domains along the H_{DC}, the H_c is very small and the hysteresis loop is much narrower (figure 2.3b).

2.2.4.3 Permeability

The relative magnetic permeability (μ_r) of soft magnetic materials is an important parameter in determining the suitability of the materials for the GMI applications. In general materials with large μ_r are essential as they bring about large GMI effects upon the application of external H_{DC}. The amorphous wires with very small λ_s exhibit largest circular permeability (μ_ϕ) and hence are desired in applications, while wires with large positive or negative λ_s show smaller μ_ϕ.

Note that the equation 2.10 assumes μ_ϕ to have a real (static) value. But to understand its dependence on frequency (ω) and H_{DC}, a simple phenomenological model has been proposed by Beach *et al* [164]. Here, the μ_ϕ is given as a complex term $\mu_\phi(\omega, H_{dc}) = \mu_\phi' + j\mu_\phi''$ with,

$$\mu_\phi' = 1 + \frac{4\pi\chi_0(H_{dc})}{1+\omega^2\tau^2}; \quad \mu_\phi'' = \frac{4\pi\chi_0(H_{dc})\omega\tau}{1+\omega^2\tau^2}$$

Where, τ is relaxation time of the magnetization due to damped magnetic response of the domains, χ_0 is magnetic susceptibility at f=0. In the above equation for μ_ϕ, we see that permeability is a strong function of both H_{DC} and ω. At low frequencies, μ_ϕ varies rapidly with increasing H_{DC} while flatten out at higher ω. When ω increases, the μ_ϕ will decrease as the wire has less time to respond to H_{DC} and at GHz range the μ_ϕ approaches to unity.

2.2.4.4 Electrical properties

It is necessary to have amorphous materials with small resistivity as the smaller resistivity leads to large changes in the Z and hence the GMI effect (see Eq.2.9). In general amorphous materials with room temperature resistivity in the range 100 $\mu\Omega$.cm are chosen for the applications.

2.2.4.5 Effect of sample geometry

The geometrical dimensions like the length, radius play important role in the GMI effects. The reference [189] observed that in certain Fe-based (having vanishing λ_s) wires showed an increase in the GMI effect when the length (l) of the wires increased. On the contrary Phan et al [190], reported rather diminishing GMI effect if the length (l) is increased in case of Co-based wires.

There exists an optimal thickness or diameter for obtaining the maximum GMI effects in the wires [191]. It is observed that as the diameter of the wire increased the GMI peak shifts towards the lower frequencies [192]. Because, as the μ_ϕ varies strongly with ω at lower frequencies, the skin effect becomes stronger as the thickness of the wire increases.

2.2.5   Magnetic field sensitivity and ultimate noise limit

The noise floor of a magnetometer determines the lowest possible magnetic field that can be measured. In the case of GMI amorphous wire sensors, the intrinsic magnetic noise spectral density (β) given by [193, 194],

$$\beta = \sqrt{\frac{2\alpha k_B T}{\gamma_e M_s \pi a^2 l}} \tag{2.12}$$

The equation 2.12 defines the theoretically achievable noise floor for the GMI sensors. It has unit of T/$\sqrt{\text{Hz}}$. Here, α is dimensionless damping parameter, k_B is Boltzman constant, T is temperature, and rest of the symbols have been already defined above. Using the standard values for the parameters used in the relation, for Co-based microwire of nominal sizes $a \sim 30$ μm and $l \sim 10$ mm, one obtains $\beta \approx 10$ fT/$\sqrt{\text{Hz}}$ at room temperature (T). However to date, the experimentally reported values for the best noise level are often in the range of 1 pT/$\sqrt{\text{Hz}}$ to 100 pT/$\sqrt{\text{Hz}}$, atleast 2-4 orders of magnitude higher than the theoretical value. Many sources contributing to this limitation have been identified [195–197]. Fundamental limitation is set by the intrinsic magnetic noise associated with the thermal fluctuations of the magnetization of domains in the wire. Other important sources include noise in the electronic circuitry involving the alternating current generation, impedance measurement and any preamplifiers used in the setup, and also from the intrinsic Johnson noise from the GMI wire itself.

The typical noise spectral density of the GMI sensor has two regions in the frequency scale (not to confuse with the driving frequency ω of the alternating current). One is low frequency $1/f$-type noise (possibly due to intrinsic magnetic noise of sensor) upto ~ 1 kHz and the other is a white noise floor (electronic and other noise) for all frequencies above 1 kHz [194, 197] where the noise level becomes flat and stays constant. For GMI sensors the noise level could reach ~ 30 pT/$\sqrt{\text{Hz}}$ in the $1/f$ region and ~ 1 pT/$\sqrt{\text{Hz}}$ in the white noise bandwidth [195]. Hence any meaningful measurements of the external magnetic field are possible only above this noise level, which is currently of the order of a pT. If the sensitivity is made to increase further then the intrinsic magnetic noise will dominate all other other noise sources and decreases the stability of the sensor.

2.3   A Hybrid magnetometer based on NV center in diamond and GMI microwire

Main motivation for hybrid sensor

There are basically two methods by which the impedance of the GMI sensors are detected-one, standard four probe measurement (also known as diagonal impedance) method where the AC voltage across the wire is directly measured. Secondly, induction coil based measurement or two probe (known as off-diagonal) method where the voltages generated in the pick up coils are measured. Owing to advantages such as nearly a 2-fold improvement in field sensitivity and reduced noise levels [196, 198], the pick up coils method has been generally employed. This method relies on the pick coils made from hundreds of turns

of a thin wire to detect the small changes in the impedance of the wire. As a result, among other factors that limit the ultimate sensitivity of these sensors the efficiency of the inductive coupling between the sensor and the pick up coils also plays an important role. In addition, the millimeter scale GMI sensing element combined with similar sized pick up coils renders the overall dimension of measuring probe rather bulky. This limits our ability to miniaturize the overall sensor for applications in nanoscale.

On the other hand NV centers have emerged as potentially reliable "Quantum sensors" for various applications. Single NV centers have been demonstrated to be highly sensitive magnetic field sensors with AC sensitivity down to a few nT/$\sqrt{\text{Hz}}$ at ambient conditions with nanoscale spatial resolution [6, 11, 16]. The sensitivity could be further enhanced if one employs ensemble NV centes instead single ones. In that case the sensitivity scales as $\sqrt{N}$, where N is the number of NV centers used. With such ensemble NV-sensors (containing $N \sim 10^{11}$) an AC and DC field sensitivities of subpicotesla (0.9 pT/$\sqrt{\text{Hz}}$) [19] and 15 pT/$\sqrt{\text{Hz}}$ [18, 199] respectively, have been achieved. However, due to the low spatial resolution associated with the ensemble based sensors, they are not suitable for nanoscale applications. In case of single NV centers, owing to the atomic size of the defects the sensor to target distances could be as small as nanometers, thus allowing nanoscale spatial resolution while compromising the sensitivity. Currently, the AC and DC sensitivities achieved in case of single NV centers are in the range of a few nT/$\sqrt{\text{Hz}}$ and ~ 10 μT/$\sqrt{\text{Hz}}$, respectively.

Therefore, in this chapter, a hybrid sensor system consisting of GMI wire (classical) and the NV center (quantum) as a highly sensitive static magnetic field sensor at ambient conditions is demonstrated. The single NV center replaces the bulky pickup coils for readout of the GMI response to external fields and the overall sensitivity of the hybrid sensor is at least two orders of magnitude better than the standalone single NV sensor.

2.3.1   Materials and methods

For the studies mentioned here Co-rich amorphous GMI wires with a composition of $Co_{69.25}Fe_{4.25}Si_{13}B_{12.5}Nb_1$ fabricated by melt-extraction method are used. These wires are cylindrical in shape and known to exhibit soft ferromagnetic properties with nearly zero magnetostriction [200]. The wires with a diameter of ~ 30 μm and length ~ 30 mm were used for the experiments. Before positioning a wire near the NV centers, the fresh wire is first coated with a thin layer (a few microns) of Gold using a standard electroplating method. This coating of Au layer helped to stabilize the GMI behaviour of the wires by removing the fluctuations in its response in the frequency region of our interest and also resulting in the smooth magnetometry oscillations (described in the section 2.4.4). The resistance (R) of the wire was measured to be about 10 Ω (Or resistivity ≈ 40 $\mu\Omega$.cm). For a RF signal with a maximum applied amplitude of 1.0 V (peak-to-peak) corresponds to an alternating current (V/R) with an amplitude of ~ 100 mA.

The NV centers in the high purity (1.1% of ^{13}C concentration) CVD diamond (from *element6*) of dimensions 3 mm $\times$3 mm $\times$0.1 mm were produced by implantation of ^{15}N ions (with same procedure explained in the section 1.3.3). It is expected that these NV centers are about a few nm below the surface following the SRIM simulation results and reports in the literature which used similar ion implantation energies and annealing
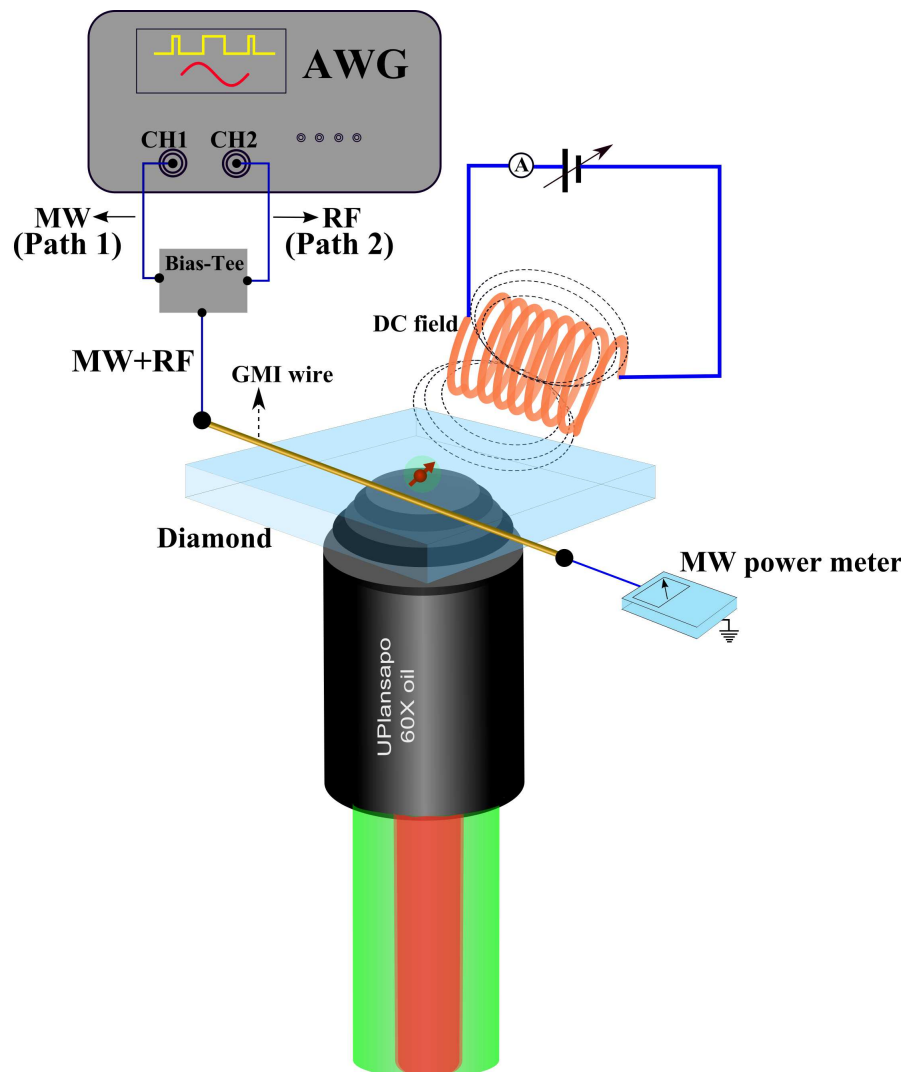
Figure 2.4: Simplified schematic of experimental setup for GMI-NV based sensing of external static magnetic fields. MW and RF signals generated from the two channels (CH1 and CH2) of the AWG are applied simultaneously to the GMI through a Bias-Tee. A nearby coil produces the DC magnetic field to be sensed. NV center is shown as red sphere with an arrow.

conditions. For the demonstration of GMI-NV hybrid sensor, one could also use native NV centers (in bulk) which will have even higher T_2 than that of shallow NVs. But there are two main reasons to employ shallow sensors here. First, they are large in number and are within a thin (nm) strip of top layer of diamond, which gives us freedom to explore many points along the length of the wire where the magnetic effects from the wire are enhanced and carry out sensitivity measurements. Second, as the shallow NV centers have been the favorite probes of choice for sensing fields from samples outside the diamond, it is interesting to see how much improvement in sensitivity one can achieve in case of standard diamond surface preparation.

Experiments were carried out on a home-built confocal microscope equipped with electron spin resonance setup for addressing the single NV centers as explained in the section 1.3. The two APDs used in the Hanbury Brown and Twiss anti bunching configuration to identify the single NV centers. A two channel arbitrary waveform generator (AWG70002A, Tektronix) operating at a sampling rate of 20 Gsps generates the optical pulses (via AOM), microwave (MW) pulses and the RF driving signals necessary for the pulse sequences used in the experiment. For simultaneous application of MW and RF pulses to the micro-wire a Bias-Tee Diplexer connector (200B-FF-3, MECA Electronics) is used. The microwave pulses generated in one channel of the AWG are amplified using a high power amplifier and applied to the RF port of Bias-Tee connector (Path 1 in the figure). The RF driving signal with a maximum amplitude of 1.0 V (peak-to-peak) for the GMI wire was generated at the second channel of the AWG and applied to DC or low frequency port of the Bias-Tee connector (Path 2). A single output port of the Bias-Tee was then applied to one end of the GMI wire. The GMI micro-wire was positioned right on top of the diamond which hosts shallow implanted NV centers at few nm below its surface. Two ends of GMI wire were soldered (or connected using conductive silver paste) to a PCB microwave stripline board. The other end of the wire was attenuated and terminated. This way one can simultaneously apply the MW and the RF signal to the GMI wire. We obtained a typical NV Rabi frequencies of $\sim$10 MHz (or π pulse length $\approx$50 ns) from the GMI wire.

The DC external magnetic field which needs to be measured with high sensitivity is produced by passing a known amount of direct current (DC) from a programmable current source (Keithley Model 6221) through a coil positioned near the micro-wire. The coil is made using a copper wire of $\sim$100 μm diameter and $\sim$100 number of turns with the coil diameter of about 7 mm. This coil was positioned close to the sample and its axis was kept parallel to the GMI wire such that the direction of the DC magnetic field lines emanating from the coil were approximately parallel to the length of the wire. This allowed us to take advantage of direction dependent response of the GMI wire to obtain maximum sensitivity for weak external DC fields.

2.4 Results and Discussion

In this section, first an optical and magnetic characterization of GMI wire using NV centers is presented. In the subsequent sections, a typical response of the GMI wire to external fields as observed from a single NV center, followed by a demonstration of sensitive DC magnetometry using the GMI-NV hybrid sensor is presented. Later on, dependence of the
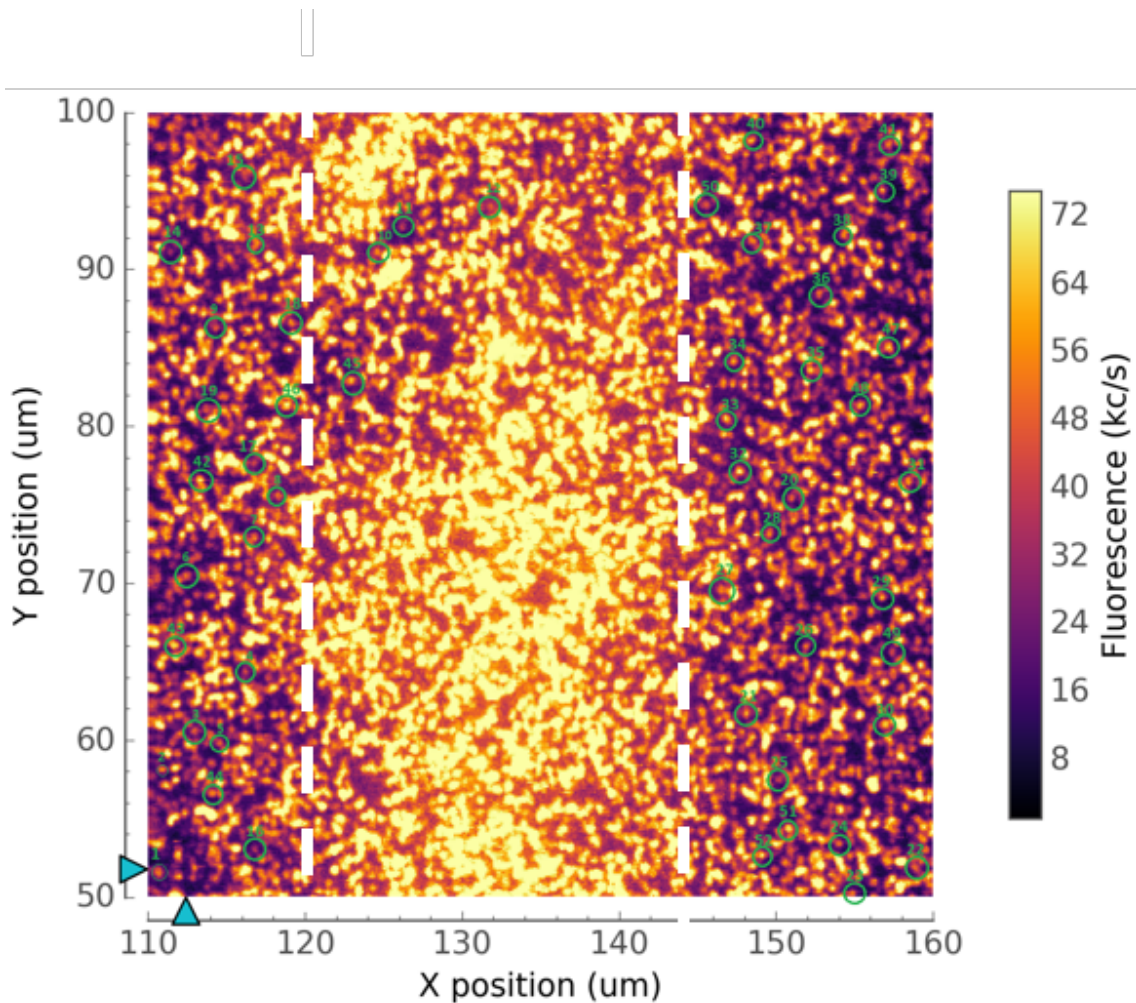
Figure 2.5: A confocal photo-luminescence scan (50 μm $\times$ 50 μm) of the shallow implanted NVs around the magnetic wire (indicated by white dashed lines). The magnetic field value at the individual NV center is calculated using the ODMR measurement. An ensemble of over 70 NV centers were used to reconstruct the magnetic field profile from the wire (see figure 2.6). Some individual NVs used for measurement are marked in green circles.

sensor response on different parameter is presented, and finally a discussion on tuning the sensor properties and possible improvements is mentioned.

2.4.1 Magneto-Optical studies of GMI wire using NV centers.

2.4.1.1 Magneto-Optical image

For the optical studies, an ensemble of over 70 NV centers are used, and a wide-field image of the magnetic profile of the wire is generated using the standard Zeeman relation.

Figure 2.5 shows a confocal image of shallow implanted NV centers in an area of 50 μm $\times$ 50 μm around the GMI wire (marked by white dotted lines). The GMI wire had a diameter of $\sim$ 25 μm, and due to the inherent magnetic nature of the wire its magnetic field extends to NV centers which are about 15-20 μm away along the lateral directions (i.e., X and Y-directions the confocal image). The GMI wire was used for both applying
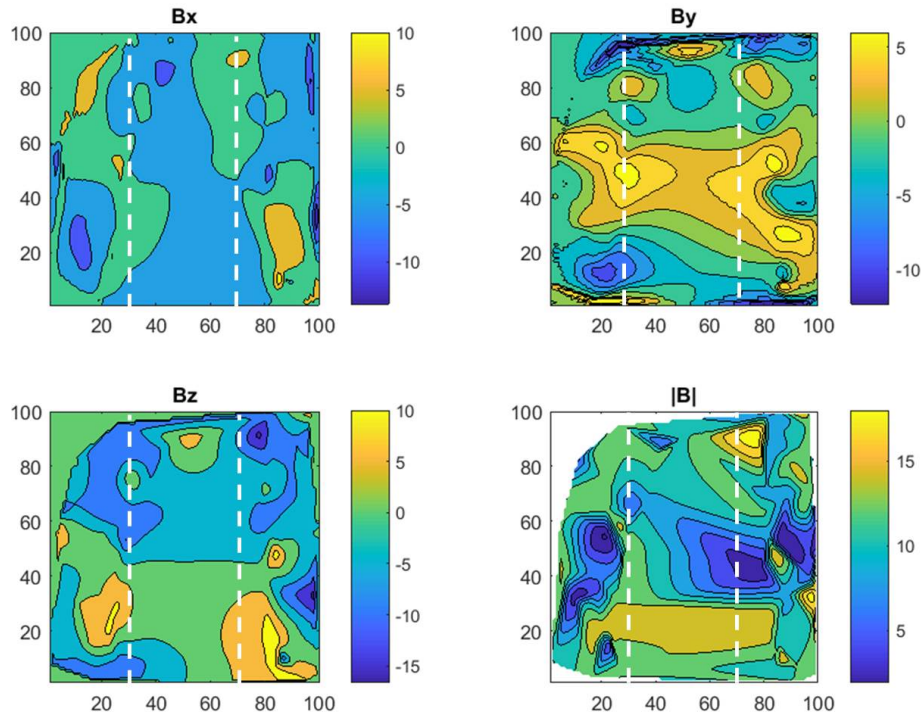
Figure 2.6: Calculation of the magnetic field profile of the wire using NV centers from the confocal image shown in figure 2.5. The components of the field, B_x, B_y and B_z along x, y and z directions respectively, together with absolute value of the field, |B| are plotted. The color bar indicates the field values in units of Gauss (G). Variation of the field values (as indicated by change in color from blue to yellow) can be attributed to the orientation of magnetic field lines from the different magnetic domains and domain walls in the amorphous GMI wire. The total area of 50 μm $\times$ 50 μm in figure 2.5 is divided into 100$\times$100 points for calculation. The approximate location of the wire is shown by white dotted lines.

.

microwaves (MW) for manipulation of NV spin and as an antenna for magnetic interactions with the NV centers. This interaction is possibly due to near-field effects as the wire is very close to the NV centers. Since the wire is magnetic, there exists a spontaneous magnetic field of several Gauss originating from the magnetic domains of the wire at the location of the NV centers. But this field has a spatial profile, in the sense from one point to another along the length of the wire its magnitude and direction change. Figure 2.6 is the wide-field magnetic image of the wire reconstructed using an ensemble of over 70 single NV centers in the given area in figure 2.5. The three components of the field along X, Y and Z directions along with the absolute value of the field ($|B|$) at the location of the NV is shown. The field value at the location of each NV was obtained by measuring the optically detected magnetic resonance (ODMR) transition frequency of that NV and then computed using the Zeeman relation $D_{gs} \pm \gamma_e.|B|$ where D_{gs} is the NV ground state zero field splitting and γ_e is the NV gyromagnetic ratio. As the field varies from the location of one NV to another one can see a distribution of the field values in the measured area. The variation in the field values as indicated by both gradual and abrupt changes in the color signifies the presence of different magnetic domains and domain walls in the amorphous GMI wire, their orientation, and their complex interplay.

Note that no driving alternating current was applied to the wire when these measurements were done.

2.4.2 DC magnetometry experiments

2.4.2.1 Combined GMI-NV sensing of external fields

Due to the spontaneous magnetic field from the ferromagnetic wire almost all shallow NVs in its vicinity show Zeeman splitting from D_{gs}. One can choose an NV which has symmetrically split ODMR transition lines about the D_{gs} and perform the spin manipulation experiments on the NV center as usual. Although the $|B|$ produced by the wire is < 10 G, this field is sufficient to drive the NV transitions with a reasonable Rabi frequency. Requirement of an additional high static field (hundreds of Gauss) to split the NV center D_{gs} is thus not necessary. Avoiding the usage of such a high field is also important because, presence of high field in a transverse direction to the wire's longitudinal axis would probably lead to pinning of the domains and hence reduced GMI response.

Figure 2.7 shows the ESR characterization of a shallow NV located at about a lateral distance of $\sim$5 μm from the wire. In figure 2.7a, ODMR spectrum on this NV is shown. Due to the presence of a stray magnetic field ($\sim$5 G) from the wire, NV center's m$_s = \pm 1$ degenerate spin sub levels are split from the zero field line D_{gs} = 2870 MHz (blue dotted vertical line). The presence of two dips at a separation of $\sim$ 3MHz on either side of D_{gs} indicates the HF interaction with unpolarized ^{15}N (nuclear spin I=1/2) of the NV center. For all NV spin manipulation experiments mentioned hereafter, MW frequency corresponding to m$_s = 0 \Leftrightarrow$ m$_s = -1$ transition is used. A standard Ramsey measurement using the sequence $(\frac{\pi}{2}) - \tau - (\frac{\pi}{2})$ gives a spin dephasing time, $T_2^* \approx 1.5$ μs (figure 2.7b). This value is typical for shallow implanted NV centers with the acid-cleaned diamond surface (see section 2.3.1). By employing a Hahn-Echo method, the NV spin interrogation time can be increased from intrinsic T_2^*-limit to a long lived T_2 time. Figure 2.7c shows the coherence time (T_2) measurement using a standard Hahn-Echo sequence of
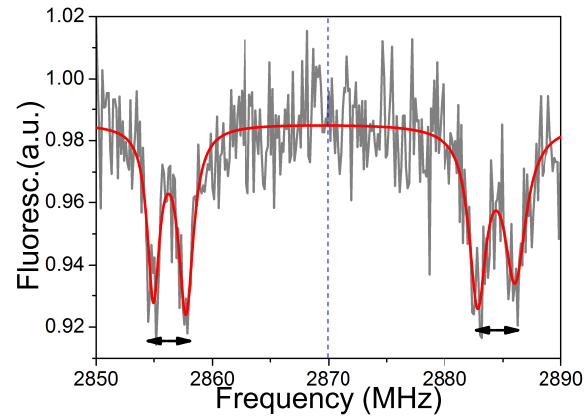
(a)
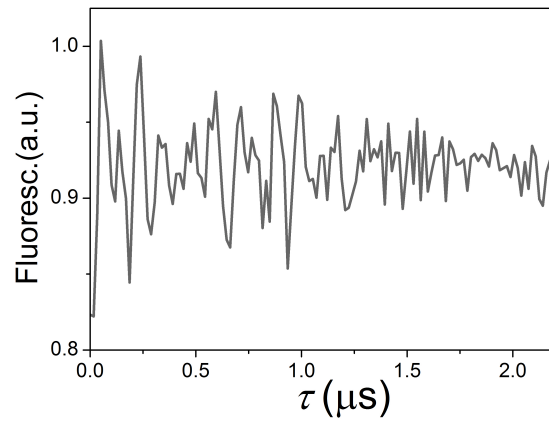
(b)
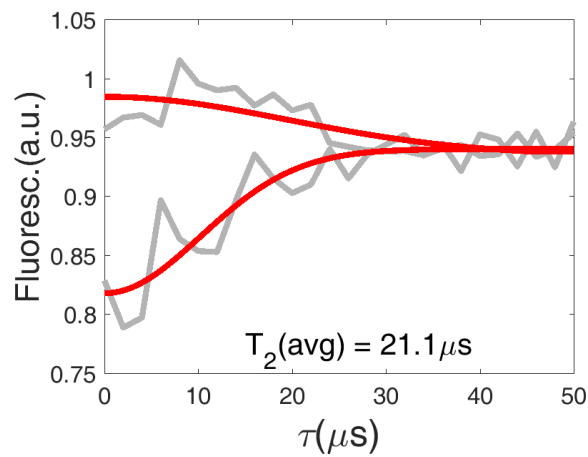
(c)

Figure 2.7: (a) ODMR spectrum of a single NV in the presence of stray magnetic field (of $\sim$5 G) from the wire. Grey line indicates the measured data and red line is a Lorentzian fit to the data. (b) T_2^* measurement yielding a value of $\sim$1.5 μs . (c) T_2 measurement. A T_2 (average) value of 21.1 μs was obtained. The two grey curves indicate the measurements with the phases of initial $\left(\frac{\pi}{2}\right)$ pulses differed by 180°. Red curves are the fit to the data (see the text).

71

$(\frac{\pi}{2}) - \tau/2 - (\pi) - \tau/2 - (\frac{\pi}{2})$. The data can be fitted to a standard stretched exponential function, $e^{-\left(\frac{\tau}{T_2}\right)^2}$ to extract the T_2 values. By changing the phase of the initial $(\frac{\pi}{2})$-pulses in the Echo sequence by 180°, one obtains two data curves (one starts from bright state and the other from dark state in figure 2.7c). The fitted T_2 values for the two curves are 14.5 ± 1.9 μs and 27.7 ± 8.9 μs, respectively for top and bottom curves. The decay rates of two curves differ, perhaps, due to MW-pulse imperfections in the Echo sequence. Therefore, an average value of 21.1 μs is considered as approximate T_2-value for the present NV. It should be noted that this T_2 value of $\approx$20 μs, is at least an order of magnitude more than T_2^* measured by Ramsey method ($\approx 1.5\mu s$).

As a first demonstration of NV-GMI coupling in the intermediate frequency regime (see section 2.2.2), GMI response to external static field is observed using NV based magnetometry method (figure 2.8).

The basic schematic of the GMI-NV magnetometry is depicted in the figure 2.8a. First a green laser pulse initializes the NV center into $m_s = 0$ spin sub level of its ground state triplet. For the NV spin manipulation, a MW frequency corresponding to transition between $m_s = 0$ and one of its other ground state sub levels (here $m_s = -1$) is used. A Hahn-Echo sequence $(\frac{\pi}{2}) - \tau - (\pi) - \tau - (\frac{\pi}{2})$ with a fixed total free-precession time (2τ) is applied to the NV center. A RF driving signal $V_{rf}(t) = V_{pp} \sin(2\pi f_{ac} t + \phi')$, with amplitude V_{pp}, frequency f_{ac} and phase ϕ' is applied to the GMI wire simultaneously. It is crucial that the f_{ac} is synchronous with the Hahn sequence duration, $f_{ac} = 1/(2\tau)$ and is phase matched (i.e., ϕ'=0) so that the phase acquired by the NV center in the Echo sequence is maximized.

Note here that the current (i_{ac}) through the wire is expressed directly in terms of the control voltage ($V_{rf}(t)$) applied from the AWG for the sake of simplicity.

To know the effect of external static field on the GMI-NV sensor, it is necessary to have prior knowledge of the approximate field which is produced from the coil. A straight forward way to estimate the B_{DC} is to perform standard FID experiment with a certain detuning from the NV resonance frequency. If the direct current (I_{DC}) through the coil is increased, the corresponding detuning frequency also increases linearly. In figure 2.8b, changes in the detuning frequency (obtained by performing FFT of FID signal) for a given NV as a function of current through the coil is plotted. In this given current range, a linear relation between detuning and current is observed. The calibration value (in units of T/mA) is obtained by dividing the slope of the resulting straight line by NV center's γ_e (28 GHz/T). The obtained slope of ~2 μT/mA is used to estimate the B_{DC} from the coil for the results shown in figure 2.8c. Note that the value of B_{DC} experienced by a given NV depends on its location in the confocal image.

Returning to schematic in figure 2.8a, under the application of a RF driving frequency (f_{ac}), presence of any weak external DC magnetic field (B_{DC}) along the length of the GMI wire causes modifications of its circular permeability (μ_ϕ) and hence changes its impedance, Z. Due to near field-type magnetic interaction of the wire with NV, this change in Z gets encoded as a change in the final spin state of the NV. The spin state of the NV is subsequently read out by another green laser pulse at the end of the sequence. If the amplitude (V_{pp}) of the signal is slowly ramped from zero to a finite value, the NV Hahn signal shows oscillations as in the case of a typical Echo-based AC magnetometry. The oscillations in the Echo signal arise due to sensitivity of the NV's Echo sequence to

(a)

(b)

(c)

(d)
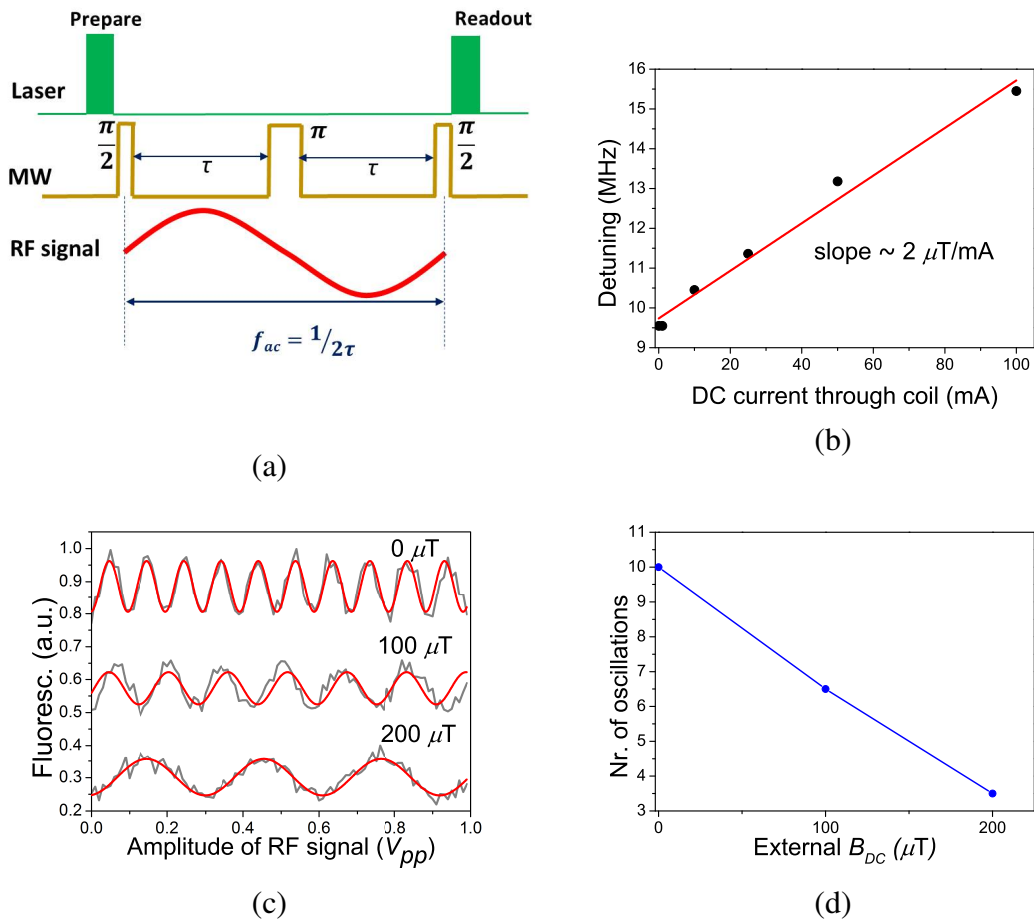
Figure 2.8: Hahn magnetometry with GMI-NV sensor. (a) Schematic representation of the Hahn Echo magnetometry sequence and synchronous RF driving of the GMI wire. (b) Variation of NV resonance frequency as a function of coil current. Black circles are data points and red line is a fit to straight line. (c) NV-Hahn magnetometry response for different external B_{DC} applied through the coil. The data along vertical axis are offset for clarity. (d) A plot of number of oscillations versus external field from (c) shows linear dependence in the measured range.

alternating magnetic field (RF) present in the wire. Now, if a small B_{DC} is applied thorough the coil positioned close to the GMI wire, clear changes in the number of oscillations of original Echo signal is observed. As an example, in the figure 2.8c, the Echo signals are obtained by setting the f_{ac} to be equal to $1/(2\tau)$ (200 kHz), where 2τ=5 μs is the total duration of the Echo sequence. The results in the figure correspond to signal measured for a constant 2τ (and f_{ac}) at different values of external B_{DC}. Along the horizontal axis amplitude of the driving signal (V_{pp}) is varied from zero to a maximum of 1.0V. It is evident from the figure that as the B_{DC} is increased from zero, the signal oscillations steadily reduce. This is due to the fact that the GMI wire response to external B_{DC} is encoded in the phase accumulated by the NV center, which can be observed as reduced number of oscillations.

On the contrary, if we had a usual MW antenna made of copper or gold material, it would not lead to observable changes in the NV-Echo signal upon the application of external B_{DC}. This feature of the NV-GMI interaction is utilized to demonstrate the sensitive magnetometer. For the present NV, the number of oscillations are observed to decrease from about 10 to 3, if the field value was increased from zero to $\sim$200 μT (figure 2.8d). While this observation indicates the dependence of the NV-GMI sensor to external B_{DC}, to quantify the sensitivity of the sensor to B_{DC}, one needs to employ a slight variant of the method as explained in the following section (section 2.4.2.2).

The applied I_{DC} from the current source could be varied over a wide range (-100mA to 100mA). For a wider I_{DC} range it is convenient to measure the field-dependent shifts using standard ODMR experiment than Ramsey method. Figure 2.9 shows the results from OMDR experiment where the B_{DC} produced from the coil is plotted for various I_{DC}. Figure 2.9a is the estimated value of field produced from the coil, calculated using standard parameters such as I_{DC} and coil diameter. The B_{DC} at the location of the NV is computed using field dependent ODMR shifts and Zeeman relation (figure 2.9b). The resulting B_{DC} shows non-linear behaviour with I_{DC} in some regions. For the magnetometry experiments using NV centers the field from the coil was calibrated in the region where the linear effects are present and this region was used to apply known values of B_{DC} from the coil. The overall behavior and magnitude of B_{DC} produced versus I_{DC} applied was almost same for all NVs in a given confocal area.
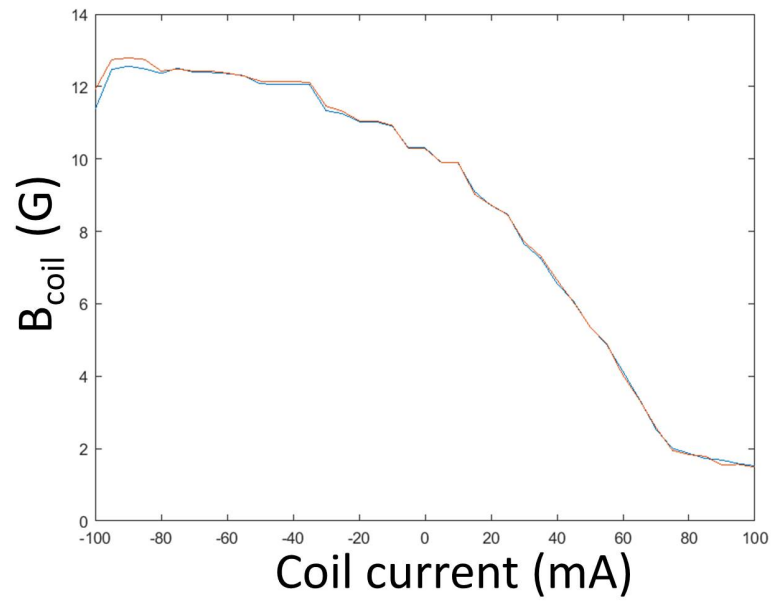
(a)
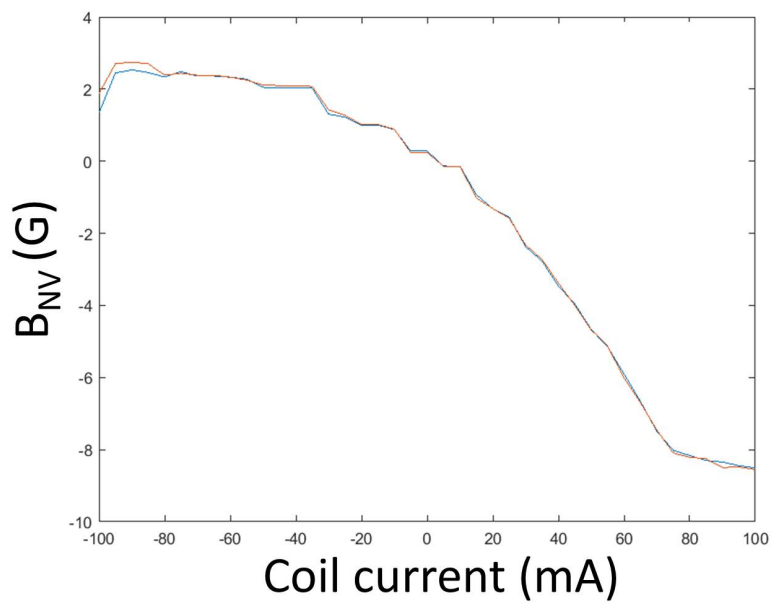
(b)

Figure 2.9: Estimation of actual field produced from the coil (a), and the field value at the location of NV (b) as calculated from the ODMR experiment. The field values are given in Gauss.

2.4.2.2   Calculation of DC field sensitivity ($\eta_{\mathbf{DC}}$)

For quantifying the sensitivity of the combined GMI-NV magnetometer to external B_{DC}, a Hahn-Echo based method similar to the one described in the beginning (figure 2.8a) of this section is presented. The experimental sequence can be thought of as consisting two paths. Path-1 consists of MW pulse sequence applied to the NV center from one Channel (CH1) of the AWG. Path-2 consists of RF driving signal with an amplitude (V_{pp}) and frequency (f_{ac}) applied from the second channel (CH2). The Echo sequence is both frequency and phase locked to the RF signal, and hence is synchronous with it (figure 2.8a). Both Path-1 (MW) and Path-2 (RF) are combined at the Bias-Tee, and applied to the GMI wire simultaneously. The f_{ac} and V_{pp} of the RF signal is chosen such that the GMI effects come into play.

If the amplitude of the external DC magnetic field (B_{DC}) is slowly varied while keeping RF amplitude (V_{pp}) as constant, we obtain periodic oscillations in the NV fluorescence signal. The sensitivity of the GMI-NV sensor is then calculated by analyzing these oscillations. In figure 2.10, the oscillation of the Hahn-Echo signal as a function of the amplitude of the B_{DC} from the coil is plotted. The minimum detectable magnetic field (B_{min}) of the GMI-NV magnetometer is calculated by (as explained in the section 1.5.2) [11],

$$B_{min} = \frac{\sigma_s}{\left(\frac{dS'}{dB_{DC}}\right)} \tag{2.13}$$

where σ_s is the standard deviation and $\frac{dS'}{dB_{DC}}$ is the maximum slope of the Echo signal. For a RF driving-signal of constant frequency f_{ac}= 200 kHz and amplitude (1.0 V), a DC field sensitivity $\eta_{\mathrm{DC}} = B_{min}\sqrt{t} \approx 67$ nT/$\sqrt{\text{Hz}}$, where t is the total measurement time, is obtained.

Conventionally, the Echo based methods are employed to sense alternating fields and are by nature insensitive to slowly varying or static fields (Chapter One). In the GMI-NV based method, the GMI element acts like an antenna for external weak B_{DC} and is inherently insensitive to any AC fields. The changes in its Z and hence the resulting magnetic information which gets encoded into NV spin state purely depends on changes in DC fields. For the calculation of η_{DC} mentioned here, the frequency of alternating current (with fixed amplitude) is locked to Hahn-Echo sequence only to maximize the NV phase acquisition. The response of the GMI wire to external DC fields results in the modifications of otherwise constant NV spin state dependent signal. If the B_{DC} is varied continuously but slowly, the NV spin state evolves with 2π periodicity, as in a typical magnetometer signal. By measuring the standard deviation (σ_s) of resulting fluorescence signal normalized to the rate (slope) of this evolution, one can calculate the photon-shot noise limited sensitivity of the GMI-NV sensor.

In a way, the Echo based DC magnetometry described here can be thought of as a method in which an up-conversion of DC field to AC field is carried out first. The up-conversion takes place through the changes in impedance, Z (of the GMI) which is an AC quantity. The Echo sequence senses the (up-converted) AC signal and converts the AC signal back to the DC signal like a rectifier. Finally, this DC field could be measured by observing the NV fluorescence oscillations.
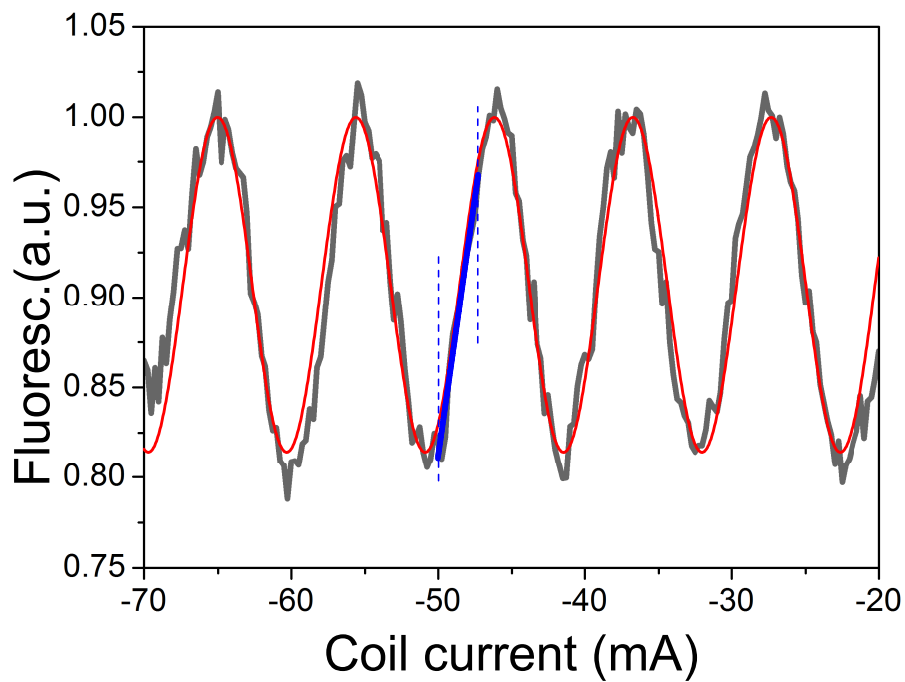
Figure 2.10: Demonstration of DC magnetic field sensitivity of the GMI-NV hybrid sensor. Oscillatory response of the Hahn Echo signal as a function of the amplitude of the external DC magnetic field (Coil current) is observed. The f_{ac} is set to 200kHz (or $2\tau = 5$ μs). It is estimated that the coil produced a DC magnetic field of 1.3 G (or 130 μT) for the current from -70 mA to -20 mA. The η_{DC} of the sensor is calculated from the maximum slope (indicated by blue solid line) of the response, where the sensor is most sensitive to the DC field changes. A value of $\eta_{DC} \sim 67$ nT/$\sqrt{\text{Hz}}$ is obtained. Solid gray line is the measured oscillatory signal and red line is sinusoidal fit.

Sensing method	η_{DC}
Ramsey, $\Delta\gamma$ (MHz)	
0.904 (NV1)	32.3 μT
0.503 (NV2)	17.9 μT
0.563 (NV3)	20.1 μT
NV-GMI (NV1)	67 nT

Table 2.2: Comparison of η_{DC} achievable with standard Ramsey method and that achieved with NV-GMI sensor. The Ramsey signal linewidth ($\Delta\gamma$) for three different NVs are given in MHz.

On the other hand, in a conventional Echo based sensing of AC fields, in addition to locking the signal frequency to the Echo sequence, the amplitude of the signal is ramped from 0 to finite values, and corresponding NV oscillations are recorded. In the present case, the RF signal is only used to drive the GMI effects in the material and its amplitude is kept constant. Whatever changes that appear in the NV signal are purely due to variation of DC field. Ramsey or ODMR method is a straight forward way to measure the B_{DC}, but the corresponding η_{DC} is limited by inhomogeneous dephasing time, (T_2^*). With Echo-based method the sensitivity could be improved by $\sqrt{\frac{T_2^*}{T_2}}$ due to the prolonged interrogation time (T_2^*).

2.4.2.3 Comparison with Ramsey based magnetometry

As a comparison, with standard Ramsey measurement, a $T_2^* \approx 1.5$ μs (figure 2.7b)) was obtained on this NV. The Fourier transform of this signal gave a full-width at half-maximum linewidth of (0.904±0.12) MHz. This corresponds to a photon shot-noise limited DC sensitivity, η_{DC} of 32.3 μT, obtained by dividing the linewidth by γ_e of NV.

Therefore, the value of η_{DC} = 67 nT/$\sqrt{Hz}$ is at least two orders of magnitude improvement compared to achievable η_{DC} of ~ 32 μT using the standard Ramsey magnetometry. Table 2.2 gives a comparison of η_{DC} of three different shallow NVs with the η_{DC} achieved from the hybrid sensor.

Echo based magnetometry was compared with FID (Ramsey) magnetometry for the same NV center. In the absence of any RF signal to the GMI signal, a FID pulse sequence with a constant τ applied to the NV center (figure 2.11a). A value of τ = 1 μs was chosen as it is the maximum possible interrogation time available from a FID method for this NV. Amplitude of external B_{DC} was varied step-wise and at each point the corresponding NV fluorescence signal is recorded. The resulting periodic oscillations represent the typical FID magnetometry signal (figure 2.11b). Notice that the reduced coherence time compared to Hahn ($T_2^* < T_2$) results in the few oscillations and hence the less sensitive magnetometer.

2.4.3 Dependence of sensitivity on RF driving parameters

For the demonstration of nT-sensitivity of GMI-NV sensor (in figure 2.10) a nominal value of 2τ = 5 μs (f_{ac} = 200 kHz) was chosen. This ensures that the τ is within NV center's coherence time (T_2) and is sufficient to provide a good SNR in the spin contrast. In

(a)

(b)
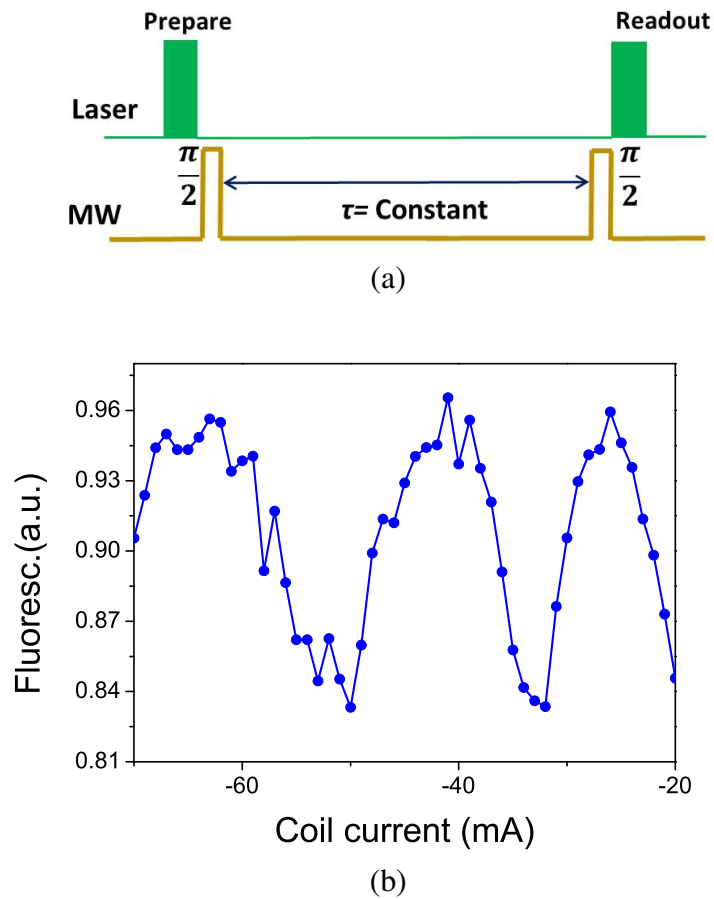
Figure 2.11: (a) Schematic diagram of the FID magnetometry sensing B_{DC} without the RF driving of the GMI wire. (b) Due to relatively short T_2^* time and the absence of GMI effects, the number of oscillations in the magnetometry signal and hence the sensitivity to external field are limited. Here the $\tau = 1$ μs is fixed and the NV fluorescence shows sinusoidal oscillations as a function of amplitude of external B_{DC}.
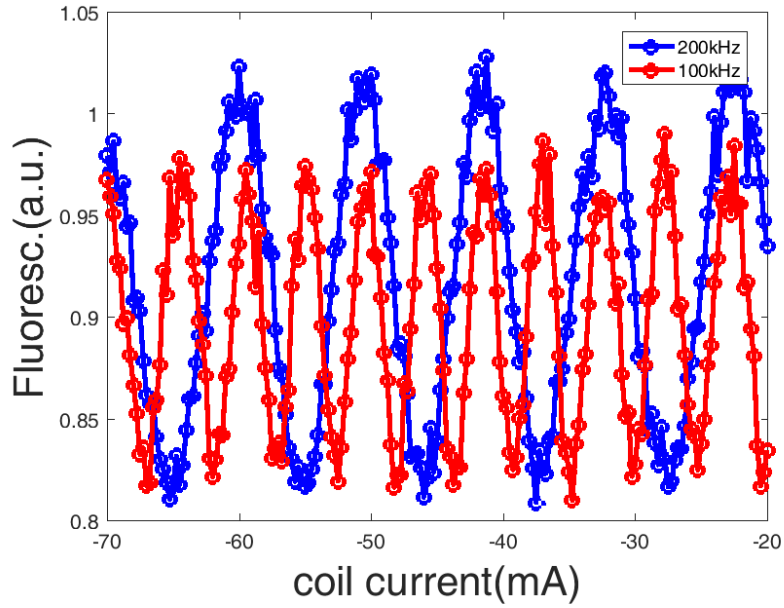
Figure 2.12: Hahn magnetometry signal as a function of amplitude of the external DC field for two RF signal frequencies, 100 kHz and 200 kHz. For a given RF amplitude (1 V here), decreasing the RF frequency by half (or increasing the τ) results in twice the increase of phase acquisition by NV and hence doubling the number of oscillations in the Echo signal at the cost of reduced SNR.

addition, the chosen f_{ac} lies within the range of frequencies where GMI effects come into play (>100 kHz). The lower limit for f_{ac} or $1/(2\tau)$ is set by the inverse of T_2 ($1/25\mu s \approx$ 40 kHz for this NV), because beyond this limit there exists no coherence and the SNR drops to zero. The upper limit for f_{ac}, in principle depends on the minimum value of τ which can produce oscillations in the magnetometer signal and the duration of π pulses (or the inverse of NV Rabi frequency, Ω_R). For the GMI-NV system studied here, the maximum possible value of f_{ac} that produced detectable oscillations was in the range of 1-10MHz. Therefore, by assuming the T_2 time as measured from Hahn experiment exists upto 20 μs for single shallow NVs, the f_{ac} has a bandwidth of roughly 50kHz-10MHz.

If we increase the τ, number of oscillations in the magnetometer signal correspondingly increases at the cost of reduced NV fluorescence contrast (see e.g., figure 2.12). Doubling of the frequency from 100 kHz to 200 kHz reduced the number of oscillations by half. In addition, if the RF driving frequency is kept constant, while its amplitude is increased, the number of oscillations in the magnetometer signal correspondingly increases (figure 2.13). For a given f_{ac} of 100 kHz, the number of oscillations increase from three for starting amplitude (V_{pp}) of 0.25 V to about ten for 1.0 V. Therefore, more the number of oscillations, maximum is the sensitivity (η_{DC}) to external field. Hence, the calculation of η_{DC} (in figure 2.10) was done at $V_{pp} = 1.0$ V where the maximum oscillations are obtained.

Notice that the value of T_2 obtained from Hahn experiment is not the intrinsic or ultimate coherence time of the NV sensor. The dynamic decoupling (DD) protocols, for example, as discussed in the previous chapter can prolong the T_2 to its intrinsic or actual value. Hahn-Echo magnetometry sequence described in this chapter can be replaced with a DD sequence which is appropriately tuned in frequency and phase with the driving
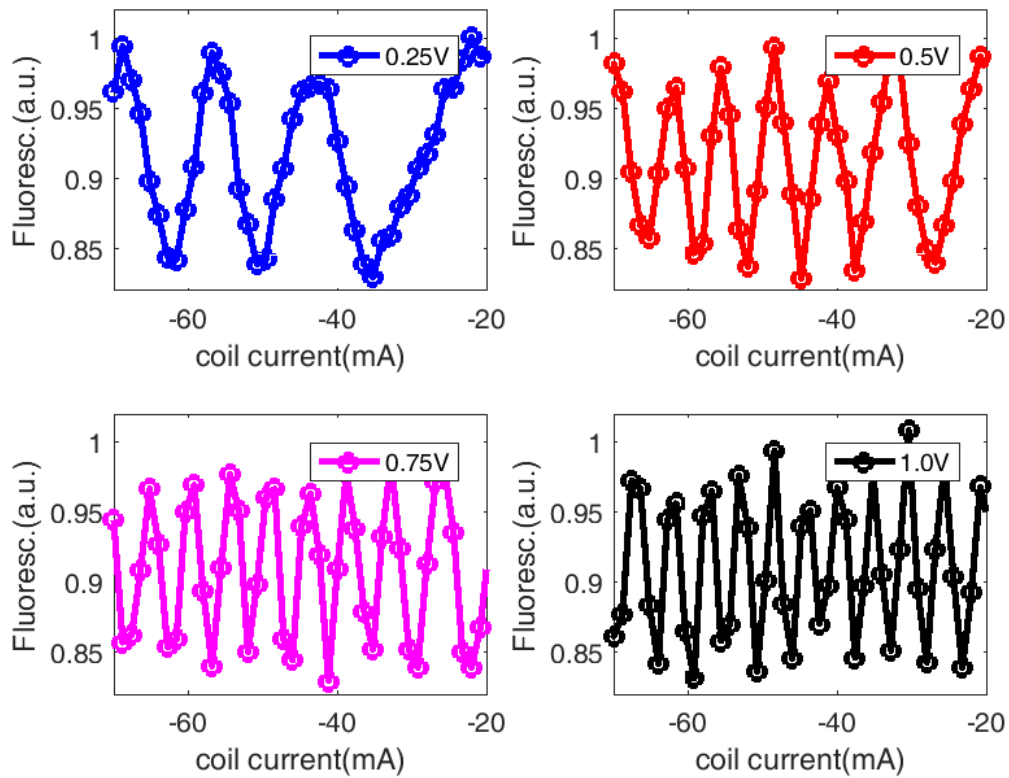
Figure 2.13: Hahn magnetometry signals as a function of external DC field amplitude for various RF amplitude (V_{pp} = 0.25, 0.5, 0.75, and 1.0 V). For a given f_{ac} (here 100 kHz), the number of oscillations in the Echo signal increases as the amplitude of RF driving signal is increased.

RF signal. This, in principle is expected to lead to more number of oscillations in the magnetometry signal and hence the enhanced η_{DC} values due to the longer interrogation times.

2.4.3.1 Validation of GMI-NV interaction

The enhancement of the DC field sensitivity presented in the previous section is due to possible near-field interaction of the GMI element and the NV center, given their close proximity ($\sim$ tens of μm). In the conventional GMI sensors, the response of the GMI to external weak fields is monitored by measuring the voltage drops across pick up coils made of many turns. In the present case, NV center due to its high sensitivity to external fields picks up the changes in Z of the GMI element via magnetic interactions. In order to verify that such interactions are indeed playing a role, number of experiments can be performed. In fact, the initial experiments mentioned in section 2.4.2 provide an indication that NV center is sensitive to external DC fields via its interaction with the GMI wire.

In the first set of experiments, the same NV-Echo sequence (shown in figure 2.8a) but with varying conditions can be employed to test the claim of enhancement of η_{DC}. First, in the absence of any RF signal to the GMI wire, a Hahn-Echo sequence with a constant τ (5 μs) was applied to the NV center. The external B_{DC} amplitude was varied step-wise and at each point the corresponding NV fluorescence signal is recorded (figure 2.14a). The signal shows no oscillations and it remains flat at its high value ($\sim$0.94). This is due to the fact that when there is no RF driving, the impedance Z of the element remains constant and does not respond to external B_{DC}. Here, the NV center does acquire a phase due to its high sensitivity to external B_{DC} during the first half (2.5 μs) of its Echo duration, but this phase gets canceled by the equal and opposite phase acquired during the second half of Echo sequence. Thus, no phase dependent oscillations are observed in Echo signal (figure 2.14a).

In the figure 2.14b, same Echo sequence was used in the first channel and a phase locked RF signal with constant amplitude and frequency was applied in the second channel, like in case of usual magnetometry experiments. But, the coil is switched off ($I_{DC} = 0$) so that there was no B_{DC} present in the vicinity of GMI or NV center. Although there is a RF signal present in the wire, the wire's Z values are intact as there is no B_{DC} which would modify the skin depths (δ) of the alternating (RF) current in the wire. The wire encodes no magnetic information to the NV center and NV spin state remains unperturbed. This again leads to absence of oscillations in the Echo signal. These experiments clearly demonstrate that the GMI element is indeed seeing the changes in the DC fields and these changes are being sensed by the NV center.

Further, it is also important that the RF signal applied to the wire was in synchronization, both in frequency and phase, with the Echo sequence applied to the NV center. Suppose, a RF signal with arbitrary frequency and phase is simultaneously applied to the wire, the corresponding Echo response shows no sensitivity to external B_{DC}. In the figure 2.14c, for example, the GMI wire was driven with a very high frequency (100 MHz) and arbitrary phase, while the Echo sequence was maintained at constant τ = 5 μs (200 kHz). As mentioned in the section 2.4.2, frequency of the RF signal is chosen according to several constraints, such as NV Rabi frequency and its T_2. Consequently, the present frequency range (of 200 kHz) is not necessarily an optimum frequency range for the present GMI
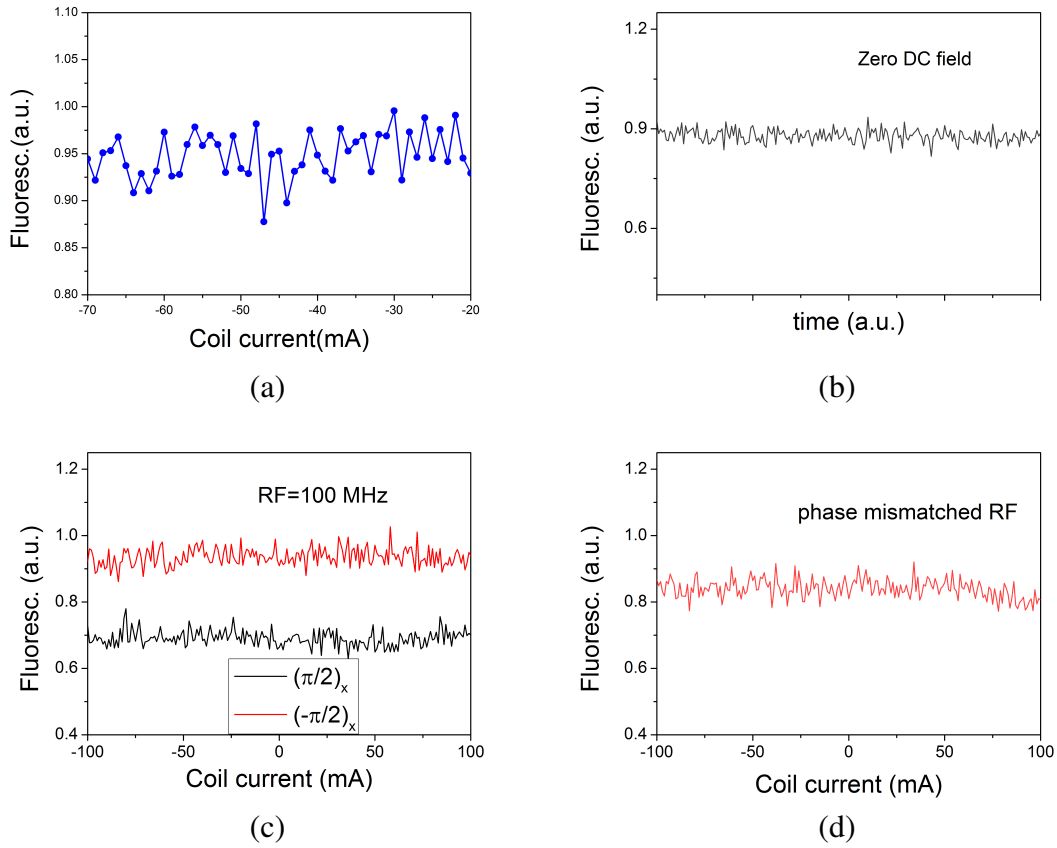
Figure 2.14: Validating the enhanced sensitivity of NV center due to GMI effects. In (a)-(d) a constant NV spin Echo sequence ($\tau = 5$ μs) subjected to various conditions are presented. (a) In the absence of any RF driving of the GMI element. (b) A phase matched RF signal applied to the wire, but no DC field from the coil is present. (c) both frequency and phase mismatched RF driving of the wire. The two data sets correspond to sign of the first $\pi/2$ pulses in the Echo sequence inverted with each other. (d) frequency matched but the phase mismatched. In all these cases the Echo signal remains constant and does not show any oscillations.

material, since the GMI values vary drastically as a function of frequency and are expected to show maximum changes at f_{ac} above 10 MHz. Even though the GMI wire may show relatively maximum sensitivity to DC fields at 100 MHz, these changes can not be picked up by the NV center due to the large mismatch of two time scales (5 μs and 1/(100 MHz)). Therefore, simply by increasing the GMI frequency (as in figure 2.14c) does not lead to corresponding enhancements in η_{DC} of NV.

In figure 2.14d, the frequencies of the Echo sequence and RF signal were matched, but their phase was mismatched. Again it can be observed that the resultant phase acquired by the NV center is zero and the sensor shows no sensitivity to changes in external B_{DC}.

Thus, the results in figure 2.14 confirm that there is a magnetic interaction between the NV center and the wire resulting in the enhanced η_{DC}.

In the following, second set of experiments to validate that the interaction of NV center with GMI material are presented. To make sure that the enhanced η_{DC} effects are specific to GMI wires and to exclude the possibility of artifacts arising from the experimental setup, a comparison of alternating current values of the GMI wire with other two materials, namely

83

copper and gold micro wires which are normally used for MW manipulation of NV spin was done. Table 2.3 summarizes the measured alternating current (I_{ac}) values for these three materials for a fixed frequency (200 kHz) and applied voltage (1 V) across the wires. As the resistances of all the three wires (GMI, Cu and Au) are comparable (1-10 Ω), the measured I_{ac} were also found to be comparable. This implies that for the same amount of applied current, the ability of the GMI wire to magnetically interact with the NV is much more plausible than that of non-GMI materials like copper and gold.

Material	Resistance (Ω)	i_{ac} measured (μA)
Au coated GMI wire	10.5	1.0
Cu μ-wire	2.5	1.0
Au μ-wire	1.2	8.0

Table 2.3: Comparison of i_{ac} values for GMI wire and two other wires (made of Cu and Au) with similar dimension. Although almost a same amount of current flows through all the three wire, the enhancement of magnetic interaction is more prominent with GMI wire as exemplified by enhanced NV sensitivity to external B_{DC}

2.4.4 Tuning the GMI wire properties

To maximize and stabilize the GMI response to external B_{DC}, certain standard techniques routinely used in the GMI sensor research were employed. These are mainly the metal electrodeposition and Joule heating or annealing. While the electrodeposition helps to stabilize the Z, the annealing improves the $\Delta Z/Z$.

It is reported that the properties of GMI wires are sensitive to thin layers of metal on the surface. For example, presence of Ni/Cu layer is known to enhance the GMI sensitivity and stability [201, 202]. Bare magnetic micro-wires posses large end-to-end resistance and show poor wettability to metal bonding. The electrodeposition process eliminates this problem by effectively increasing the wettability of the wire, which in turn reduces the undesired contact resistance and stray capacitance, and also stabilizes the Z.

Since for NV-GMI sensor the GMI wire needs to be soldered to coplanar waveguide, poor wettability of the wire results in the increased contact resistance and destabilized Z response of the wire. In order to overcome this, the GMI wires were deposited with thin layer of gold through the standard process of electroplating [203]. A current density of $\sim$5 mA/cm^2 at room temperature for a duration of 10 minutes produced a few μm layer of gold on the surface of $\sim$ 25 μm diameter GMI wire (figure 2.15a). A typical NV Echo signal for a plated and bare wire is shown in the figure 2.15b. The standard Echo experiment in figure 2.15b is done with a fixed NV-Echo duration, τ. The RF signal (with its f_{ac} matched Echo sequence) is applied simultaneously to wire and along the horizontal axis the V_{pp} of RF current is ramped. No external B_{DC} is present. The resulting oscillations from a bare wire show non-linear response with V_{pp} and presence of higher harmonics in the sinusoidal Echo signal. It turns out that even though apparently the wire shows fast response, in the DC magnetometry (as in section 2.4.2.2) experiments, this does not translate into any improvements in the η_{DC}.

It should be noted that the thickness of the plated Au layer has to be carefully adjusted to get optimum sensitivity. For too thin layer of plating (less than about 1 μm), the

(a)

(b)
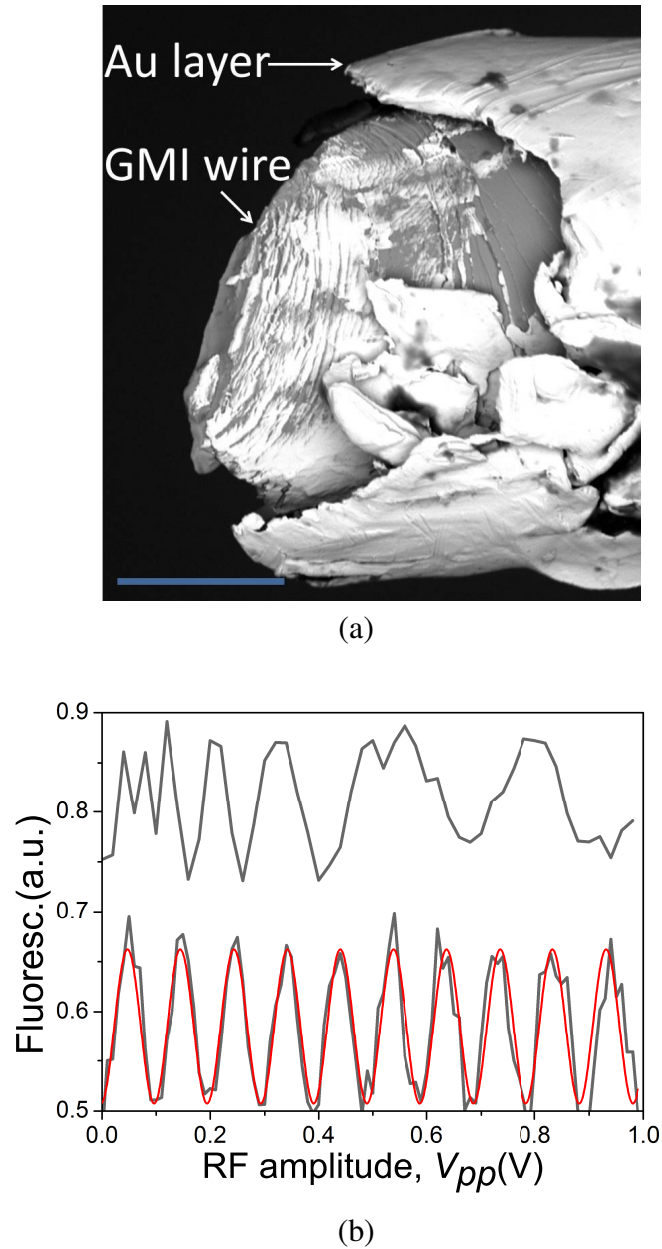
Figure 2.15: (a) Scanning electron microscope (SEM) image of GMI wire plated with a thin layer of gold. The image is taken at the fractured end of the wire. Scale bar is 10 μm. (b) Echo response of the bare (top) and gold plated (bottom) GMI wire. Along the horizontal axis the V_{pp} is ramped upto 1.0 V and the corresponding NV oscillations are recorded. A smooth and steady oscillations in the plated wire is compared with bare wire where the oscillations show fast response at small V_{pp}, but gradually decay at higher V_{pp}. The Echo signals are offset along vertical axis for clarity.
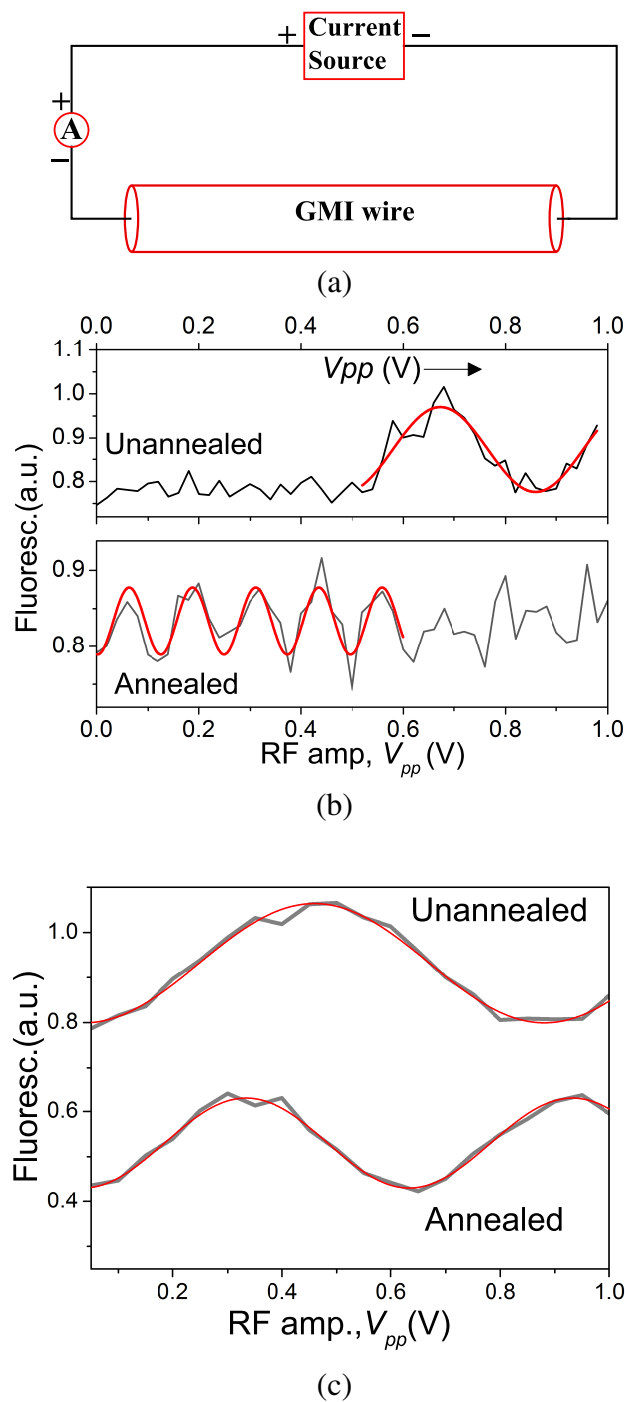
Figure 2.16: Effect of current annealing. (a) Schematic of the current annealing of GMI wire. Red rectangle is a current source and 'A' is the current meter. (b) For a fresh wire annealing significantly improves the wire response to RF signal compared to an unannealed wire (see text). (c) On an aged wire, the annealing seems to have little effect in improving the wire response.

magnetometer shows the typical bare-wire characteristics- i.e., non-linear response. For the case of too thick layer of plating (over 10 μm), the GMI properties tend to be suppressed due to the dominance of gold layer and the wire behaves like an ordinary metal.

On the other hand, the Au-coated wire appears to have fully stabilized the GMI response as can be seen from the smooth and linear modulation of Echo signal with V_{pp} (bottom data, figure 2.15b). Most of the plated wires subsequently showed more sensitivity to the external B_{DC} than the bare wire. Therefore, for all the sensing experiments mentioned in this chapter plated wires are used.

In GMI materials the domain structure and their movements play a key role. This factor critically depends on the preparation and post-processing methods. It has been reported that subjecting the GMI material to high temperatures by passing a direct current tailors their magnetic and mechanical properties for the sensors applications [204, 205]. This process is known as 'Joule-current annealing' and is found to modify the domain structure in favor of better sensitivity to external B_{DC}. Joule heating is usually done close to 100 mA [206]. For the present case the Joule heating of the gold plated wire is studied and it is observed that although the process helps to increase the sensitivity compared to an unannealed wire, the change is not very consistent. Figure 2.16b shows an example in which the NV Echo signal is studied (for $B_{DC} = 0$) for the case of before annealing and after annealing. Oscillations in case of fresh and unannealed wire start only at a higher amplitude of the RF signal and completes one cycle at the point of maximum V_{pp}. For the same wire the joule heating is performed by passing high direct current using a current source (*Keithley 6221*) as shown schematically in the figure 2.16a. The wire is subjected to incremental current from 0 to 100 mA in steps of 20 mA, with a 10 minutes current flow time and 10 minutes of delay between two successive steps. The resulting wire shows an enhanced response as it is evident from an increased number of oscillations even at small V_{pp} values (figure 2.16b).

But this enhancement was not consistent for all the wires studied and some wires showed no change post-annealing. Also, the GMI properties appear to degrade over time and the sensitivity of even the plated wires showed lower values over the course of several months. For example, in figure 2.16c, annealing results from a wire which is about 6 months old (post fabrication by melt extraction) are presented. As it can be seen, even the same procedure of Joule current annealing failed to increase the number of oscillations and the GMI effects were not revived. Hence, the Joule-heating in the context of GMI-NV needs further careful investigations. Additionally, as the GMI wires are collected from the process of melt extraction, they exhibit varying diameters (from 20-60 μm). This also results in inconsistent responses of the GMI-NV magnetometer for sensing applications. Hence, it is important to find an optimum size and length of the GMI material which produces best η_{DC}. Further, performing experiments in a magnetically shielded environment could mitigate any adverse effects of geomagnetic fields on the NV-GMI magnetometer.

2.4.5 Noise floor

The ultimate sensitivity or the minimum possible magnetic field (B_{min}) that can be detected using a sensor is given by its noise floor level in the magnetic noise spectral density. For
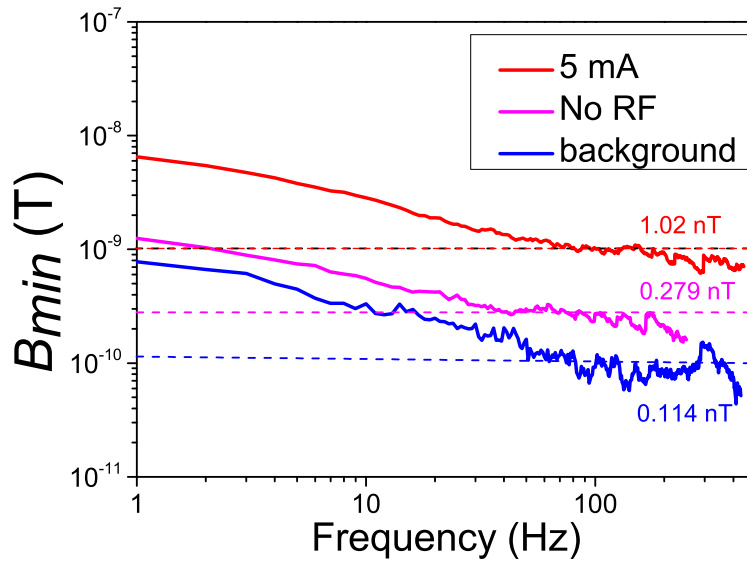
Figure 2.17: Noise floor of the GMI-NV sensor. Data in red color corresponds to magnetically sensitive GMI-NV sensor and has a noise floor of ~ 1 nT. The data in the middle (magenta) represents the magnetically insensitive configuration (i.e., no RF driving of the GMI wire) and has a noise floor of ~ 0.3 nT. The data in blue is acquired without the presence of any laser, MW pulse and RF signal. Correspondingly, the lowest noise floor of ~ 0.1 nT from the background is obtained.

the GMI-NV hybrid sensor, figure 2.17 shows the results of noise spectral density and associated noise floor levels. The results in the figure are obtained by, recording the photon counts for a duration of 1 s with a sampling rate of 1 kHz. Then, the Allan deviation of this signal is determined, and the B_{min} at each point is calculated by dividing the Allan deviation by the contrast of the magnetometer signal. The time domain data is converted into frequency domain using fast Fourier transform and the variation of B_{min} versus frequency describes the noise spectral density. In figure 2.17, the noise spectral density of the magnetometer for three different conditions are presented. In the first case, the noise spectrum is recorded under the usual GMI-NV magnetometry conditions. Here, the f_{ac} is set to 200 kHz and synchronized to NV-Echo sequence. A small external B_{DC} is applied by passing 5 mA of current through the coil. The sensor is thus magnetically sensitive. A noise floor level of 1.02 nT is obtained and it is the best achievable B_{min} for the present GMI-NV sensor. In the second case, noise spectrum of magnetically insensitive configuration is presented. Here, only a NV-Echo sequence is applied while the GMI wire is not driven with any RF signal. The corresponding noise spectrum results from the technical noise of the setup and has a noise floor of 0.279 nT. In the third case, both laser and MW pulses are also switched off, and only the background fluorescence signal was collected. This constitutes an electronic noise and has a lowest noise floor of 0.114 nT among three cases.

2.4.6 Possible improvements and applications

The GMI-NV based Hahn-Echo magnetometry presented here is a proof-of-concept method and its sensitivity is mainly limited by the photon-shot noise. Perhaps it is possible to further improve the η_{DC} of the GMI-NV hybrid sensor. Use of double quantum (DQ) magnetometry methods [207] might provide twice the sensitivity. Since the η_{DC} critically depends on the readout efficiency (F), the F can be improved by following methods. First, by improving the photon collection efficiency using schemes like diamond nanopillar waveguides [208] or circular diamond gratings [209]. Second, by employing recently proposed spin-to-charge conversion methods for NV spin state readout [210] would enhance the F. Third, using nuclear spin assisted readout schemes [211] the F can be significantly improved. At least a factor of 10 improvement in η_{DC} could be achieved with these advanced methods. This would mean that the DC field sensitivity η_{DC} could approach a few nT/$\sqrt{\text{Hz}}$, which is close to the single NV center's currently achieved AC-field sensitivity ($\sim$nT/$\sqrt{\text{Hz}}$).

On the other hand, the limitations of η_{DC} on the relatively shorter T_2 time of the NV center can be overcome if one employs the continuous sampling scheme of Qdyne [150, 151]. Since the interrogation time scale of these schemes depends, not on the NV relaxation time, but rather on the stability of the external clocks, they achieve arbitrary spectral resolution. By implementing such a scheme for the GMI-NV sensor, it is expected that NV center's sensitivity to can be greatly enhanced beyond that is reported in this Chapter. Precisely, as the Qdyne offers a spectral resolution of $1/T$ (where, T is the total measurement time with reference to an external clock), NV sensor is capable of detecting very minute changes in the impedance (Z) of the GMI material in response to external B_{DC}. In this case, the GMI wire can be driven with any known f_{ac} which produces maximum response to B_{DC}, and the NV center stroboscopically samples the magnetic signal from the GMI wire. Thus, the achieved η_{DC} can potentially reach pT/$\sqrt{\text{Hz}}$ and even better.

Instead of single NV centers, if ensemble NV centers are used then the η_{DC} of the resulting GMI-NV sensor can potentially be improved. The η_{DC} of ensemble NV sensors is shown to be in the sub-pT range/$\sqrt{\text{Hz}}$ [19] and scales by a factor of $1/\sqrt{N}$ (where, N is the number of NV defects in the ensemble) [18]. Since the theoretically achievable η_{DC} of standalone GMI sensors are in the range of ft/$\sqrt{\text{Hz}}$ (see section 2.2.5), by combining the GMI with NV ensembles one can possibly push the η_{DC} of hybrid sensors down to ft/$\sqrt{\text{Hz}}$. This provides us a sensor operating in ambient conditions and whose sensitivities are comparable to those of SQUIDs and atom vapor magnetometers. However, the readout method of such a hybrid sensor involves micrometer scale area encompassing the ensemble defects and the advantages of having a single defect as readout unit will have to be compromised.

In place of micrometer scale GMI material, one can think of positioning nanoscale GMI structures, both to enhance the η_{DC} of a single NV-GMI sensor (due to more localized type of interaction between a single NV and nano-GMI material), and to achieve a highest spatial resolution (because the overall sensor is now miniaturized). The idea of hybrid sensor scheme presented in this Chapter can be utilized to combine in general other magnetic systems with the NV center to enhance the NV's sensing abilities. Perhaps, it is possible to enhance the η_{DC} of a single NV center using nanomagnetic structures such as magnetic thin films (two dimensional or 2D), nanowires (1D) or magnetic clusters (0D) fabricated directly on top of the diamond crystal. Due to the low dimensionality of these

systems, their spatial separation from NV center can be greatly reduced and hence the mutual magnetic interaction can be enhanced. When these systems respond to external B_{DC} in their vicinity, the NV center quickly encodes that magnetic information, and by reading out NV's spin state, one can expect to measure B_{DC} with high sensitivity.

Regarding the applications of GMI-NV sensor is concerned, one can visualize many platforms where the sensor can be useful. Along the lines of recent works with NV centers for detection of neuron action potentials [199], since the biological specimen could be brought in contact with the GMI-NV sensor, it could potentially allow the extracellular detection of bio-magnetic field activity from such systems with much better spatio-temporal resolution.

A GMI-NV based sensitive DC magnetometer with advanced spatial resolution could be highly desirable in the area of sensing biomolecules and biomagnetism. Due to the high sensitivity of the GMI sensors, they have been shown to detect the binding of about 30 functionalized magnetic micro-particles with the target molecules on the surface of the sensor which is about 1 mm in length [212]. As the combination of NV with the GMI wire provides the added the advantage of much higher spatial resolution, with proper optimization of GMI-NV method, it is possible to detect a single or few molecules with the GMI-NV sensor.

In the medical diagnostics such as magnetoencephalography and magnetocardiography (study of magnetic fields generated by human brain and heart, respectively), SQUID based sensors which provide $\eta_{DC} \sim$ fT are routinely used [213]. However, these sensors require cryogenic temperature and magnetically shielded room, besides consuming high power and contributing to overall operating costs. Further, due to the presence of thick dewar thermal insulation the sensor to subject distances are greatly increased ($>$30 mm). This reduces the spatial resolution. On the other hand, GMI based sensors are already demonstrated to be capable of non-invasive detection of magnetic fields down to 100 pT from the living tissues and organs [214]. It would be immensely useful to have a sensor that can provide high spatial resolution, thereby potentially replacing the SQUID based sensors which are current state of the art. With proper optimization, GMI-NV based sensors can thus be developed in this direction. Such a hybrid sensor overcomes most of the above mentioned limitations of SQUIDs.

2.5   Chapter conclusion

A novel static field magnetometer combining the advantages of highly sensitive magnetoimpedance material with a single defect center in diamond operating at the ambient conditions has been demonstrated. Here, the GMI material acts as a sensitive element to small external field changes, and a NV center located nearby is used measure the material's response. The achieved static field sensitivities, in the range of tens of nT are atleast two orders of magnitude better than those of standard T_2^* based single-NV magnetometers. Thus, the method achieves η_{DC} close to η_{AC} of single NV sensors. The presented hybrid sensor system has a noise floor of about 1 nT. Unlike the classical GMI based sensors which contain bulky sensor head, here due to atomic size of the NV defect, the hybrid sensor is capable of detecting nT fields with miniaturized readout system. The reported sensitivity of the hybrid sensor is still a few orders of magnitude lower than the actual sensitivity

of the GMI sensors, which are in the range of pT. By making certain improvements one can envision of GMI-NV hybrid sensor with minimal experimental resources, for various applications.

Chapter 3

Probing phase transitions in a soft matter system using NV centers

This chapter deals with the nanoscale nuclear magnetic resonance (nano-NMR) studies of a soft condensed matter system using single NV centers in diamond. The soft matter system chosen for the study is Liquid crystals. A NV center close to the surface of the diamond used as a nanoscale probe to sense the temperature dependent phase transitions of the Liquid crystals. The NV center detects these phase transitions in its nanoscopic detection volumes. Potential advantages of using atomic scale defects such as NV centers in probing the phase transitions in soft matter systems and their access to study rich physical phenomena in such systems at nanoscale is discussed.

3.1   Introduction

Depending on the structural rigidity of the materials, the condensed matter can be broadly classified into two sub-categories viz., 'Hard' and 'Soft' condensed matter. 'Hard' condensed matter generally deals with basic building blocks of matter like electrons, atoms and molecules, and their interactions. The term 'soft condensed matter' is used to describe materials which posses low elastic moduli (several orders smaller than that of metals) and can be easily deformed by mechanical or thermal means [43, 215, 216]. Common examples of soft matter include-polymers, liquid crystals, gels, emulsions, colloids, surfactant assemblies, granular systems and many biological materials. These materials also known as 'mesoscopic systems' because the atoms in such systems are organized into entities whose length scales are larger than the individual atoms but are much smaller than the overall size of the materials. The large sizes of these structural entities and relatively weak interactions that hold them together causes the materials to posses softness. All soft matter systems share a common property that their important physical behaviors occur at thermal energy scale of $k_B T \sim 10^{-21}$J at room temperature (k_B is Boltzman constant and T is temperature.) [43].

Some of the fascinating aspects of the nature are manifested when the states of matter undergo phase transitions. Understanding the microscopic origins of macroscopic phase transitions has profound impact in studying superconductivity, magnetic ordering, topological materials, ferroelectricity, superfluidity, rigidity and fluidity of biological cell

membranes etc [215, 217–219]. In all these systems the phase transitions are often characterized by complex behaviors such as the abrupt or continuous changes and discontinuities or fluctuations in the associated parameters which have their origin in the interactions between the individual entities and their collective behavior at the micro or nanoscale.

Among the soft matter systems, Liquid crystals (LC) whose properties are intermediate between those of crystalline solids and conventional liquids form an important class of materials with relevance to several scientific studies and technological applications. They are also known as useful and simpler model systems to address certain fundamental physical problems in cosmology [220, 221] and self assembly of biological matter like DNA which show liquid crystalline phases [222, 223]. There exist analogies between the phase transitions in liquid crystals and those in the metal-superconductor transitions [224]. The study of defects present in the liquid crystals presents a relatively simple systems to understand the more complex defects in other condensed matter systems [225]. At the nanoscale it still remains a major challenge to non-invasively obtain the information about structure and dynamics of these defects across the phase transition. Furthermore, other properties like fluidity or elasticity of soft materials in nanoscopic volumes, which are markedly different from their bulk counterparts, could provide important insights about such systems. The exact nature of transitions between some of the LC phases (nematic to smectic, mentioned below) and whether they are universal are still under debate. In these contexts nano-NMR might provide a significant insights in understanding these phenomena.

In the area of Liquid Crystals (LC), the NMR spectroscopy is routinely used as a major analytical tool due to its elemental sensitivity and ability to provide distinct fingerprints of the molecular structure and interactions of its chemical species with one another. Due to their dependency on induction coil based detection schemes and hence the low sensitivity, the traditional NMR techniques require large sample volumes to generate the signal from thermally polarized spins. As a result it is not possible to obtain information about the sample in smaller (nanoscopic) volumes.

NV centers have now been demonstrated to be potential candidates for performing the NMR spectroscopy at the nanoscale at ambient conditions [30, 31]. Besides, they are also capable of measuring temperature with ∼mK resolutions [13]. Therefore, NV sensors offer a unique advantage of probing soft matter systems at the nanoscale by precisely measuring the temperatures. In this Chapter, a NV based NMR noise spectroscopy scheme to detect phase transitions in a LC material as it undergoes transition from more ordered phase close to room temperature to disordered phases at higher temperatures is demonstrated. This particular material, when heated above room temperature, known to exhibit two distinctly ordered liquid crystalline phases before becoming an isotropic liquid at its clearing point (around 40°C). The LC material was placed directly on top of the diamond crystal and the phase transitions were induced by changing the temperature. The single NV centers situated at a few nanometers below the diamond surface were used as a probe to detect the phase transitions. Instead of thermal polarization, the NV-NMR method employed here measures the NMR signals due to statistical polarization of the hydrogen spins in the LC sample across the phase transition. Dependence of linewidth (Γ_p) of this proton magnetic resonance signal as a function of the temperature indicates that the NV center could detect the phase transitions in the nanoscopic volumes of the LC material above the diamond

surface.

3.1.1 Introduction to Liquid Crystals

Apart from the three conventional states of matter namely solids, liquids and gases there exists an intermediate state known as liquid crystals. As the name suggests their properties are intermediate between solids and liquids, in that they maintain certain order like crystals while still being able to flow like liquids. As a consequence they exhibit some optical properties characteristic of solids like birefringence and at the same time a liquid-like response to shear. Certain organic materials while undergoing phase change from solid to liquid (or vice versa) might actually show such an additional liquid crystalline phase (s). There are two categories of liquid crystals: Thermotropic and Lyotropic liquid crystals.

Liquid crystals whose phase transitions are caused solely by change of temperature are known as Thermotropic liquid crystals. In such systems the main criterion for the appearance of LC ordering is due to shape anisotropy and structural rigidity of the constituent molecules. The shape anisotropy of the molecules forces them to exhibit orientational order as it minimizes the overall energy of the system. There are varieties of molecular shape anisotropies that result in stable LC phases, among them the simplest are rod-like and disc-like molecules. The complex ones are bent or V-shaped molecules. In these molecules the hard parts (like benzene rings) provide the rigidity of a solid while the long flexible alkyl chains provide the fluidity of a liquid.

In Lyotropic liquid crystals the phase transitions are caused by both temperature and concentration of the molecules (solute) in a solvent (usually water). The molecules which give rise to this LC phase are known as amphiphilic molecules and there are a wide range of lytropic LC structures possible which have direct relevance to living systems. But as this thesis deals only with the thermotropic liquid crystals, the lyotropic liquid crystals will not be discussed anymore.

3.1.1.1 Thermotropic liquid crystals classification

Among thermotropic liquid crystals most common are the calamitic or liquid crystals of long, rod-like molecules. Due to the anisotropic nature of the molecules the refractive indices along the long molecular axis and perpendicular to it are different. This leads to LC materials being birefringent and each phase shows distinct characteristic textures when viewed between the crossed polarizers. This helps to identifie the different LC phases optically. In the following, different LC phases that *can* arise as the sample is cooled below its isotropic phase are explained.

The simplest LC phase is 'Nematic' (N_1), which occurs below the isotropic clearing point and here the molecules are approximately oriented along their long molecular axis over a long range (3.1a). The average direction of orientation is called as director and is given by a dimensionless unit vector $\hat{n}$ with both $-\hat{n}$ and $\hat{n}$ are being equivalent (i.e., apolar). The nematic phase does not have a positional order. As a result the nematic phase has a discrete rotational symmetry (along $\hat{n}$) and a continuous translational symmetry. Thus, they are liquid-like along transversal directions while still maintaining orientational order along longitudinal direction. The orientational ordering of rod-like elongated molecules in

the nematic phase can be well described by an orientational order parameter, S_1 which is a scalar. S_1 is defined based as the average of the second Legendre polynomial [44],

$$S_1 = \langle P_2(\cos\theta) \rangle = \left\langle \left(\frac{3\cos^2\theta}{2} - \frac{1}{2} \right) \right\rangle \tag{3.1}$$

where θ is the angle between the orientation of long molecular axis and the local director $\hat{n}$, and the brackets denote both spatial and temporal averaging. A value of $S_1 = 0$ indicates a randomly oriented isotropic liquid phase and $S_1=1$ corresponds to a perfectly oriented crystal. Generally for liquid crystals S_1 takes the intermediate value of 0.3 to 0.8 and sharply drops to 0 at the liquid crystal to isotropic phase transition (3.1b). Experimentally the S_1 can be measured by various ways- dielectric relaxation, x-ray diffraction, optical (birefringence, light scattering), magnetic (diamagnetism, NMR, EPR) methods.

As the sample is further cooled, it undergoes a phase transition to a more ordered phase known as the 'Smectic' phase. By 'more ordered' it means in addition to the orientational order as in nematic, there exists one dimensional (1D) positional order in which the molecules are stacked into well defined equidistant layers. Depending on the types of positional and orientational order a material can show different types of smectic phases (but not necessary that all materials show more than one type of smectic ordering). The most common smectic phase is known as Smectic A (S_A) phase in which the molecules are stacked along the layer normal and there exists no additional order within the layers (figure 3.1a). That is, within the layers molecules can freely move like in an ordinary liquid and the layers themselves can slide over one another. If the molecules within the layer are tilted with respect to the layer normal then the phase is called smectic C (S_C). In smectics, there exists a discrete translational symmetry along layer normal and a discrete rotational symmetry along $\hat{n}$.

The ordering in S_A phase is described in terms of a complex order parameter [215]

$$\psi = |\psi| \exp\{(i\Phi)\} \tag{3.2}$$

here $|\psi|$ is the degree of layer ordering ($|\psi|=0$ for nematic phase). If the smectic layers are stacked along the layer normal (z-axis) with a periodicity $\lambda = 2\pi/d$, then the phase factor Φ given by $\Phi = \lambda z$, determines the position of smectic layers. d stands for the layer spacing.

In addition to the two simple LC phases, nematic and smectic phase mentioned above, there exist a wide varieties of LC phase in the calamitic materials depending on the nature of the molecules (for e.g., if the molecule is chiral), types of positional and orientational ordering within the layers, etc. But for the work mentioned in the thesis, it is sufficient to discus only N_1 and S_A phases.

Table 3.1 shows a rough classification of the matter and some of the important aspects frequently mentioned in this chapter.

3.1.2 Phase transitions in Liquid Crystals

3.1.2.1 Nematic to isotropic transition

Various experimental measurements indicate that in the N_1 phase, the order parameter S_1 decreases continuously as the temperature is increased and drops abruptly (a first

States of matter/Phase	Positional order	Orientational oder	Elasticity	Fluidity
Solid (crystalline)	✓	✓	✓	×
Smectic	Quasi	✓	✓	✓
Nematic	×	✓	✓	✓
Isotropic liquid	×	×	×	✓

Table 3.1: A gross classification of materials depending on some important parameters frequently mentioned in this chapter.

order transition) to zero at the nematic to isotropic ($N_1 - I_1$) transition temperature (T_{NI}) (figure 3.1b). The theoretical description of the nematic to isotropic phase transition is given by Maier-Saupe [226–228] based on general Landau theory [229]. It successfully explains the behavior of S_1 near the $N_1 - I_1$ transition. Only a brief description of the Maier-Saupe theory is given in the following.

The Maier-Saupe theory employs the molecular mean field approach in which each LC molecule is considered as a hard-rod subjected to a mean potential field arising from interactions of its neighbours. Introducing a thermodynamic chemical potential $G(p, T)$ (where p and T are the pressure and temperature, resp.) such that it is minimum in the equilibrium state [44],

$$G(p,T) = G_1(p,T) + k_B T \int f_a \log(4\pi f_a) d\Omega + G_1(p,T,S_1) \tag{3.3}$$

where f_a is orientation distribution function for each molecule with long axis **a** (In general $f(\theta)$, where θ is the angle between molecular axis and $\hat{n}$- is maximum for $\theta = 0$ or π and minimum for $\pi/2$). $d\Omega$ is small solid angle and S_1 is the order parameter. In the equation 3.3 the first term is free enthalpy of the isotropic case, second term is the decrease in entropy of the system due to anisotropic anglular distribution, and the last term G_1 stands for the intermolecular interactions. By assuming G_1 is quadratic in S_1, $G_1 = -\frac{1}{2}U(p,T)S_1^2$ and minimizing the G (equation 3.3) with respect to all variations of f, one arrives at two solutions for $G(S_1)$ which correspond to minima in the equilibrium state. One is $S_1=0$ associated with an isotropic liquid. The other is associated with the N_1 phase below the transition point. Its value just below the transition point (T_c) is $S_1(T_c) = 0.44$. This value of $S_1(T_c)$ closely matches with the values of S_1 observed in various experiments measuring the order parameter and taken as a universal value for all $N_1 - I_1$ transitions. The behavior of the S_1 with respect to T is depicted in the figure 3.1b.

3.1.2.2 Smectic A to nematic ($S_A \rightarrow N_1$) transition

Following the Landau-Ginzburg theory for superconductor-normal metal transition, de Gennes developed a S_A to N_1 transition [224, 230].

As the molecules in the S_A phase are organized into layers the phase can be characterized by a density modulation in along $\hat{z}$ direction (orthogonal to the layer).

$$\rho(z) = \rho_0 + \rho_1 \cos\left(2\pi\frac{d}{z} - \Phi\right) \tag{3.4}$$
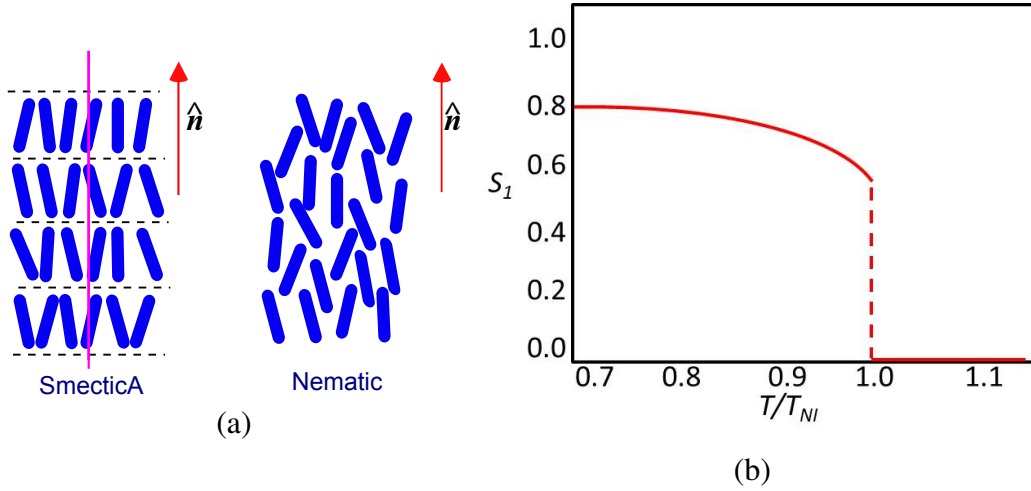
Figure 3.1: (a) Molecular ordering in the nematic and smectic A phase. The director $\hat{n}$ denotes the average direction of orientation. In smectic, the molecules are stacked into layers (black dotted lines) with a 1D postional ordering along the layer normal (vertical magenta line). (b) Temperature dependence of order parameter S_1 in the nematic and isotropic phase. T_{NI} is the isotropic clearing temperature.

where, ρ_0 is the average density, ρ_1 is the amplitude, d is the layer spacing and Φ is the phase factor. For nematic ρ_1 is 0. Thus the smectic order parameter can be conveniently described by a complex order parameter (already given in equation 3.2),

$$\psi = \rho_1 \exp\{(i\Phi)\} \tag{3.5}$$

In the vicinity of the $N \to S_A$ transition the free energy may be expanded in the even power of ρ_1,

$$F_s = \alpha\rho_1^2 + \beta\rho_1^4 + ... \tag{3.6}$$

where α and β are material constants. Due to the coupling between ρ_1 and the nematic order parameter (orientational) S_1, the free energy can be written as,

$$F = \alpha\rho_1^2 + \beta\rho_1^4 + [(\delta S_1)^2/2\chi] - C\rho_1^2\delta S_1 \tag{3.7}$$

where, δS_1 is a change in the nematic order due to layering of the smectics, $\chi(T)$ is a response function which is large near the nematic-isotropic transition T_{NI} and small for $T < T_{NI}$ and C is a positive constant. Minimization with respect to δS_1 gives,

$$F = \alpha\rho_1^2 + \beta'\rho_1^4 \tag{3.8}$$

where, $\beta' = \beta - \frac{1}{2}C^2\chi$. For a wide nematic range, $\chi(T_{AN})$ is small (T_{AN} is the smecticA to nematic transition temperature) and $\beta' > 0$, and the transition is second order. For a small nematic range, $\chi(T_{AN})$ is large and $\beta' < 0$ and the transition is first order. The point for which $\beta'=0$ is known as tricritical point (at which smectic A, nematic and isotropic phases meet) where the transition changes from first to second order.
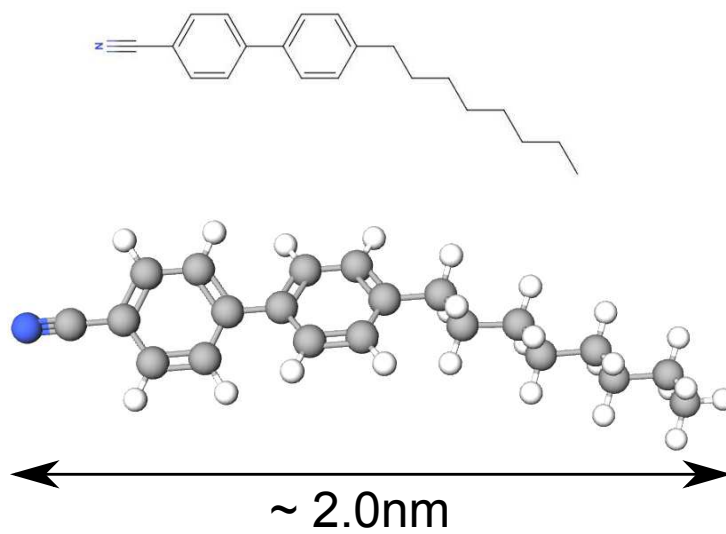
Figure 3.2: Molecular structure of 8CB liquid crystal (top) and its 3D image (below). The CN group serves as the polar part, central two benzene rings as the rigid core, and the alkyl hydrocarbon chain as the flexible and non-polar parts of the molecule.
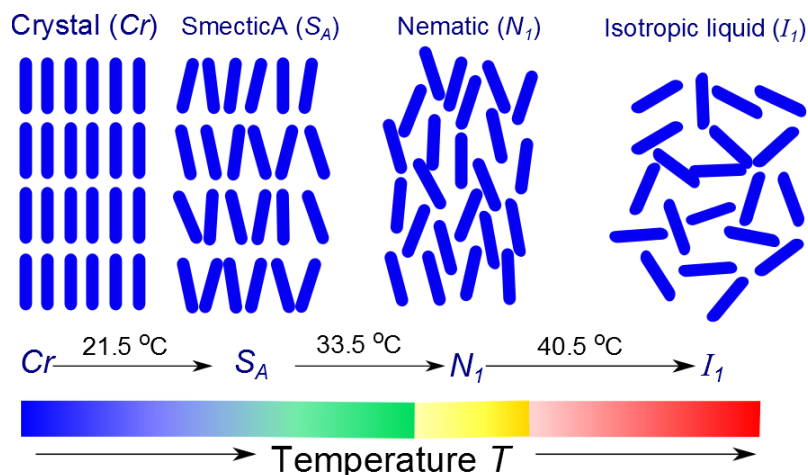
Figure 3.3: Schematic diagram of different phases of 8CB liquid crystal as a function of temperature, T.

3.2 Materials and methods

3.2.1 About liquid crystal material

For the phase transitions studies reported here, a standard liquid crystal 4-n-octyl-4'-cyanobiphenyl ($CH_3(CH_2)_7C_6H_4C_6H_4CN$; molecular weight 291.43; CAS Number 52709-84-9), commonly known as 8CB is used. The material was commercially obtained from Sigma Aldrich and is used as received. 8CB is known to exhibit LC behavior at room temperatures and its properties have been extensively studied in the literature. 8CB as a LC material offers a simple model system for understanding phase transitions in two dimensions [231]. There are several advantages of using 8CB as a model system. Mainly, as a standard soft matter system it offers access to study different phases close room temperature. Owing to the strong polar nature of the molecules [232] they readily adsorb on several hydrophilic surfaces, including diamond. This helps to investigate LC behavior using NV centers close to the surface.

In figure 3.2, the structure of the molecule is shown. The phase transition of 8CB LC is depicted in the figure 3.3. It undergoes a phase transition from Crystalline (Cr) state to smectic A (S_A) at 21.5 °C, from S_A to nematic (N_1) at 33.5 °C, and from N_1 to isotropic liquid (I_1) at 40.5 °C (also known as the clearing temperature). Owing to the strong electric dipole moment ($\sim$6 D, about three times that of water) of the molecule [232], the molecules in the smectic layer orient themselves in a such a way that their polar groups (CN) are anti parallel to each other. Such an organization reduces the electrostatic repulsion between the polar groups of the molecules. This makes 8CB molecules to pack in a so-called interdigitated bilayers fashion with the overall layer spacing 1.4 times the molecular length.

3.2.2 Sample preparation

The diamond sample used had a dimension of 2 mm$\times$2 mm$\times$100 μm. Prior to use, the sample was cleaned in a boiling solution of three acids (equal ratio of Nitric acid+Sulfuric acid+ perchloric acid) for several hours with a reflux condenser. This acid treatment, apart

from removing any residual impurities (organic contaminants and graphitic carbon) on the diamond surface, makes the diamond surface oxygen terminated and hence hydrophilic (water-liking). For nano-NMR sensing of the liquid crystals, the single shallow NVs at a few nm depth were used. The procedure for fabricating shallow NV centers has been described in the chapter one. A small drop of 8CB LC was placed on the diamond surface containing shallow NV centers and allowed to spread over the surface. Due to the hydrophilic nature of the diamond surface, the LC wets the surface and forms a thin layer (in the μm range) on the diamond surface. As mentioned above, the 8CB exhibits S_A phase starting from 21.5°C and hence it appears as a cloudy liquid at room temperature (around 23°C). The diamond was then placed on a 170 μm microscope cover glass (figure 3.4). Before placing the diamond, a copper wire of 30 μm diameter was drawn on top of the cover glass and its ends were soldered to a microwave (MW) stripline. This copper wire acts as a MW antenna for the MW manipulation of NV spin. The diamond with its liquid crystal coated side facing the copper wire was fixed on the cover glass by applying small amounts of adhesive (*Pattex Super glue*) on its sides.

Another way to produce thin layers of LC film on the diamond surface is to use standard spin coating method. But, probably due to the very small size of the substrate (2mm×2mm diamond chip), it was difficult to optimize the uniform coating of the film on diamond.

3.2.3 Temperature settings

Heating the 8CB LC above room temperature value causes it to undergo phase transitions. The diamond crystal was heated from above using a Peltier temperature controller (*ET-071-10-13-RS Adaptive module*; dimension: 20 mm×20 mm×3.6 mm). A thin (0.5 mm) copper plate of dimension 25 mm×45 mm was fixed on the diamond and was in thermal contact with the diamond. The Peltier controller was then firmly fixed on top of this Cu plate. This ensures the uniform heating up of diamond and accommodates the relatively bulky Peltier controller. The top surface of the Peltier was also equipped with small heat sinks to achieve optimum heating performance of the Peltier element. The Peltier was driven by a variable DC power supply. By slowly increasing the voltage, the temperature (T) of the Peltier can be increased. The Peltier also showed reversible T change (within ±0.5° C) over a wide range if the voltage was varied back and forth. As the diamond is heated from above, due to excellent thermal conductivity property of the diamond, the LC film on the other surface of the diamond also gets heated up. Therefore the T value measured on the top surface of the diamond is almost equal to the T of the LC film underneath. To measure the T on the diamond surface, a PT100 temperature sensor (1/3 DIN type) was used. The PT100 was fixed on the copper plate at one corner using a thermal conducting tape. By measuring the resistance of the PT100 in a 3-point-probe measurement, the temperature (T) at the Peltier and hence at the LC film can be indirectly calculated. Before doing experiments at different T, the Peltier was allowed to stabilize at each T value for at least an hour.
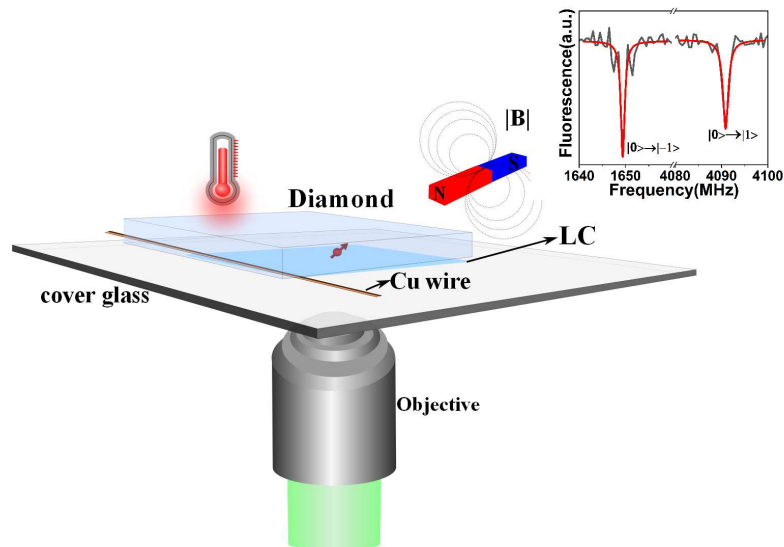
Figure 3.4: A simplified schematic diagram of the experimental setup for performing nano-NMR of LC. The shallow NV center (red sphere with an arrow) on the bottom side of the diamond was imaged by looking through the cover glass and a thin layer of LC material. The diamond was heated from above. Inset shows the typical ODMR spectrum for |B| around 400 G.

3.2.4 Experimental setup

The experimental setup consisted of a home-built confocal microscope equipped with NV electron spin resonance (ESR) system as explained in the Chapter One. The confocal microscope comprised of a 532 nm laser for optical excitation of NV center, an oil immersion objective (UPlanSApo 60X, NA:1.35) for focusing the laser onto the sample and collecting the fluorescence signal from the NV. Following the standard confocal design, the fluorescence from the sample focused onto a 25 μm pinhole and detected using a single avalanche photo detectors. For the LC experiments reported here, the excitation laser power at the sample was set to $\sim$500 μW. The NV count rate was about 100 kcounts/s against the background counts of $<$5 kcounts/s. As shown in the schematic figure 3.4, the the microscope objective was in vertical position while the sample was in horizontal position with respect to the plane of the optic table (this helps to avoid the flowing away of LC material and ensures its presence on the surface of diamond even when it is heated to its more fluidic phases).

An arbitrary waveform generator operating at a sampling rate of 20 Gsps generates the optical pulses (through AOM) and MW pulses. The MW pulses generated in the AWG are amplified using a 16 W high power amplifier (ZHL-16W-43+, Mini-circuits) and applied to the sample through the 30 μm copper wire. The Rabi frequency obtained was in the range of 10-25 MHz, depending on the proximity of given NV center with the copper wire. A permanent magnet was aligned along the NV axis to provide a sufficient static magnetic field (|B|) to split the $m_s=\pm 1$ magnetic sublevels of the NV. The magnet was mounted on a linear positioning system with a fine movement (10 μm resolution) to adjust the magnitude of the field.
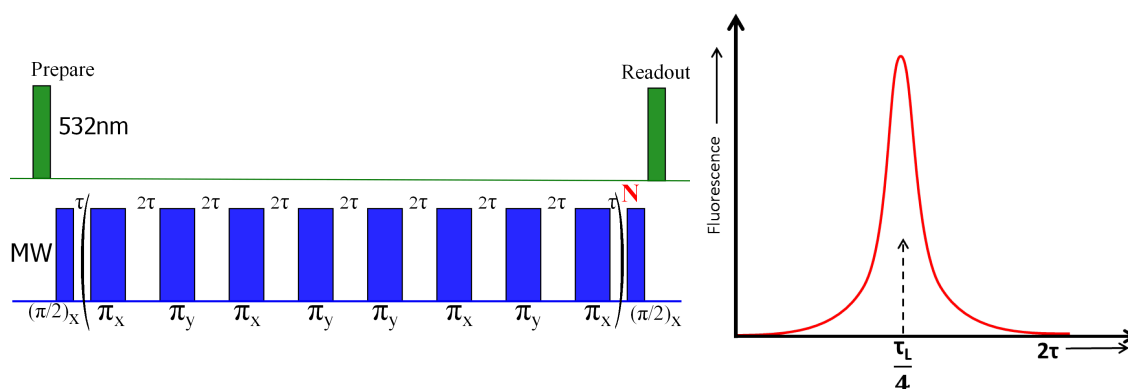
Figure 3.5: (Left) XY8-N dynamical decoupling sequence. Green pulses refer to 532 nm Laser and blue pulses refer to microwaves. N is the order of the XY8 sequence, N×8 is the total number of π-pulses were used. (Right) Spectrum of the spin noise with a Lorentzian centered around the Larmor frequency.

3.3 Results

3.3.1 Sensing the proton spin noise with dynamical decoupling

As shown in the figure 3.2, an 8CB molecule is mostly made up of hydrogen and carbons. As there are abundant hydrogen (protons) spins compared to ^{13}C the magnetic signal at the NV is dominated by protons in the LC molecules close to NV center. The experimental procedure involved the measurement of proton magnetic resonance signal from the 8CB LC in various phases using single NV centers. The experiments were performed over ten different NV centers and the corresponding proton signal linewidth (Γ_p) was measured in each case. A consistent trend in the change in signal Γ_p as a function of T indicates the presence of different phases of the LC material.

Only those NV centers which show no strongly coupled ^{13}C spins in their ODMR and FID experiments were chosen for the measurements as this would avoid the possible ambiguity in the proton signal in a XY experiment. Figure 3.5 (left) depicts the XY8-N pulse sequence used for recording the proton resonance signal from the LC material. Initially a green Laser pulse prepares the NV center in its m$_s$ = 0 (spin up) ground state spin. A MW $\pi/2$ pulse places the NV spin in a coherent superposition of its 'spin up' and 'spin down' ground states. A train of alternate (x and y) MW π-pulses separated by time 2τ, are then applied to the NV center. Each block consisting of 8 π-pulses are repeated N times to generate a total of 8×N π-pulses. The NV spin accumulates a net phase during this interval. A final $\pi/2$ pulse converts this phase into population difference between 'spin up' and 'spin down' ground states. Finally the fluorescence which is spin state dependent, is read out by an end laser. The XY dynamical decoupling sequence serves the two purposes: It decouples the NV spin from the stray magnetic noise in the NV surroundings and makes the NV spin only sensitive to narrow band signal centered at $\gamma_L = 1/4\tau$, the Larmor frequency. By sweeping the interpulse delay 2τ the entire spectrum of the spin noise in the NV surrounding can be recorded (figure 3.5, right).

Figure 3.6 shows the results of XY based proton sensing experiment in various LC phases for one particular NV. The four T values correspond to three different phases of the LC material. At each T, the spectrum was recorded and the data was fitted to a standard
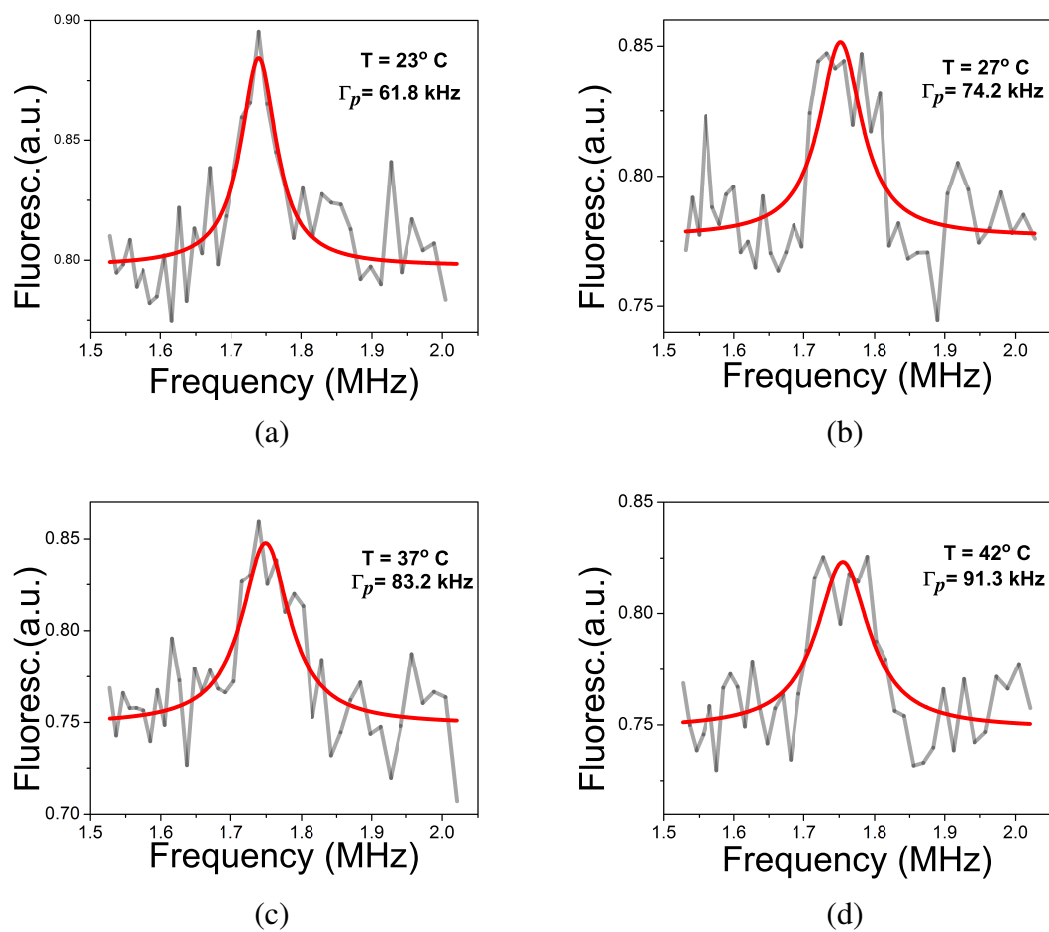
Figure 3.6: Proton signal linewidth (FWHM, Γ_p) as a function of temperature. (a) (room temperature) and (b) correspond to smectic phase of the LC, (c) for nematic phase, and (d) for isotropic liquid phase of the LC. Horizontal axis is the proton Larmor ($\gamma_L = 1/4\tau$) and vertical axis is the NV fluorescence. Gray and red lines are signal and Lorentzian fit, respectively. The T for each experiment was determined by measuring the shift of NV center's zero field splitting parameter, D.

Lorentzian model. The FWHM of the fitted curve gives the linewidth (Γ_p) of the proton signal and its value in different phases indicates the local dynamics of the LC molecules in the vicinity of the NV center. Starting from an initial room temperature of 23° C, the signal's Γ_p shows clear increase and reaches a maximum in the isotropic fluid at 42° C. For 23° and 27° C, where the material is in S_A phase, the Γ_p values obtained were 61.8±14 kHz and 74.2±21 kHz, respectively. These two different values possibly arise because, although it is the same smectic phase, as 23° is close to the $Cr \rightarrow S_A$ phase transition point (∼22° C) of the material, the complete melting of the material may not yet have happened and therefore it may be still exhibiting the properties of the crystal. The Γ_p increases to 83.2±20 kHz for the N_1 phase and a maximum value of 91.3±24 kHz for the fluidic I_1 phase. The experiments were carried out at a constant |B| of about 410.75 G and hence the peak of the signal appears at an average value of 1.7486 MHz for all T values, which is the Larmor frequency of the proton spins at this |B|.

NV as a dual mode sensor

Due to the dependence of NV center's zero field splitting parameter D on temperature, the T can be estimated by measuring changes in D [13]. In the range of temperatures studied here the D varies linearly with T and has a slope $\frac{\delta D}{\delta T} \approx$ -70 kHz/K. This allows us to monitor and precisely tune the temperature for bringing the LC molecules about their phase transitions. In the figure 3.6 the temperature values were calculated from measuring the changes in D from room temperature values. The T values measured directly on the diamond surface using external sensor (Pt100) matches within ±0.5° C with these values. This unique feature of NV center as a sensitive probe to spin noise as well as T values makes it a dual mode sensor for studying temperature-dependent phase transitions.

3.3.2 Creating statistics of linewidth variation

In order to see the general trend of the variation of the Γ_p versus T, the experiment was repeated for a total of 12 NVs. For all the experiments the external magnetic field was kept constant around 400 G. The summary of results obtained is shown in the figure 3.7. For each NV the Γ_p obtained from the XY8-N experiment at four different T are plotted. Note that the N value or the order of XY8 sequence varies from one NV to another. However, for a given NV the N was fixed for all the four T in which the experiments were done. Depending on how long the spin coherence time (T_2) of a given NV survives, the N was chosen. This is because, the T_2 value for each NV is different depending on its depth below the surface and the spin noise in its vicinity. The deeper the NV, longer is its T_2 and hence a higher order XY8 is required to see the detectable signal. Table 3.2 shows the total number of π-pulses (in a given XY sequence) used for obtaining the Γ_p mentioned in the figure 3.7.

It can be observed that for most of the NVs the Γ_p values show an increasing trend with increasing temperature. For a few NVs the the Γ_p values appear to be constant or even decreasing (NV1 and NV9, for example) across the phase transitions. This could be perhaps due to the presence of local effects like the voids or regions where no LC material is present, which resulted in the weaker spin noise experienced by the NVs. such inhomogeneity in the LC film can be expected due to the nature of film preparation method
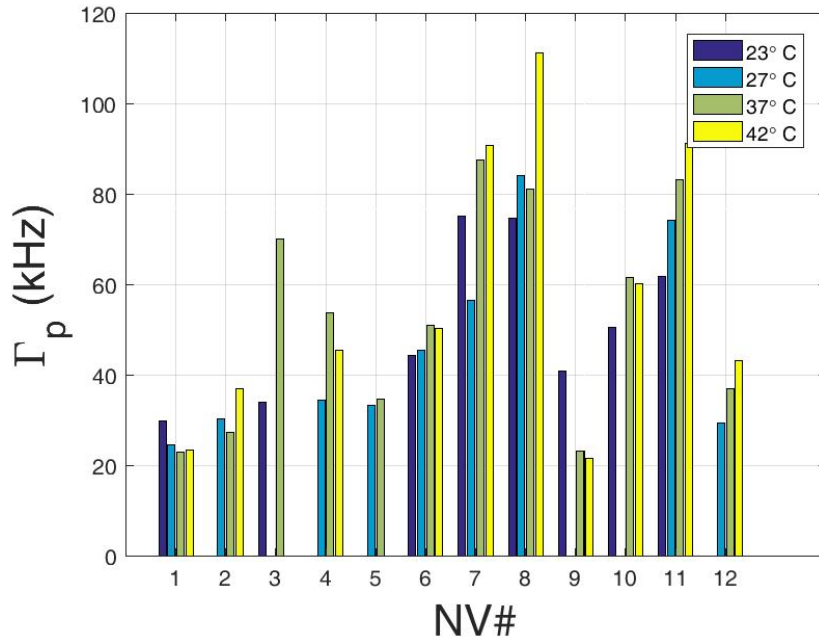
Figure 3.7: Proton Γ_p for various NVs at different T. The horizontal axis shows the number of NVs and the vertical axis shows the Γ_p for each NV at four different T values. The missing data points for some NVs correspond to poor fitting values which are omitted here.

NV number	Total number of π-pulses used	T_2 in μs.
1	512	146.4
2	128	30.7
3	200	52
4	128	29.4
5	256	64
6	256	65.5
7	256	66.6
8	256	62.4
9	128	44.3
10	128	44.3
11	512	87
12	256	48.6

Table 3.2: Total π pulses ($8 \times N$) used for the NVs plotted in the figure 3.7 along with the corresponding coherence time T_2 = total sequence length given by $2 \times N \times \tau$.
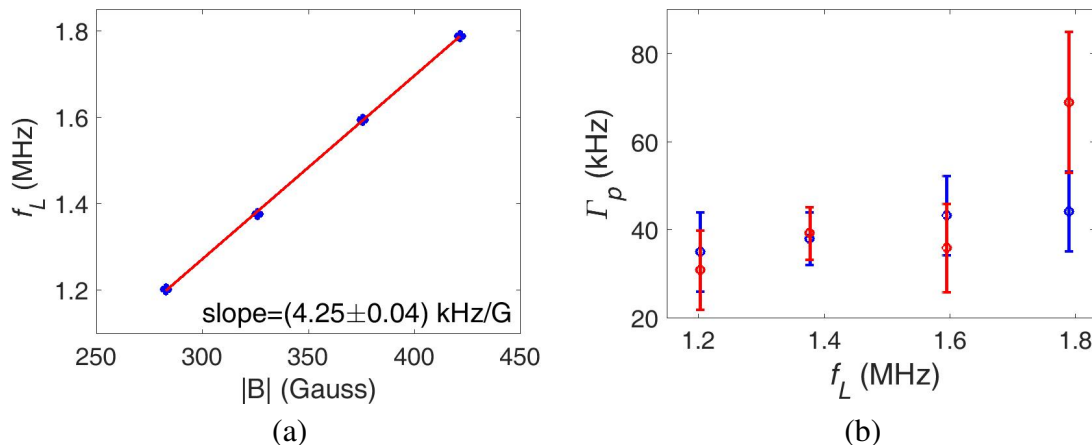
Figure 3.8: (a) Variation of Larmor frequency versus magnetic field. The slope of the straight line fit matches with γ_h (gyromagnetic ratio of the protons). Error bars are indicated but are much smaller than the actual values. (b) On the same NV, dependence of the signal Γ_p (from XY128) on the proton Larmor frequency at room temperature, is plotted. The two data sets (in blue and red) correspond to '+' and '-' sign of the last $\pi/2$ pulse in the XY sequence.

used here. The NVs were chosen at random positions from a confocal image of area $200 \times 200 \ \mu m^2$. This is to make sure that there exists a reasonable trend in the signal with respect to T and also to rule out increase in the Γ_p caused by other spurious effects.

Magnetic field dependence study

To confirm that the signal in the XY experiment was arising from the protons, the XY128 experiments were repeated at various magnetic field for one of the NVs (NV9). The variation of the obtained Larmor frequency values as a function of the |B| yielded a straight line (figure 3.8a) and whose slope of 4.25±0.04 kHz/G matches with the gyromagentic ratio of protons. Also for the same NV, figure 3.8b shows dependence of the signal Γ_p on the |B| (shown in terms of the corresponding proton Larmor frequency). As the field was decreased the signal Γ_p reduced or it became sharper.

Variation of NV $(T_1)^{-1}$ relaxation as a function of T

Figure 3.9 shows the measurement of NV's spin-lattice relaxation time (T_1^{NV}) as a function of temperature in the presence of LC film. The NV10 was used for this measurement. For a given temperature the NV center was initially optically polarized into $m_s = 0$ state ('Bright' state) using a green laser pulse. Then a resonant π pulse inverts the population into $m_s = -1$ state ('Dark' state) and after a waiting time τ the spin state was readout by another laser pulse at the end. T_1^{NV} time of the NV can then be measured by repeating the sequence for various values of τ and recording the fluorescence at each point, which shows an exponential decay. As shown in the figure 3.9a, the T_1^{NV} decreases with increase in the T or its relaxation rate ($1/T_1^{NV}$) increases (figure 3.9b). Although there is a clear change in the decay curves upon the change in T, perhaps this can not be solely taken as the detection of the phase transition. Because the NV centers show linear dependence of T_1 on
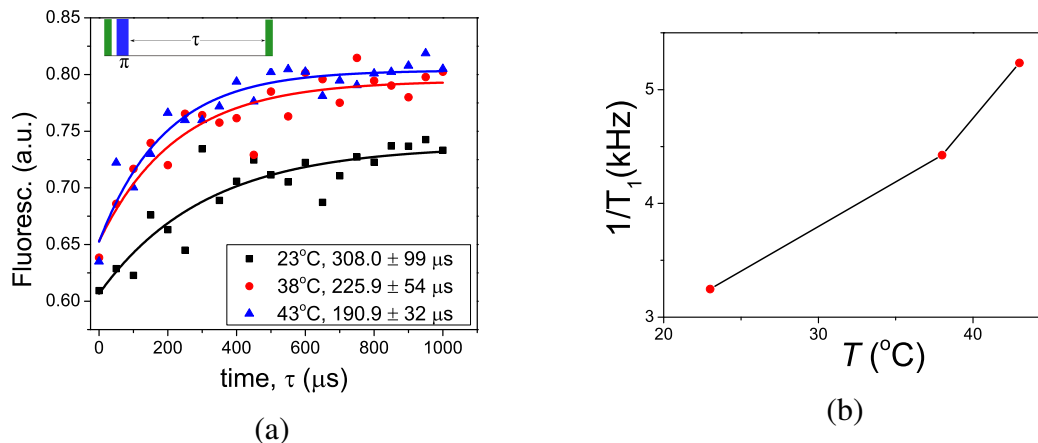
Figure 3.9: T dependence of the NV spin-lattice relaxation (T_1^{NV}) time in the presence of LC. (a) T_1^{NV} measurement for three different T. Scattered points are measured data and solid lines are fit to exponential decay curve. The upper inset shows the pulse sequence used for the measurement and the fitted T_1^{NV} values are shown inside a box at the bottom. (b) NV's spin-lattice relaxation rate, $1/T_1^{NV}$ as a function of T.

temperature in this temperature range and the order of $1/T_1^{NV}$ observed in our case matches with the already reported values [111, 233]. Thus there is ambiguity in determining if the changes in T_1^{NV} took place due to the NV's intrinsic response to T or due to the phase transition of the LC material close to it. Maybe it needs careful examination further.

3.4   Discussion

The results obtained here show that NV based sensing could be used to detect the LC phase transitions in nanoscopic volumes. Due to the more ordered nature of the smectic phase it is less fluidic compared to nematic and isotropic liquid phases. The above mentioned results indicate that as LC material undergoes phase transition to more liquid-like phases, the signal Γ_p increases. These results are qualitatively in agreement with the reported studies on NV based sensing of nanoscopic volumes of other systems where the line broadening was observed for more fluidic samples [39, 142, 146, 234]. The ultimate frequency resolution or narrowness of the measured proton signal depends on many factors: magnetic field, T_1^{LC} of the protons spins in LC, diffusion time scale of these spins (T_D) and T_1^{NV} time of the NV sensor itself [142].

3.4.1   Organization of LC molecules on diamond surface and NV sensing volume

As already mentioned in the section 3.2 the LC material was deposited on the diamond surface which was hydrophilic in nature due to oxygen termination. Based on the reports in the literature of organization of thin films of 8CB molecules on various hydrophilic surfaces such as water [231], silicon [235] or glass [236] we propose that almost a similar organization of molecules takes place on the diamond surface studied here. In figure 3.10 a possible organization of the molecules in the three different phases of 8CB and
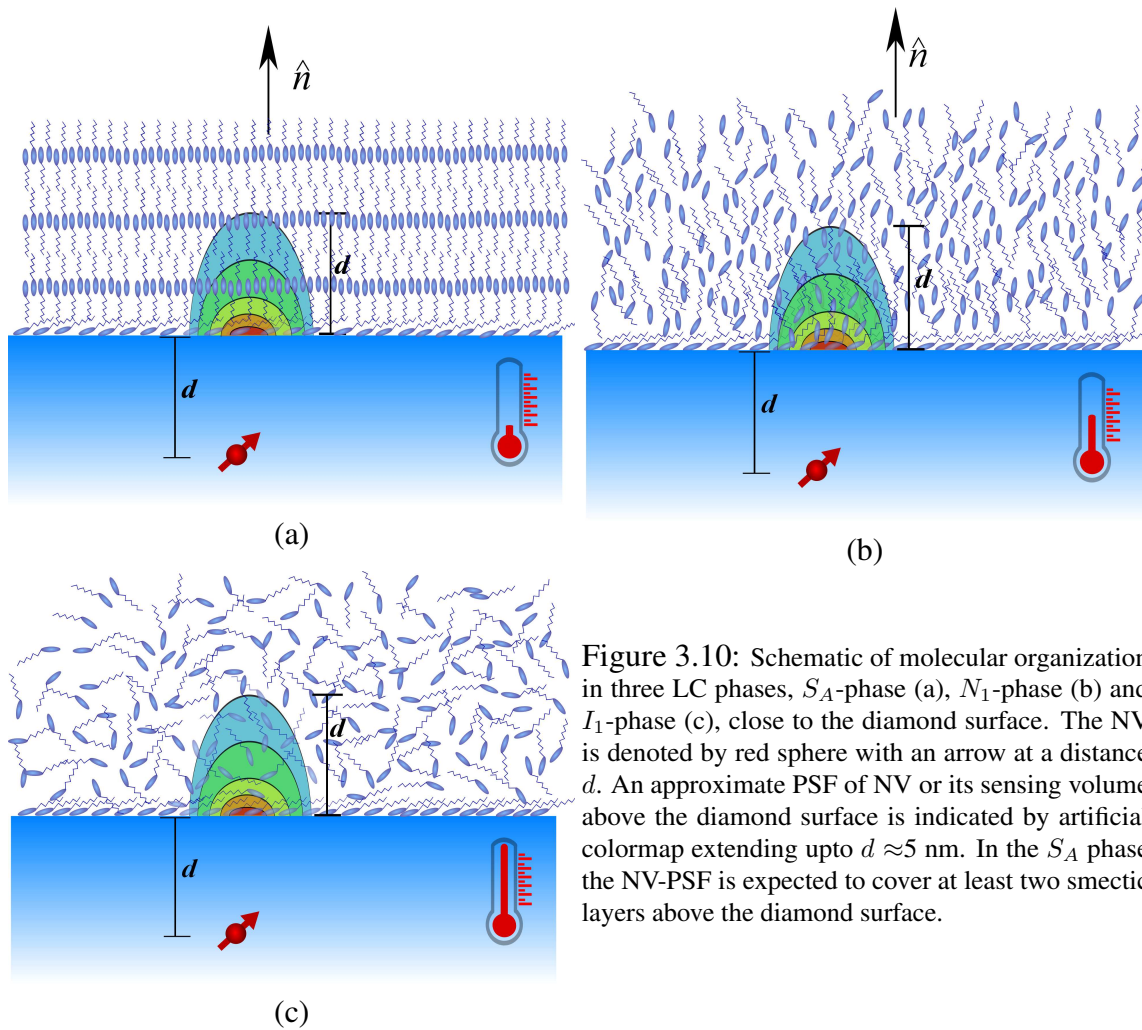
(a)

(b)

(c)

Figure 3.10: Schematic of molecular organization in three LC phases, S_A-phase (a), N_1-phase (b) and I_1-phase (c), close to the diamond surface. The NV is denoted by red sphere with an arrow at a distance d. An approximate PSF of NV or its sensing volume above the diamond surface is indicated by artificial colormap extending upto $d \approx 5$ nm. In the S_A phase the NV-PSF is expected to cover at least two smectic layers above the diamond surface.

the NV center's sensing volume is schematically shown. Due to hydrophilic nature of diamond surface, the polar head groups in the molecule get anchored to the surface while the hydrophobic alkyl chains points away from it. It is often mentioned in the literature that for most hydrophilic surfaces the first layer of 8CB molecules orient themselves at small angles from the surface (even flat in some cases) than being vertical due to the strong polar nature of their head groups. Studies on the wetting of macroscopic droplets of 8CB on silicon substrates have shown that this monolayer behaves like a prewetting film during the spreading of droplet [237, 238].

If the 8CB is in S_A phase, then a subsequent stacks of interdigitated bilayers with antiparallel dipole orientation will be present over the monolayer (with a possibility that the first bilayer being slightly tilted towards the underlying monolayer)as shown in the schematic (figure 3.10a). The length of the bilayers is about 3 nm or 1.4 times the single molecule length [231]. When the T is raised beyond the $S_A \rightarrow N$ transition point (34°C), the bilayers which form the S_A ordering will disappear and molecules will orient on an average along the surface normal (the director $\hat{n}$). The molecules now possess only orientation order and no positional order (figure 3.10b). When the material melts to fluidic I_1 phase this orientation order also disappears and the molecules orient in all possible directions (figure 3.10c), and show random motion driven by increased thermal energy.

But in both N_1 and I_1 phases, due to the strong anchoring to the surface the first monolayer on the diamond surface would essentially remain unchanged (figure 3.10b and 3.10c) as it is the case on most solid surfaces [238].

It is now well established in the literature that an NV center at a depth of d below the diamond surface can detect spins from approximately a half sphere of volume $\approx (d)^3$ above the diamond surface [30, 31]. The deeper the NV below the surface is, larger volumes it can detect above the diamond, though at the cost of reduced sensitivity [142]. It is estimate that in our samples, the NV centers were created at least 5 nm below the diamond surface for an implantation energy of 2.5 keV for 15N ions. This will result in the NV sensing volumes of about $(5nm)^3$ above the diamond surface. The approximate point spread function (PSF) of a shallow NV is indicated in the figure 3.10 In other words if the diameter of the half sphere sensing volume is d, then an NV at $d \sim$5 nm below the surface could detect spins at a height of 5 nm above the diamond. This means that as the 8CB molecule has a length of about 2 nm, the NV center can potentially sense at least a couple of smectic layers (by ignoring the thickness of the first monolayer) immediately above the diamond surface.

3.4.2 Diffusional broadening effects

Measurements of NMR signals from nanoscopic volumes show significant difference compared to those of conventional (bulk) NMR in terms of the Γ_p [39, 142, 239]. Precisely, in conventional NMR, compared to solids the liquid samples show narrower Γ_p due to the 'motional narrowing' effect. Contrastingly, in nanoscopic volumes the liquids show broadened Γ_p compared to solids due to 'diffusional broadening' effects [142, 146]. For example, Yang et al [39] observed a broadening of Γ_p of liquid water as compared to solid ice in nanoscopic volumes using NV sensors. The observable Γ_p is related to total phase acquisition time (τ) as,

$$\Gamma_p = \frac{2}{\gamma_h |\mathbf{B}|} \cdot \frac{1}{\tau} \tag{3.9}$$

where, $\frac{1}{\tau} = \frac{1}{T_D} + \frac{1}{T_{2p}^*} + \frac{1}{T_1^{NV}}$ with T_D-diffusion time scale of these spins in the nanoscopic volumes, T_{2p}^*-dephasing time of proton spins, T_1^{NV} is T_1 time of sensing NV and γ_h is the gyromagnetic ratio of proton spins.

As the NV-NMR relies on measuring the spin noise from statistically polarized spins (protons here), fast translational diffusion of molecules in and out of the detection volumes changes the distribution of statistically polarized spins. This results in the randomization of this polarization on fast time scale causing the broadening of Γ_p. Similar effects play a role in the LC experiments mentioned here. As the T is increased the material's properties change from more solid-like (S_A) to liquid-like phases. In the S_A phase due to the orientational and quasi-positional order (one dimensional layering) the molecules spend longer times within the NV-sensing volume. Hence the magnetization due to statistically polarized proton spins results in a narrower Γ_p of the signal. In the N_1 phase, the quasi-positional order disappears and the molecules posses only an orientational order along $\hat{n}$. Due to the increased mobility of the molecules in this phase the Γ_p increases. When the T is further raised to I_1 phase, the molecules experience self diffusion and fast tumbling driven by increased thermal energy as the material now exhibits no order. This will further broaden the Γ_p as explained above. The presence of immobile monolayer immediately next to the diamond surface can be correlated with similar thin layers observed in other studies of polymeric films on diamond surface [146]. As the NV sensing area in our case extends beyond this monolayer, the NV center's overall response is mainly dictated by the dynamics of the molecules outside this monolayer. The results mentioned in the figure 3.7 corroborate well with the explanation mentioned above. Majority of the NVs in the plot show line broadening with the increase in T.

As described by the equation 3.9, the achievable frequency resolution depends on the characteristic time scale, T_D of the molecules, among other factors [240]. Longer the T_D is narrower will be the Γ_p. The T_D is inversely proportional to the diffusion constant D_1 of the molecules and is of the order of microseconds for organic liquids, including the LC studied here. Owing to the anisotropy, the D_1 will have two components in LC : $D_\parallel$ and $D_\perp$, components parallel and perpendicular to director $\hat{n}$, respectively. D_1 measurements by NMR on bulk 8CB have reported that in going from S_A to I_1 phase the average diffusion constant $|D_1|$ doubles [241]. NV based sensing of other organic systems have indicated that NV signal could be sensitive to the doubling of diffusion constant [146]. It is expected that the LC phase transition studied here is indeed detectable with our method.

For some NVs (e.g., NV1, NV2, and NV6,) the Γ_p changes were small or remained almost constant. Some (NV4 and NV7) showed fluctuations in Γ_p although there is an overall increasing trend with T. Generally the solid-liquid interfacial boundaries are quite complex [216] and in some cases the solids induce order in the liquids in contact with them [242]. According to some reports in the literature, for liquid crystals on solid, the solid surface induces smectic-like ordering close to surface and this is even independent of T [237, 243]. However, the range of such ordering depends critically on the surface conditions [244] and strength of solid-LC interactions. Nevertheless, it is not clear if such effects really played any role in our case causing the Γ_p to remain almost constant as the

temperature was changed, which was observed in case of some NVs. It should also be noted that as the LC was heated through the diamond crystal itself, any layering close to the surface could melt fast facilitating the molecular dynamics to imprint their effects on the Γ_p.

Here we assumed that the LC undergoes transition at the transition temperatures mentioned for the case of bulk material. One can not completely rule out the possibility that for the LC material close to the surface transition temperature might be slightly different from the actual value. Indeed, such offsets in temperature have been observed in some thin films [245] and nanoconfined geometries [246]. Since the measurements were done not close to the transition point but almost in the middle (at 27° C and 37° C) of the phases, the observations can be considered as valid.

Also the amount of change in Γ_p across the phase transition is different for different NVs. This maybe because as there is a distribution of NV depths below the diamond surface, their interaction strength with the proton spins varies (due to $1/r^3$ dependence with distance). In addition, increased stochastic movement of the LC molecules in and out of the NV detection volume with increase in T could also contribute to change in the amount of increase in Γ_p.

3.4.3 Comparison with bulk NMR of 8CB LC

In the bulk 8CB, NMR measurements of proton spin relaxation rate ($(T_1^{LC})^{-1}$) across the phase transitions show a strong dependence on the γ_L [246]. For instance, at 3 MHz Larmor frequency, the T_1^{LC} rate across the phase transition ($S_A \rightarrow N \rightarrow I$) is almost negligible. Whereas at 10 kHz, the T_1^{LC} rate changes by as much as one order of magnitude and is abrupt at the transition point. This makes the three phase transitions become clearly detectable. It should be reminded that all our measurements were done at $\gamma_L \sim$ MHz. Obviously by performing the NV based nanoscale-NMR at small |B| of a few Gauss which results in the low γ_L(kHz range), one could expect to clearly detect the phase transitions. The T_1^{LC} times are in the range of tens of milliseconds for 8CB LC at such low γ_L. Naturally the spin coherence times (T$_2$) of the shallow NVs, which only last upto about 100 μs may not be sufficient to see the complete dynamics resulting from T_1^{LC} relaxation in these systems. Instead one could employ correlation protocols or other advanced NV-sensing methods which can probe for longer interrogation times to access the T_1^{LC} relaxation of protons.

Unlike the conventional liquids, LCs are characterized by many different kind of motions due to their anisotropic nature. There are anisotropic translational and rotational self diffusion of individual molecules with characterisitic timescales, τ_c of 10^{-8}-10^{-11} s. Also there are slower ($\tau_c \sim 10^{-4}$-10^{-8} s) collective molecular fluctuations known as order fluctuations of the director (OFD).

Consequently, the T_1^{LC} is driven by these motions [247]. NMR studies of the bulk LC materials show that the T_1^{LC} relaxation is a function of the Larmor frequency (γ_L) [246]. While at high γ_L (in MHz regime), the individual molecular dynamics dominate the T_1^{LC}, at low frequencies (in kHz regime) the collective fluctuations (OFD) dominate T_1^{LC}. It is found that in bulk the T_1^{LC} of 8CB LC shows different γ_L scaling depending on which phase it is in [248, 249]. S_A phase is shown to exhibit $T_1^{LC} \propto \gamma_L^1$ scaling and in N_1 phase

the scaling is $T_1^{LC} \propto \gamma_L^{1/2}$.

But, like ordinary liquids T_1^{LC} in isotropic phase shows no dependency on γ_L and remains constant. To check the response of the S_A phase to the Larmor frequency in the nano-NMR experiment, |B| was varied and the corresponding spin noise signal using XY experiment was measured. Figure 3.8b shows the result of the experiment where the spin noise Γ_p is plotted against the proton γ_L. As the T_1^{LC} varies linearly with γ_L in S_A one would expect the Γ_p to scale inversely with γ_L (because $\Gamma_p \propto 1/T_1^{LC}$). Counter intuitively however, it is observed that the Γ_p increased with γ_L (not linear though) in the nano-NMR. This is probably because, since the T_1^{LC} changes happen at much longer time scales (ms) than our measurement time scale (μs) and here we are probing only a small range of γ_L it is difficult to correlate present results with the bulk S_A behavior. Also, it may be possible that there is some other unknown process at play.

3.4.4   NV as a novel sensor to probe soft condensed matter systems

NV based sensing could potentially be used to address some fundamental problems in soft matter systems. For example, one of the long standing questions in two dimensional LC systems is the nature of the I_1 to N_1 phase transitions. It is proposed to be of first order, second order or even a Kosterlitz–Thouless type of continuous order [218, 250, 251]. But experimental confirmation of exact nature of this transition is not yet achieved, mainly due to lack of suitable probes to access the information. Also, dynamics of defects in LC are suggested to be similar to those of defects that appear in very large length scales in other systems such as cosmic strings [220], for example. There is still a dearth of suitable experimental tools that can be used to study defects kinetics over a wide length scale-from individual molecules to their collective self-assemblies. Perhaps, by combining single NV based methods (to sense at molecular level) with ensemble NV based schemes (to sense at μm level) one could bridge the gap between this wide length scale. Furthermore, NV based Nano-NMR methods could also be employed to study wetting and other interfacial phenomena in general. Precisely, the finer details about molecular interactions at the solid (diamond)-liquid boundaries could be addressed non-invasively through the recently developed NV based nano-NMR methods with high spectral resolution [150–152]. The ultralong interrogation time scales offered by these methods could also enable observing the subtle molecular signatures like chemical shifts and J-coupling in ultra low sample volumes. In soft matter systems T plays a decisive role in determining their properties. Thus NV centers offer combined advantages of highly sensitive magnetic and thermal field detection with nanoscale spatial resolution for studying interesting phenomena in such systems.

3.5   Chapter Conclusion

Temperature induced phase transitions in nanoscopic volumes of a standard liquid crystal material have been studied using an atom-sized sensor. The sensor is a single NV center situated at a few nm below the surface of the diamond and has a sensing volume of nearly $(5nm)^3$ above the diamond surface. The LC material in bulk shows three distinct phases starting from room temperature. By applying dynamical decoupling pulse sequences

on the NV center the spin noise spectra from the statistically polarized protons in the molecules have been obtained. The corresponding signal linewidths measured across the phase transitions over ten NV centers indicate the dependence of the spin noise signal on the different phases of the material. The broadening of the Γ_p with respect to temperature confirms that the material is undergoing transition to more fluidic state. This observation of line broadening is attributed to diffusional broadening effects specific to nanoscopic volumes. Since the NV center's detection volume extends upto a few molecular layers in the ordered phase of the LC material the change in the molecular dynamics across the phase transition definitely imprint their effect on the NV response which was observed as a change in the Γ_p. This observation is also supported by the fact that the expected changes in the diffusion constant, D_1 of the material across the phase transitions are within the reach of NV's sensitivity.

As the relaxation rates (T_1^{-1}) of the target spins in LC system become enhanced at lower Larmor frequencies, it is instructive to perform the nano-NMR measurements at smaller magnetic fields to more clearly see the signatures of the phase transitions in the nanoscopic volumes. In addition, using NV centers located deep (tens of nanometers) below the surface would not only make the signal narrower (because $T_D \propto \frac{d^2}{2 \cdot D_1}$) but also help probe larger length scales, possibly the correlation length scales of LC systems. Owing to the sensitivity of the NV to spin noise signals and temperature changes, it can be utilized as a dual mode nanoscale sensor for studying temperature related phenomena in soft matter. Particularly in LC systems, by precisely tuning the temperature using NV centers, one can explore interesting features across phase transitions.

Conclusions and Outlook

In summary, the works presented in the thesis portray studies related to advancing the applications of near surface NV centers for quantum sensing. In the recent years NV centers have emerged as a novel tool for sensing various physical quantities such as magnetic and electric fields, temperature, pressure etc. at the nanoscale. Basically, the studies mentioned in the thesis focused on detection of external magnetic field, both static and alternating in nature, using the single NV center. Towards realizing a novel and sensitive static field sensor, a hybrid system is demonstrated in the first part of results mentioned in the thesis. In the second part, NV center as a novel tool for sensing the alternating magnetic fields from a unique condensed matter system, is reported. By combing the magnetic sensing with temperature sensing, the second part demonstrates the ability of the NV centers for dual mode quantum sensing.

Starting with an artificial engineering of NV centers at shallow depths in high purity CVD diamond samples, Chapter One discussed the various magnetometry methods, with an emphasis on shallow NV center based sensing. Towards realizing a static field magnetometer with enhanced sensitivity, Chapter Two introduced a concept of hybrid sensing scheme combining a classical (GMI) sensor and a single NV center. NV centers as standalone sensors have static field sensitivity in the range of μT and is limited by their inhomogeneous dephasing rate, $1/T_2^*$. By integrating a single NV with the GMI microwire the resulting static field sensitivity is increased by over two orders of magnitude. The enhanced sensitivity results from the combination of many factors. First, the magnetometry protocol employed an echo based sensing, which takes advantage of the relatively long lived (nearly a factor of 10) coherence time rather than the T_2^* time. Second, compared to ordinary conductors, the GMI material is inherently sensitive to external static fields, this in turn encodes the magnetic information on the NV spin state, which can be readout optically. Third, by carefully coating the GMI microwire with a thin layer of gold, the GMI response can be enhanced compared to a bare (uncoated) wire.

The achieved sensitivity levels in the present work are still about three orders of magnitude lower than the potential sensitivity ($\sim$pT) of standalone GMI sensors based on conventional pick-up coils. Definitely there is a room for improvement to further boost the sensitivity. On the NV center part, the sensitivity depends on the NV readout fidelity and spin coherence time (T_2). One can enhance the readout efficiency, by employing more efficient schemes like-improved photon collection and advanced readout methods. Preparing better diamond surface will result in prolonged coherence times (T_2) and hence, helps improve the sensitivity. Perhaps, one can also implement advanced sensing modalities [150, 151] which are independent of NV relaxation times. On the GMI part, the material properties need to be further refined for more consistent and enhanced response. For

example, in the present work it was not fully possible to exploit the dependence of wire properties on Joule annealing. While the exact reason for this is not known, it is believed to be due to so-called aftereffect, which degrades the GMI response over time. This could be mitigated by properly tuning the magnetostriction values of the material. One can also experiment with coating of the wire with other metals (like copper) which have been already used [202] and study its influence on the hybrid sensor. One can also gain in the sensitivity by reducing the distance between NV center and GMI material. Currently, there are several advanced methods to fabricate GMI materials on any substrate [26]. By directly fabricating a GMI wire or thin film on the diamond chip itself, one can further gain in the sensitivity because, GMI material is located in close proximity with the NV center. Finally, as mentioned in the Chapter Two, the selected RF driving frequency depends on the $1/T_2$ of the NV and the Rabi frequency (Ω_R). The used frequency of hundreds of kHz is not necessarily the optimum frequency for the wire in which it shows maximum GMI response and hence, it is important to tune the driving frequency accordingly for the GMI-NV sensor.

As far as the application is concerned, highly sensitive static field sensor with minimal experimental resources could potentially be useful in bio-medical research. Essentially, the NV centers provide non-invasive sensing and replace the pick-up coil as the readout mechanisms.

In the second part of the thesis, an application of NV center to probe soft matter system was demonstrated for the first time. A single NV center is used as a sensor for detecting the spin noise signals from the external spins as well as measuring the temperature changes. This bimodal sensing nature of the NV centers is exploited to study phase transitions in the LC system. The NV based nano-NMR of the LC system indicated that LC phase transitions are indeed detectable and further improvements could enable us to more clearly observe the system dynamics in nanoscale across the transitions. Extending further, it would be interesting if one can arrive at the experimental observation of order parameter (S_1) as a function of temperature at the nanoscale using a nano-NMR method and compare with the corresponding S_1 variation in the bulk LC system.

While NV centers as quantum sensors have been widely employed to study hard condensed matter in the recent years, their application to explore soft condensed matter in general, is also expected to lead to some interesting observations. In this regard, the LC system used in the Chapter Three provided important advantage of accessing different ordered phases close to room temperature. As the sensing volumes of single NV centers is limited to nanoscopic range, they are excellent non-invasive probes for studying the lower dimensional systems. In the literature, techniques such as atomic force microscope (AFM) and X-ray are routinely used to characterize the mechanical, rheological and structural nature of soft matter. Nano-NMR spectroscopy can provide complementary information about the dynamics of the system at the nanoscale. Importantly, unlike the other conventional techniques (AFM, for example), the NV based sensing does not perturb the system. In addition, since the NV centers are also sensitive detectors for important physical quantities such as temperature, pressure etc, they constitute a multi-modal probe for investigating the soft matter systems.

In the present work, the thickness of the film in the μm range does not really constitute a true two dimensional (2D) system, but the probed length scales (using NV center) of

a few molecular layers can be roughly considered as a 2D layer. However, preparing a true 2D layer of ordered LC system provides exciting opportunities for studying them as model systems for understanding other complex phenomena [252]. For example, thin monomolecular layers of LC can be produced on the surface of the water and then transferred onto solid surfaces layer-by-layer using Langmuir-Blodgett (LB) method [253]. The LB films on solid surfaces are generally characterized using AFM. The LB films can also be prepared on the diamond surface containing proximal NV centers. Since the thickness of the LB films can be precisely controlled at the level of the individual molecular layers, this allows for nano-NMR studies on LC films, as a function of several parameters such as temperature, layer thickness etc. Since the lateral detection length scale (PSF) of the single NV extends upto roughly half its distance below the surface, to obtain signal from larger lateral distances on the diamond it is necessary use ensemble NV centers. The ensemble sensors also provide NMR spectroscopic information and it is possible to construct an optical MRI image [133] of the 2D film. This allows for obtaining the information about wider network of molecules in a 2D film. Another interesting area in which the NV based sensing could be useful is in the study of LCs in confined geometries, such as microfluidics. Studies on nematic LCs in microfluidics has gained significance due to its relevance to understand various phenomena related to lab-on-a-chip concept [254]. NV centers could be utilized to study local nematic order, molecular flow patterns and dynamics of topological defects in confined geometries constructed on the diamond. In the standard procedures for observing the flow patters, LCs are normally mixed with dye molecules and studied under fluorescence microscopes [254]. Instead, by using proximal NV centers, one can take advantage of spin contrast imaging (like in ref. [255]) with high spatio-temporal resolution for tracking individual molecules and map their flow patterns.

Bibliography

[1] Wiseman, H. M. and Milburn, G. J. *Quantum Measurement and Control*. Cambridge University Press, 2009.

[2] Giovannetti, V., Lloyd, S., and Maccone, L. "Quantum-Enhanced Measurements: Beating the Standard Quantum Limit". *Science* 306, 5700 (2004), pp. 1330–1336.

[3] Giovannetti, V., Lloyd, S., and Maccone, L. "Advances in quantum metrology". *Nat. Photonics* 5 (2011). Review Article, p. 222.

[4] Balasubramanian, G. et al. "Nanoscale imaging magnetometry with diamond spins under ambient conditions". *Nature* 455 (2008), p. 648.

[5] Degen, C. L. "Scanning magnetic field microscope with a diamond single-spin sensor". *Appl. Phys. Lett.* 92, 24 (2008), p. 243111.

[6] Taylor, J. M. et al. "High-sensitivity diamond magnetometer with nanoscale resolution". *Nat. Phys.* 4 (2008), p. 810.

[7] Schirhagl, R. et al. "Nitrogen-Vacancy Centers in Diamond: Nanoscale Sensors for Physics and Biology". *Annu. Rev. Phys. Chem.* 65, 1 (2014), pp. 83–105.

[8] Doherty, M. W. et al. "The nitrogen-vacancy colour centre in diamond". *Phys. Rep.* 528, 1 (2013), pp. 1–45.

[9] Degen, C. L., Reinhard, F., and Cappellaro, P. "Quantum sensing". *Rev. Mod. Phys.* 89 (2017), p. 035002.

[10] Liu, G.-Q. and Pan, X.-Y. "Quantum information processing with nitrogen–vacancy centers in diamond". *Chinese Phys. B* 27, 2 (2018), p. 020304.

[11] Maze, J. R. et al. "Nanoscale magnetic sensing with an individual electronic spin in diamond". *Nature* 455 (2008), pp. 644–648.

[12] Dolde, F. et al. "Electric-field sensing using single diamond spins". *Nat. Phys.* 7, 6 (2011), pp. 459–463.

[13] Neumann, P. et al. "High-Precision Nanoscale Temperature Sensing Using Single Defects in Diamond". *Nano Lett.* 13, 6 (2013), pp. 2738–2742.

[14] Doherty, M. W. et al. "Electronic Properties and Metrology Applications of the Diamond NV^- Center under Pressure". *Phys. Rev. Lett.* 112 (2014), p. 047601.

[15] Fu, C.-C. et al. "Characterization and application of single fluorescent nanodiamonds as cellular biomarkers". *Proc. Natl. Acad. Sci. U.S.A.* 104, 3 (2007), pp. 727–732.

[16] Balasubramanian, G. et al. "Ultralong spin coherence time in isotopically engineered diamond". *Nat. Mater* 8 (2009), p. 383.

[17] Dréau, A. et al. "Avoiding power broadening in optically detected magnetic resonance of single NV defects for enhanced dc magnetic field sensitivity". *Phys. Rev. B* 84 (2011), p. 195204.

[18] Barry, J. F. et al. "Sensitivity Optimization for NV-Diamond Magnetometry". http://arxiv.org/abs/1903.08176. 2019.

[19] Wolf, T. et al. "Subpicotesla Diamond Magnetometry". *Phys. Rev. X* 5, 4 (2015), p. 041001.

[20] Mizuochi, N. et al. "Coherence of single spins coupled to a nuclear spin bath of varying density". *Phys. Rev. B* 80 (2009), p. 041201.

[21] Loretz, M. et al. "Nanoscale nuclear magnetic resonance with a 1.9-nm-deep nitrogen-vacancy sensor". *Appl. Phys. Lett.* 104, 3 (2014), p. 033102.

[22] Abe, E. and Sasaki, K. "Tutorial: Magnetic resonance with nitrogen-vacancy centers in diamond—microwave engineering, materials science, and magnetometry". *J. Appl. Phys* 123, 16 (2018), p. 161101.

[23] Lenz, J. and Edelstein, S. "Magnetic sensors and their applications". *IEEE Sens. J* 6, 3 (2006), pp. 631–649.

[24] Mohri, K. et al. "Magneto-inductive element". *IEEE Trans. Magn.* 29, 2 (1993), pp. 1245–1248.

[25] Panina, L. V. and Mohri, K. "Magneto-impedance effect in amorphous wires". *Appl. Phys. Lett.* 65, 9 (1994), pp. 1189–1191.

[26] Peng, H.-X., Qin, F., and Phan, M.-H. *Ferromagnetic Microwire Composites:From Sensors to Microwave Applications*. 1st. Springer International Publishing, 2016.

[27] Mohri, K. et al. "Recent advances of amorphous wire CMOS IC magneto-impedance sensors: Innovative high-performance micromagnetic sensor chip". *J. Sensors* 2015 (2015).

[28] Staudacher, T. "Nuclear magnetic resonance spectroscopy on a nanoscopic sample volume". PhD thesis. University of Stuttgart, 2015.

[29] Slichter, C. P. *Principles of Magnetic Resonance*. Springer Berlin Heidelberg, 1996.

[30] Mamin, H. J. et al. "Nanoscale Nuclear Magnetic Resonance with a Nitrogen-Vacancy Spin Sensor". *Science* 339, 6119 (2013), pp. 557–560.

[31] Staudacher, T. et al. "Nuclear Magnetic Resonance Spectroscopy on a (5-Nanometer)3 Sample Volume". *Science* 339, 6119 (2013), pp. 561–563.

[32] Glover, P. and Mansfield, P. "Limits to magnetic resonance microscopy". *Rep. Progr. Phys.* 65, 10 (2002), pp. 1489–1511.

[33] Degen, C. L. et al. "Nanoscale magnetic resonance imaging". *Proc. Natl. Acad. Sci. U.S.A.* 106, 5 (2009), pp. 1313–1317.

[34] Shi, F. et al. "Single-protein spin resonance spectroscopy under ambient conditions". *Science* 347, 6226 (2015), pp. 1135–1138.

[35] Lovchinsky, I. et al. "Nuclear magnetic resonance detection and spectroscopy of single proteins using quantum logic". *Science* 351, 6275 (2016), pp. 836–841.

[36] Müller, C. et al. "Nuclear magnetic resonance spectroscopy with single spin sensitivity". *Nat. Commun.* 5 (2014), p. 4703.

[37] Sushkov, A. O. et al. "Magnetic Resonance Detection of Individual Proton Spins Using Quantum Reporters". *Phys. Rev. Lett.* 113, 19 (2014), p. 197601.

[38] Lovchinsky, I. et al. "Magnetic resonance spectroscopy of an atomically thin material using a single-spin qubit". *Science* 355, 6324 (2017), pp. 503–507.

[39] Yang, Z. et al. "Detection of magnetic dipolar coupling of water molecules at the nanoscale using quantum magnetometry". *Phys. Rev. B* 97, 20 (2018), p. 205438.

[40] Tetienne, J.-P. et al. "Quantum imaging of current flow in graphene". *Sci. Adv.* 3, 4 (2017).

[41] Kolkowitz, S. et al. "Probing Johnson noise and ballistic transport in normal metals with a single-spin qubit". *Science* 347, 6226 (2015), pp. 1129–1132.

[42] Sar, T. van der et al. "Nanometre-scale probing of spin waves using single electron spins". *Nat. Commun.* 6 (2015), p. 7886.

[43] Nagel, S. R. "Experimental soft-matter science". *Rev. Mod. Phys.* 89, 2 (2017), p. 025002.

[44] Gennes, P. de and Prost, J. *The Physics of Liquid Crystals*. English. 2nd ed. Clarendon Press, Oxford, 1993.

[45] Gennes, P. G. de. *Solid State Commun.* 88, 11-12 (1993), pp. 1039–1042.

[46] Rey, A. D. "Liquid crystal models of biological materials and processes". *Soft Matter* 6, 15 (2010), pp. 3402–3429.

[47] Graebner, J. E. *Thermal Conductivity of Diamond*. Ed. by Pan, L. S. and Kania, D. R. Boston, MA: Springer US, 1995, pp. 285–318.

[48] McSkimin, H. J. and Andreatch, P. "Elastic Moduli of Diamond as a Function of Pressure and Temperature". *J. Appl. Phys* 43, 7 (1972), pp. 2944–2948.

[49] Mochalin, V. N. et al. "The properties and applications of nanodiamonds". *Nat. Nanotechnol.* 7 (2011). Review Article, 11 EP -.

[50] Bundy, F. P. et al. "Man-Made Diamonds". *Nature* 176 (1955), p. 51.

[51] Hall, H. T. "Ultrahigh-Pressure Research". *Science* 128, 3322 (1958), pp. 445–449.

[52] Bundy, F. P. "The P, T phase and reaction diagram for elemental carbon, 1979". *J. Geophys. Res. Solid Earth.* 85, B12 (1980), pp. 6930–6936.

[53] Butler, J. E. et al. "Thin film diamond growth mechanisms". *Philos. Trans. A Math. Phys. Eng. Sci.* 342, 1664 (1993), pp. 209–224.

[54] Schwander, M. and Partes, K. "A review of diamond synthesis by CVD processes". *Diam. Relat. Mater.* 20, 9 (2011), pp. 1287–1301.

[55] Boudou, J.-P. et al. "High yield fabrication of fluorescent nanodiamonds". *Nanotechnology* 20, 23 (2009), p. 235602.

[56] Stacey, A. et al. "Controlled synthesis of high quality micro/nano-diamonds by microwave plasma chemical vapor deposition". *Diam. Relat. Mater.* 18, 1 (2009), pp. 51–55.

[57] Zaitsev, A. M. *Optical properties of diamond: a data handbook.* Springer Science & Business Media, 2013.

[58] Aharonovich, I. et al. "Diamond-based single-photon emitters". *Rep. Prog. Phys.* 74, 7 (2011), p. 076501.

[59] Jahnke, K. D. et al. "Electron–phonon processes of the silicon-vacancy centre in diamond". *New J. Phys.* 17, 4 (2015), p. 043011.

[60] Aharonovich, I., Englund, D., and Toth, M. "Solid-state single-photon emitters". *Nat. Photonics* 10 (2016). Review Article, 631 EP -.

[61] Schirhagl, R. et al. "Nitrogen-Vacancy Centers in Diamond: Nanoscale Sensors for Physics and Biology". *Annu. Rev. Phys. Chem.* 65, 1 (2014), pp. 83–105.

[62] Jelezko, F. and Wrachtrup, J. "Single defect centres in diamond: A review". *Phys. Status Solidi (a)* 203, 13 (2006), pp. 3207–3225.

[63] Acosta, V. M. "Optical Magnetometry with Nitrogen-Vacancy Centers in Diamond". PhD thesis. University of California, Berkeley, 2011.

[64] Loubser, J. H. N. and Wyk, J. A. van. "Electron spin resonance in the study of diamond". *Rep. Prog. Phys.* 41, 8 (1978), p. 1201.

[65] Maze, J. R. et al. "Properties of nitrogen-vacancy centers in diamond: the group theoretic approach". *New J. Phys.* 13, 2 (2011), p. 025025.

[66] Reddy, N., Manson, N., and Krausz, E. "Two-laser spectral hole burning in a colour centre in diamond". *J. Lumin.* 38, 1 (1987), pp. 46–47.

[67] Fuchs, G. D. et al. "Excited-State Spectroscopy Using Single Spin Manipulation in Diamond". *Phys. Rev. Lett.* 101 (11 2008), p. 117601.

[68] Mita, Y. "Change of absorption spectra in type-Ib diamond with heavy neutron irradiation". *Phys. Rev. B* 53 (17 1996), pp. 11360–11364.

[69] Felton, S. et al. "Electron paramagnetic resonance studies of the neutral nitrogen vacancy in diamond". *Phys. Rev. B* 77 (8 2008), p. 081201.

[70] Manson, N. and Harrison, J. "Photo-ionization of the nitrogen-vacancy center in diamond". *Diam. Relat. Mater.* 14, 10 (2005), pp. 1705–1710.

[71] Gaebel, T. et al. "Photochromism in single nitrogen-vacancy defect in diamond". *Appl. Phys. B* 82, 2 (2006), pp. 243–246.

[72] Kun, H., Avril, R., and Francis, M. N. "Theory of light absorption and non-radiative transitions in F-centres". *Proceedings of the Royal Society of London. Series A. Mathematical and Physical Sciences* 204, 1078 (1950), pp. 406–423.

[73] Doherty, M. W. et al. "The negatively charged nitrogen-vacancy centre in diamond: The electronic solution". *New J. Phys.* 13 (2011).

[74] Nizovtsev, A. et al. "NV centers in diamond: spin-selective photokinetics, optical ground-state spin alignment and hole burning". *Physica B: Condens. Matter* 340-342 (2003). Proceedings of the 22nd International Conference on Defects in Semiconductors, pp. 106–110.

[75] Harrison, J., Sellars, M. J., and Manson, N. B. "Optical spin polarisation of the N-V centre in diamond". *J. Lumin.* 107, 1-4 (2004), pp. 245–248.

[76] Manson, N. B., Harrison, J. P., and Sellars, M. J. "Nitrogen-vacancy center in diamond: Model of the electronic structure and associated dynamics". *Phys. Rev. B - Condens. Matter Mater. Phys.* 74, 10 (2006), pp. 1–11.

[77] Delaney, P., Greer, J. C., and Larsson, J. A. "Spin-polarization mechanisms of the nitrogen-vacancy center in diamond". *Nano Lett.* 10, 2 (2010), pp. 610–614.

[78] Robledo, L. et al. "Spin dynamics in the optical cycle of single nitrogen-vacancy centres in diamond". *New J. Phys.* 13 (2011).

[79] Thiering, G. and Gali, A. "Theory of the optical spin-polarization loop of the nitrogen-vacancy center in diamond". *Phys. Rev. B* 98, 8 (2018), pp. 1–12.

[80] Jelezko, F. et al. "Observation of Coherent Oscillations in a Single Electron Spin". *Phys. Rev. Lett.* 92, 7 (2004), p. 076401.

[81] Jelezko, F. et al. "Observation of Coherent Oscillation of a Single Nuclear Spin and Realization of a Two-Qubit Conditional Quantum Gate". *Phys. Rev. Lett.* 93, 13 (2004), p. 130501.

[82] Harrison, J., Sellars, M. J., and Manson, N. B. "Measurement of the optically induced spin polarisation of N-V centres in diamond". *Diam. Relat. Mater.* 15, 4-8 (2006), pp. 586–588.

[83] Acosta, V. M. et al. "Temperature Dependence of the Nitrogen-Vacancy Magnetic Resonance in Diamond". *Phys. Rev. Lett.* 104, 7 (2010), p. 070801.

[84] Weil, J. A. and Bolton, J. R. *Electron Paramagnetic Resonance: Elementary Theory and Practical Applications*. Wiley, 2007.

[85] Epstein, R. J. et al. "Anisotropic interactions of a single spin and dark-spin spectroscopy in diamond". *Nat. Phys.* 1, 2 (2005), pp. 94–98.

[86] Jacques, V. et al. "Dynamic polarization of single nuclear spins by optical pumping of nitrogen-vacancy color centers in diamond at room temperature". *Phys. Rev. Lett.* 102, 5 (2009), pp. 7–10.

[87] Jeong, K. et al. "Understanding the Magnetic Resonance Spectrum of Nitrogen Vacancy Centers in an Ensemble of Randomly Oriented Nanodiamonds". *J. Phys. Chem. C* 121, 38 (2017), pp. 21057–21061.

[88] He, X. F., Manson, N. B., and Fisk, P. T. "Paramagnetic resonance of photoexcited N-V defects in diamond. II. Hyperfine interaction with the N14 nucleus". *Phys. Rev. B* 47, 14 (1993), pp. 8816–8822.

[89] Steiner, M. et al. "Universal enhancement of the optical readout fidelity of single electron spins at nitrogen-vacancy centers in diamond". *Phys. Rev. B* 81, 3 (2010), p. 035205.

[90] Rabeau, J. R. et al. "Implantation of labelled single nitrogen vacancy centers in diamond using N15". *Appl. Phys. Lett.* 88, 2 (2006), p. 023113.

[91] Dréau, A. et al. "High-resolution spectroscopy of single NV defects coupled with nearby ^{13}C nuclear spins in diamond". *Phys. Rev. B* 85, 13 (2012), p. 134107.

[92] Taminiau, T. H. et al. "Detection and Control of Individual Nuclear Spins Using a Weakly Coupled Electron Spin". *Phys. Rev. Lett.* 109, 13 (2012), p. 137602.

[93] Felton, S. et al. "Hyperfine interaction in the ground state of the negatively charged nitrogen vacancy center in diamond". *Phys. Rev. B* 79, 7 (2009), p. 075203.

[94] Donley, E. A. et al. "Double-pass acousto-optic modulator system". *Rev. Sci. Instrum.* 76, 6 (2005), pp. 3–8.

[95] Binder, J. M. et al. "Qudi: A modular python suite for experiment control and data processing". *SoftwareX* 6 (2017), pp. 85–90.

[96] Webb, R. H. "Confocal optical microscopy". *Rep. Prog. Phys.* 59, 3 (1996), pp. 427–471.

[97] Hell, S. W. "Far-Field Optical Nanoscopy". *Science* 316, 5828 (2007), pp. 1153–1158.

[98] Brown, R. H. and Twiss, R. Q. "Correlation between Photons in two Coherent Beams of Light". *Nature* 177, 4497 (1956), pp. 27–29.

[99] Ohno, K. et al. "Engineering shallow spins in diamond with nitrogen delta-doping". *Appl. Phys. Lett.* 101, 8 (2012), p. 082413.

[100] Myers, B. A. et al. "Probing surface noise with depth-calibrated spins in diamond". *Phys. Rev. Lett.* 113, 2 (2014), pp. 1–6.

[101] Meijer, J. et al. "Generation of single color centers by focused nitrogen implantation". *Appl. Phys. Lett.* 87, 26 (2005), p. 261909.

[102] Pezzagna, S. et al. "Creation efficiency of nitrogen-vacancy centres in diamond". *New J. Phys.* 12, 6 (2010), p. 065017.

[103] Haque, A. and Sumaiya, S. "An Overview on the Formation and Processing of Nitrogen-Vacancy Photonic Centers in Diamond by Ion Implantation". *J. Manuf. Mater. Process* 1, 1 (2017).

[104] Dam, S. B. van et al. "Optical coherence of diamond nitrogen-vacancy centers formed by ion implantation and annealing". *Phys. Rev. B* 99, 16 (2019), p. 161203.

[105] Davies, G. et al. "Vacancy-related centers in diamond". *Phys. Rev. B* 46, 20 (1992), pp. 13157–13170.

[106] Ziegler, J. F. *SRIM - The Stopping and Range of Ions in Matter.* http://www.srim.org/.

[107] Gruber, A. et al. "Scanning Confocal Optical Microscopy and Magnetic Resonance on Single Defect Centers". *Science* 276, 5321 (1997), pp. 2012–2014.

[108] Maertz, B. J. et al. "Vector magnetic field microscopy using nitrogen vacancy centers in diamond". *Appl. Phys. Lett.* 96, 9 (2010), p. 092504.

[109] Steinert, S. et al. "High sensitivity magnetic imaging using an array of spins in diamond". *Rev. Sci. Instrum* 81, 4 (2010), p. 043705.

[110] Bloch, F. "Nuclear Induction". *Phys. Rev.* 70 (1946), pp. 460–474.

[111] Jarmola, A. et al. "Temperature- and Magnetic-Field-Dependent Longitudinal Spin Relaxation in Nitrogen-Vacancy Ensembles in Diamond". *Phys. Rev. Lett.* 108, 19 (2012), p. 197601.

[112] Norambuena, A. et al. "Spin-lattice relaxation of individual solid-state spins". *Phys. Rev. B* 97 (2018), p. 094304.

[113] Redman, D. A. et al. "Spin dynamics and electronic states of N-V centers in diamond by EPR and four-wave-mixing spectroscopy". *Phys. Rev. Lett.* 67, 24 (1991), pp. 3420–3423.

[114] Maurer, P. C. et al. "Room-Temperature Quantum Bit Memory Exceeding One Second". *Science* 336, 6086 (2012), p. 1283.

[115] Hanson, R., Gywat, O., and Awschalom, D. D. "Room-temperature manipulation and decoherence of a single spin in diamond". *Phys. Rev. B* 74, 16 (2006), p. 161203.

[116] Lange, G. de et al. "Universal Dynamical Decoupling of a Single Solid-State Spin from a Spin Bath". *Science* 330, 6000 (2010), pp. 60–63.

[117] Naydenov, B. et al. "Dynamical decoupling of a single-electron spin at room temperature". *Phys. Rev. B* 83, 8 (2011), p. 081201.

[118] Bar-Gill, N. et al. "Suppression of spin-bath dynamics for improved coherence of multi-spin-qubit systems". *Nat. Commun.* 3 (2012), p. 858.

[119] Bar-Gill, N. et al. "Solid-state electronic spin coherence time approaching one second". *Nat. Commun.* 4 (2013). Article, p. 1743.

[120] Maze, J. R. et al. "Free induction decay of single spins in diamond". *New J. Phys.* 14, 10 (2012), p. 103041.

[121] Childress, L. et al. "Coherent Dynamics of Coupled Electron and Nuclear Spin Qubits in Diamond". *Science* 314, 5797 (2006), pp. 281–285.

[122] Ofori-Okai, B. K. et al. "Spin properties of very shallow nitrogen vacancy defects in diamond". *Phys. Rev. B* 86 (2012), p. 081406.

[123] Rosskopf, T. et al. "Investigation of Surface Magnetic Noise by Shallow Spins in Diamond". *Phys. Rev. Lett.* 112, 14 (2014), p. 147602.

[124] Romach, Y. et al. "Spectroscopy of Surface-Induced Noise Using Shallow Spins in Diamond". *Phys. Rev. Lett.* 114 (2015), p. 017601.

[125] Vandersypen, L. M. K. and Chuang, I. L. "NMR techniques for quantum control and computation". *Rev. Mod. Phys.* 76, 4 (2005), pp. 1037–1069.

[126] Cywiński, Ł. et al. "How to enhance dephasing time in superconducting qubits". *Phys. Rev. B* 77, 17 (2008), p. 174509.

[127] Carr, H. Y. and Purcell, E. M. "Effects of Diffusion on Free Precession in Nuclear Magnetic Resonance Experiments". *Phys. Rev.* 94, 3 (1954), pp. 630–638.

[128]   Meiboom, S. and Gill, D. "Modified Spin-Echo Method for Measuring Nuclear Relaxation Times". *Rev. Sci. Instrum* 29, 8 (1958), pp. 688–691.

[129]   Ryan, C. A., Hodges, J. S., and Cory, D. G. "Robust Decoupling Techniques to Extend Quantum Coherence in Diamond". *Phys. Rev. Lett.* 105, 20 (2010), p. 200402.

[130]   Gullion, T., Baker, D. B., and Conradi, M. S. "New, compensated Carr-Purcell sequences". *J. Magn. Reson.* 89, 3 (1990), pp. 479–484.

[131]   Rugar, D. et al. "Proton magnetic resonance imaging using a nitrogen-vacancy spin sensor". *Nat. Nanotechnol.* 10 (2014), p. 120.

[132]   Häberle, T. et al. "Nanoscale nuclear magnetic imaging with chemical contrast". *Nat. Nanotechnol.* 10 (2015), p. 125.

[133]   DeVience, S. J. et al. "Nanoscale NMR spectroscopy and imaging of multiple nuclear species". *Nat. Nanotechnol.* 10 (2015), p. 129.

[134]   Loretz, M. et al. "Spurious Harmonic Response of Multipulse Quantum Sensing Sequences". *Phys. Rev. X* 5 (2015), p. 021009.

[135]   Degen, C. L. et al. "Role of Spin Noise in the Detection of Nanoscale Ensembles of Nuclear Spins". *Phys. Rev. Lett.* 99, 25 (2007), p. 250601.

[136]   Mamin, H. J. et al. "Magnetic resonance force microscopy of nuclear spins: Detection and manipulation of statistical polarization". *Phys. Rev. B* 72, 2 (2005), p. 024413.

[137]   Mamin, H. J. et al. "Nuclear magnetic resonance imaging with 90-nm resolution". *Nat. Nanotechnol.* 2 (2007), p. 301.

[138]   Rondin, L. et al. "Magnetometry with nitrogen-vacancy defects in diamond". *Rep. Prog. Phys.* 77, 5 (2014), p. 056503.

[139]   Hauf, M. V. et al. "Chemical control of the charge state of nitrogen-vacancy centers in diamond". *Phys. Rev. B* 83, 8 (2011), p. 081304.

[140]   Myers, B. A., Ariyaratne, A., and Jayich, A. C. B. "Double-Quantum Spin-Relaxation Limits to Coherence of Near-Surface Nitrogen-Vacancy Centers". *Phys. Rev. Lett.* 118 (2017), p. 197201.

[141]   Kim, M. et al. "Decoherence of Near-Surface Nitrogen-Vacancy Centers Due to Electric Field Noise". *Phys. Rev. Lett.* 115, 8 (2015), p. 087602.

[142]   Aslam, N. et al. "Nanoscale nuclear magnetic resonance with chemical resolution". *Science* 357, 6346 (2017), pp. 67–71.

[143]   Fu, R. R. et al. "Solar nebula magnetic fields recorded in the Semarkona meteorite". *Science* 346, 6213 (2014), pp. 1089–1092.

[144]   Maletinsky, P. et al. "A robust scanning diamond sensor for nanoscale imaging with single nitrogen-vacancy centres". *Nat. Nanotechnol.* 7 (2012), p. 320.

[145]   Lazariev, A. and Balasubramanian, G. "A nitrogen-vacancy spin based molecular structure microscope using multiplexed projection reconstruction". *Sci. Rep.* 5 (2015), p. 14130.

[146] Staudacher, T. et al. "Probing molecular dynamics at the nanoscale via an individual paramagnetic centre". *Nat. Commun.* 6 (2015), p. 8527.

[147] Loretz, M., Rosskopf, T., and Degen, C. L. "Radio-Frequency Magnetometry Using a Single Electron Spin". *Phys. Rev. Lett.* 110, 1 (2013), p. 017602.

[148] London, P. et al. "Detecting and Polarizing Nuclear Spins with Double Resonance on a Single Electron Spin". *Phys. Rev. Lett.* 111, 6 (2013), p. 067601.

[149] Lazariev, A. et al. "Dynamical sensitivity control of a single-spin quantum sensor". *Sci. Rep.* 7, 1 (2017), p. 6586.

[150] Schmitt, S. et al. "Submillihertz magnetic spectroscopy performed with a nanoscale quantum sensor". *Science* 356, 6340 (2017), pp. 832–837.

[151] Boss, J. M. et al. "Quantum sensing with arbitrary frequency resolution". *Science* 356, 6340 (2017), pp. 837–840.

[152] Glenn, D. R. et al. "High-resolution magnetic resonance spectroscopy using a solid-state spin sensor". *Nature* 555 (2018), p. 351.

[153] Ripka, P. and Janosek, M. "Advances in Magnetic Field Sensors". *IEEE Sens. J* 10, 6 (2010), pp. 1108–1116.

[154] DeMille, D., Doyle, J. M., and Sushkov, A. O. "Probing the frontiers of particle physics with tabletop-scale experiments". *Science* 357, 6355 (2017), pp. 990–994.

[155] Budker, D. et al. "Proposal for a Cosmic Axion Spin Precession Experiment (CASPEr)". *Phys. Rev. X* 4, 2 (2014), p. 021030.

[156] Hämäläinen, M. et al. "Magnetoencephalography—theory, instrumentation, and applications to noninvasive studies of the working human brain". *Rev. Mod. Phys.* 65, 2 (1993), pp. 413–497.

[157] Phan, M.-H. and Peng, H.-X. "Giant magnetoimpedance materials: Fundamentals and applications". *Prog. Mater. Sci.* 53, 2 (2008), pp. 323–420.

[158] Kitching, J. "Chip-scale atomic devices". *Appl. Phys. Rev.* 5, 3 (2018), p. 031302.

[159] Harrison, E. P. et al. "The electrical properties of high permeability wires carrying alternating current". *Proc. R. Soc. Lond. A Math. Phys. Sci.* 157, 891 (1936), pp. 451–479.

[160] Kawashima, K. et al. "Magneto-inductive effect in tension-annealed amorphous wires and MI sensors". *IEEE Trans. Magn.* 29, 6 (1993), pp. 3168–3170.

[161] Panina, L. V. et al. "Giant magneto-impedance in Co-rich amorphous wires and films". *IEEE Trans. Magn.* 31, 2 (1995), pp. 1249–1260.

[162] Kraus, L. "GMI modeling and material optimization". *Sens. Actuators A Phys.* 106, 1-3 (2003), pp. 187–194.

[163] Ciureanu, P. et al. "Physical models of magnetoimpedance". *J. Appl. Phys* 102, 7 (2007), p. 073908.

[164] Beach, R. S. and Berkowitz, A. E. "Sensitive field- and frequency-dependent impedance spectra of amorphous FeCoSiB wire and ribbon (invited)". *J. Appl. Phys* 76, 10 (1994), pp. 6209–6213.

[165] Machado, F. L. A. et al. "Giant ac magnetoresistance in the soft ferromagnet Co70.4Fe4.6Si15B10". *J. Appl. Phys* 75, 10 (1994), pp. 6563–6565.

[166] Beach, R. S. and Berkowitz, A. E. "Sensitive field- and frequency-dependent impedance spectra of amorphous FeCoSiB wire and ribbon (invited)". *J. Appl. Phys* 76, 10 (1994), pp. 6209–6213.

[167] Landau, L. D. and Lifshitz, E. M. *Electrodynamics of continuous media*. Pergamon Press, Oxford, 1975.

[168] Rao, K. V., Humphrey, F. B., and Costa-Krämer, J. L. "Very large magneto-impedance in amorphous soft ferromagnetic wires (invited)". *J. Appl. Phys* 76, 10 (1994), pp. 6204–6208.

[169] Knobel, M., Gómez-Polo, C., and Vázquez, M. "Evaluation of the linear magnetostriction in amorphous wires using the giant magneto-impedance effect". *J. Magn. Magn. Mater.* 160 (1996), pp. 243–244.

[170] Knobel, M. and Pirota, K. R. "Giant magnetoimpedance: Concepts and recent progress". *J. Magn. Magn. Mater.* 242-245, PART I (2002), pp. 33–40.

[171] Mohri, K. et al. "Magneto Inductive effect(MI effect) in amorphous wires". *IEEE Trans. Magn.* 28 (1992), pp. 3150–3152.

[172] Kraus, L. "Theory of giant magneto-impedance in the planar conductor with uniaxial magnetic anisotropy". *J. Magn. Magn. Mater.* 195 (1999), pp. 764–778.

[173] Takajo, M., Yamasaki, J., and Humphrey, F. B. "Domain observations of Fe and Co based amorphous wires". *IEEE Trans. Magn.* 29, 6 (1993), pp. 3484–3486.

[174] Chen, D.-X. et al. "Magnetoimpedance of metallic ferromagnetic wires". *Phys. Rev. B* 57, 17 (1998), pp. 10699–10704.

[175] Machado, F. L. A. and Rezende, S. M. "A theoretical model for the giant magnetoimpedance in ribbons of amorphous soft-ferromagnetic alloys". *J. Appl. Phys* 79, 8 (1996), pp. 6558–6560.

[176] Atkinson, D. and Squire, P. T. "Experimental and phenomenological investigation of the effect of stress on magneto-impedance in amorphous alloys". *IEEE Trans. Magn.* 33, 5 (1997), pp. 3364–3366.

[177] Pirota, K. R. et al. "Influence of induced anisotropy and magnetostriction on the giant magnetoimpedance effect and its aftereffect in soft magnetic amorphous ribbons". *J. Magn. Magn. Mater.* 202, 2 (1999), pp. 431–444.

[178] Yelon, A. et al. "Calculations of giant magnetoimpedance and of ferromagnetic resonance response are rigorously equivalent". *Appl. Phys. Lett.* 69, 20 (1996), pp. 3084–3085.

[179] Britel, M. R. et al. "Magnetoimpedance measurements of ferromagnetic resonance and antiresonance". *Appl. Phys. Lett.* 77, 17 (2000), pp. 2737–2739.

[180] Ménard, D. et al. "Giant magnetoimpedance in a cylindrical magnetic conductor". *J. Appl. Phys* 84, 5 (1998), pp. 2805–2814.

[181] Machado, F. L. A. et al. "Surface Magnetoimpedance Measurements in Soft-Ferromagnetic Materials". *Phys. Status Solidi (a)* 173, 1 (1999), pp. 135–144.

[182] Wang, H. et al. "Fabrication and Characterization of Melt-Extracted Co-Based Amorphous Wires". *Metall. Mater. Trans.A* 42, 4 (2011), pp. 1103–1108.

[183] Wang, H. et al. "Relating residual stress and microstructure to mechanical and giant magneto-impedance properties in cold-drawn Co-based amorphous microwires". *Acta Mater.* 60, 15 (2012), pp. 5425–5436.

[184] Jiang, S. D. et al. "Relating surface roughness and magnetic domain structure to giant magneto-impedance of Co-rich melt-extracted microwires". *Sci. Rep.* 7 (2017), p. 46253.

[185] Velázquez, J. et al. "Magnetoelastic anisotropy in amorphous wires due to quenching". *J. Appl. Phys* 70, 10 (1991), pp. 6525–6527.

[186] Vázquez, M. and Hernando, A. "A soft magnetic wire for sensor applications". *J. Phys. D Appl. Phys.* 29, 4 (1996), pp. 939–949.

[187] Reininger, T. et al. "Magnetic domain observation in amorphous wires". *J. Appl. Phys* 73, 10 (1993), pp. 5357–5359.

[188] Domínguez, L. et al. "Circumferential magnetization processes in CoFeBSi wires". *J. Appl. Phys* 79, 8 (1996), pp. 6539–6541.

[189] Vázquez, M., Li, Y.-F., and Chen, D.-X. "Influence of the sample length and profile of the magnetoimpedance effect in FeCrSiBCuNb ultrasoft magnetic wires". *J. Appl. Phys* 91, 10 (2002), pp. 6539–6544.

[190] Phan, M. H. et al. "Large enhancement of GMI effect in polymer composites containing Co-based ferromagnetic microwires". *J. Magn. Magn. Mater.* 316 (2007), e253–e256.

[191] Hu, J. et al. "Diameter dependence of the giant magnetoimpedance in hard-drawn CoFeSiB amorphous wires". *J. Appl. Phys* 91, 10 (2002), pp. 7418–7420.

[192] Jantaratana, P. and Sirisathitkul, C. "Effects of thickness and heat treatments on giant magnetoimpedance of electrodeposited cobalt on silver wires". *IEEE Trans. Magn.* 42, 3 (2006), pp. 358–362.

[193] Melo, L. G. C. et al. "Optimization of the magnetic noise and sensitivity of giant magnetoimpedance sensors". *J. Appl. Phys* 103, 3 (2008), p. 033903.

[194] Ménard, D. et al. "Progress towards the optimization of the signal-to-noise ratio in giant magnetoimpedance sensors". *Sens. Actuators A Phys.* 129 (2006), pp. 6–9.

[195] Ding, L. et al. "Equivalent Magnetic Noise Limit of Low-Cost GMI Magnetometer". *IEEE Sens. J* 9, 2 (2009), pp. 159–168.

[196] Dufay, B. et al. "Impact of Electronic Conditioning on the Noise Performance of a Two-Port Network Giant MagnetoImpedance Magnetometer". *IEEE Sens. J* 11, 6 (2011), pp. 1317–1324.

[197] Malatek, M. et al. "Improvement of the off-diagonal magnetoimpedance sensor white noise". *Sens. Actuators A Phys.* 204 (2013), pp. 20–24.

[198] Dufay, B. et al. "Improved GMI Sensors Using Strongly-Coupled Thin Pick-Up Coils". *Sensor Lett.* 7, 3 (2009), pp. 334–338.

[199] Barry, J. F. et al. "Optical magnetic detection of single-neuron action potentials using quantum defects in diamond". *Proc. Natl. Acad. Sci. U.S.A.* 113, 49 (2016), pp. 14133–14138.

[200] Shen, H. et al. "Optimization of mechanical and giant magneto-impedance (GMI) properties of melt-extracted Co-rich amorphous microwires". *Phys. Status Solidi (a)* 211, 7 (2014), pp. 1668–1673.

[201] Liu, J.-S. et al. "Experimental study on the effect of wire bonding by Cu electroplating on GMI stability of Co-based amorphous wires". *Phys. Status Solidi (a)* 208, 3 (2011), pp. 530–534.

[202] Liu, J. et al. "Composite electroplating to enhance the GMI output stability of melt-extracted wires". *Mater. Des.* 96 (2016), pp. 251–256.

[203] Kanani, N. *Electroplating*. Oxford: Elsevier, 2004.

[204] Chen, D.-M. et al. "Correlation of magnetic domains, microstructure and GMI effect of Joule-annealed melt-extracted Co68.15Fe4.35Si12.25B13.75Nb1Cu0.5 microwires for double functional sensors". *Phys. Status Solidi (a)* 210, 11 (2013), pp. 2515–2520.

[205] Allia, P. et al. "Joule-heating effects in the amorphous $Fe_{40}Ni_{40}B_{20}$ alloy". *Phys. Rev. B* 47, 6 (1993), pp. 3118–3125.

[206] Thiabgoh, O. et al. "Real-time monitoring of position and motion of a non-stationary object with a highly sensitive magnetic impedance sensor". *J. Sci. Adv. Mater. Dev.* 3, 1 (2018), pp. 122–128.

[207] Mamin, H. J. et al. "Multipulse double-quantum magnetometry with near-surface nitrogen-vacancy centers". *Phys. Rev. Lett.* 113, 3 (2014), p. 030803.

[208] Momenzadeh, S. A. et al. "Nanoengineered Diamond Waveguide as a Robust Bright Platform for Nanomagnetometry Using Shallow Nitrogen Vacancy Centers". *Nano Lett.* 15, 1 (2015), pp. 165–169.

[209] Li, L. et al. "Efficient Photon Collection from a Nitrogen Vacancy Center in a Circular Bullseye Grating". *Nano Lett.* 15, 3 (2015), pp. 1493–1497.

[210] Shields, B. J. et al. "Efficient Readout of a Single Spin State in Diamond via Spin-to-Charge Conversion". *Phys. Rev. Lett.* 114, 13 (2015), p. 136402.

[211] Neumann, P. et al. "Single-Shot Readout of a Single Nuclear Spin". *Science* 329, 5991 (2010), pp. 542–544.

[212] Chiriac, H. et al. "Magnetic GMI sensor for detection of biomolecules". *J. Magn. Magn. Mater.* 293, 1 (2005), pp. 671–676.

[213] Körber, R. et al. "SQUIDs in biomagnetism: a roadmap towards improved healthcare". *Supercond. Sci. Technol.* 29, 11 (2016), p. 113001.

[214] Uchiyama, T., Mohri, K., and Nakayama, S. "Measurement of Spontaneous Oscillatory Magnetic Field of Guinea-Pig Smooth Muscle Preparation Using Pico-Tesla Resolution Amorphous Wire Magneto-Impedance Sensor". *IEEE Trans. Magn.* 47, 10 (2011), pp. 3070–3073.

[215] Chaikin, P. and Lubensky, T. *Principles of Condensed Matter Physics*. Cambridge University Press, 2000.

[216] Israelachvili, J. N. *Intermolecular and surface forces*. English. 2nd ed. Academic Press, London, 1991.

[217] Stanley, H. E. *Introduction to Phase Transitions and Critical Phenomena*. Oxford University Press, 1971.

[218] Kosterlitz, J. M. and Thouless, D. J. "Ordering, metastability and phase transitions in two-dimensional systems". *J. Phys. C : Solid State Phys.* 6, 7 (1973), pp. 1181–1203.

[219] L.D.Landau and E.M.Lifshitz. *Statistical Physics*. English. 3rd ed. Vol. 5. Pergamon Press, Oxford, 1980.

[220] Chuang, I. et al. "Cosmology in the laboratory: Defect dynamics in liquid crystals". *Science* 251, 4999 (1991), pp. 1336–1342.

[221] Zurek, W. H. "Cosmological experiments in condensed matter systems". *Phys. Rep.* 276 (1996), pp. 177–221.

[222] Cowin, S. C. "Do liquid crystal-like flow processes occur in the supramolecular assembly of biological tissues?" *J. Nonnewton. Fluid Mech.* 119, 1-3 (2004), pp. 155–162.

[223] Olesiak-Banska, J. et al. "Liquid crystal phases of DNA: Evaluation of DNA organization by two-photon fluorescence microscopy and polarization analysis". *Biopolymers* 95, 6 (2011), pp. 365–375.

[224] Gennes, P. G. de. "An analogy between superconductors and smectics A". *Solid State Commun.* 10, 9 (1972), pp. 753–756.

[225] Kléman, M. *Advances in Liquid Crystals*. Vol. 1. Elsevier, 1975. Chap. Defects in Liquid Crystals, pp. 267–311.

[226] Maier, W. and Saupe, A. Z. *Z. Naturforsch.,* 13a (1959), pp. 564–570.

[227] Maier, W. and Saupe, A. Z. *Z. Naturforsch.,* 14a (1959), pp. 882–900.

[228] Maier, W. and Saupe, A. Z. *Z. Naturforsch.,* 15a (1960), pp. 287–292.

[229] Gramsbergen, E. F., Jeu, W. H. de, and Als-Nielsen, J. "Antiferroelectric surface layers in a liquid crystal as observed by synchrotron X-ray scattering". *J. Phys* 47 (1986), p. 711.

[230] Chandrasekhar, S. *Liquid Crystals*. 2nd ed. Cambridge University Press, 1992.

[231] Xue, J., Jung, C. S., and Kim, M. W. "Phase transitions of liquid-crystal films on an air-water interface". *Phys. Rev. Lett.* 69, 3 (1992), pp. 474–477.

[232] Mul, M. N. de and Mann, J. A. "Multilayer formation in thin films of thermotropic liquid crystals at the air-water interface". *Langmuir* 10, 7 (1994), pp. 2311–2316.

[233] Takahashi, S. et al. "Quenching Spin Decoherence in Diamond through Spin Bath Polarization". *Phys. Rev. Lett.* 101, 4 (2008), p. 047601.

[234] Pham, L. M. et al. "NMR technique for determining the depth of shallow nitrogen-vacancy centers in diamond". *Phys. Rev. B* 93, 4 (2016), p. 045425.

[235] Schulz, B. et al. "Influence of mesoscopic structures on single molecule dynamics in thin smectic liquid crystal films". *Soft Matter* 7, 16 (2011), pp. 7431–7440.

[236] Guyot-Sionnest, P., Hsiung, H., and Shen, Y. R. "Surface polar ordering in a liquid crystal observed by optical second-harmonic generation". *Phys. Rev. Lett.* 57, 23 (1986), pp. 2963–2966.

[237] Bardon, S. et al. "Organization of cyanobiphenyl liquid crystal molecules in prewetting films spreading on silicon wafers". *Phys. Rev. E* 59, 6 (1999), pp. 6808–6818.

[238] Xu, L., Salmeron, M., and Bardon, S. "Wetting and molecular orientation of 8CB on silicon substrates". *Phys. Rev. Lett.* 84, 7 (2000), pp. 1519–1522.

[239] Kong, X. et al. "Towards Chemical Structure Resolution with Nanoscale Nuclear Magnetic Resonance Spectroscopy". *Phys. Rev. Applied* 4, 2 (2015), p. 024004.

[240] DeVience, S. J. "Nuclear Magnetic Resonance with Spin Singlet States and Nitrogen Vacancy Centers in Diamond". PhD thesis. Harvard University, 2014.

[241] Dvinskikh, S. V. et al. "Anisotropic self-diffusion in thermotropic liquid crystals studied by 1 H and 2 H pulse-field-gradient spin-echo NMR". *Physical review E* 65, 6 (2002), p. 061701.

[242] Thompson, P. A. and Robbins, M. O. "Shear flow near solids: Epitaxial order and flow boundary conditions". *Phys. Rev. A* 41, 12 (1990), pp. 6830–6837.

[243] Kočevar, K., Blinc, R., and Muševič, I. "Atomic force microscope evidence for the existence of smecticlike surface layers in the isotropic phase of a nematic liquid crystal". *Phys. Rev. E* 62 (2000), pp. 3055–3058.

[244] Miyano, K. "Surface-induced ordering of a liquid crystal in the isotropic phase". *J. Chem. Phys* 71, 10 (1979), pp. 4108–4111.

[245] Chao, C.-Y. et al. "Nature of Layer-by-Layer Freezing in Free-Standing 4O.8 Films". *Phys. Rev. Lett.* 77, 13 (1996), pp. 2750–2753.

[246] Vilfan, M. et al. "Liquid crystal 8CB in random porous glass: NMR relaxometry study of molecular diffusion and director fluctuations". *Phys. Rev. E* 76, 5 (2007), pp. 1–15.

[247] Zamar, R., González, C., and Mensio, O. "Molecular motions in thermotropic liquid crystals studied by NMR spin-lattice relaxation". *Braz. J. Phys* 28 (1998), p. 314.

[248] Kimmich, R. and Anoardo, E. "Field-cycling NMR relaxometry". *Prog. Nucl. Magn. Reson. Spectrosc.* 44, 3-4 (2004), pp. 257–320.

[249] Acosta, R. H. and Pusiol, D. J. "Pseudonematic order fluctuations of the director in the smectic phase of thermotropic liquid crystals". *Phys. Rev. E* 60, 2 (1999), pp. 1808–1811.

[250] Jordens, S. et al. "Non-equilibrium nature of two-dimensional isotropic and nematic coexistence in amyloid fibrils at liquid interfaces". *Nat. Commun.* 4, May (2013), pp. 1917–1918.

[251] Vink, R. L. "Crossover from a Kosterlitz-Thouless phase transition to a discontinuous phase transition in two-dimensional liquid crystals". *Physical Review E* 90, 6 (2014), p. 062132.

[252] Kaganer, V. M., Möhwald, H., and Dutta, P. "Structure and phase transitions in Langmuir monolayers". *Rev. Mod. Phys.* 71, 3 (1999), pp. 779–819.

[253] Ulman, A. *An Introduction to Ultrathin Organic Films From Langmuir-Blodgett to Self-Assembly*. Academic Press, 1991.

[254] Sengupta, A., Herminghaus, S., and Bahr, C. "Liquid crystal microfluidics: surface, elastic and viscous interactions at microscales". *Liq. Cryst. Rev.* 2, 2 (2014), pp. 73–110.

[255] Steinert, S. et al. "Magnetic spin imaging under ambient conditions with subcellular resolution". *Nat. Commun.* 4 (2013), p. 1607.

Acknowledgments

Curriculum Vitae

Contact information

MPRG-Nanoscale Spin Imaging,
Max Planck Institute for Biophysical Chemistry,
Am Fassberg 11, 37077, Göttingen.
Email: vkavata@mpibpc.mpg.de

Education

PhD: Oct/2012 - present
Max Planck Institute for Biophysical Chemistry, Göttingen,
Thesis title: Quantum Sensing with NV Centers in Diamond

Research assistant: Aug/2008-Sep/2012
Center For Nano and Soft Matter Sciences, Bangalore, India,

M.Sc. (Physics): Aug/2006-July/2008
Mangalore University, India,
Project: Synthesis and Characterization of CdSe quantum dots

B.Sc.: July/2003-June/2006
Kuvempu University, India,

Nationality: Indian

List of publications

[1] V. K. Kavatamane, D. Duan, S. R. Arumugam, N. Raatz, S. Pezzagna, J. Meijer and G. Balasubramanian, Probing phase transitions in a soft matter system using a single spin quantum sensor. *New J. Phys.* (DOI:10.1088/1367-2630/ab482d)

[2] V. K. Kavatamane, D. Duan, S. R. Arumugam, M. H. Phan and G. Balasubramanian, A Nitrogen-Vacancy spin based magnetometer with nano-Tesla static magnetic field sensitivity (manuscript in preparation)

[3] V. K. Kavatamane, D. Duan, S. R. Arumugam and G. Balasubramanian, Nanoscale NMR with defect centers in diamond, *Nanoscale(RSC journal)*, Invited review article (manuscript in preparation)

[4] D. Duan, V. K. Kavatamane, S. R. Arumugam, G. Rahane, G.-X. Du, Y.-K. Tzeng, H.-C. Chang and G. Balasubramanian, Laser-induced heating in a high-density ensemble of nitrogen-vacancy centers in diamond and its effects on quantum sensing, *Opt. Lett.*, 44,2851(2019)

[5] D. Duan, G. X. Du, V. K. Kavatamane, S. Arumugam, Y.-K. Tzeng, H.-C. Chang and G. Balasubramanian, Efficient nitrogen-vacancy centers' fluorescence excitation and collection from micrometer-sized diamond by a tapered optical fiber in endoscope-type configuration, *Opt. Express*,27,6734(2019)

[6] D. Duan, V. K. Kavatamane, S. R. Arumugam, G. Rahane, Y.-K. Tzeng, H.-C. Chang, H. Sumiya, S. Onoda, J. Isoya and G. Balasubramanian, Enhancing fluorescence excitation and collection from the nitrogen-vacancy center in diamond through a micro-concave mirror, *Appl. Phys. Lett.*, 113,041107(2018)

[7] A. Lazariev, S. Arroyo-Camejo, G. Rahane, V. K. Kavatamane and G. Balasubramanian, Dynamical sensitivity control of a single-spin quantum sensor, *Sci. Rep.*, 7,6586(2017)